creative commons
COMMONS DEED

저작자표시-비영리-변경금지 2.0 대한민국

이용자는 아래의 조건을 따르는 경우에 한하여 자유롭게

- 이 저작물을 복제, 배포, 전송, 전시, 공연 및 방송할 수 있습니다.

다음과 같은 조건을 따라야 합니다:

저작자표시. 귀하는 원저작자를 표시하여야 합니다.

비영리. 귀하는 이 저작물을 영리 목적으로 이용할 수 없습니다.

변경금지. 귀하는 이 저작물을 개작, 변형 또는 가공할 수 없습니다.

- 귀하는, 이 저작물의 재이용이나 배포의 경우, 이 저작물에 적용된 이용허락조건을 명확하게 나타내어야 합니다.
- 저작권자로부터 별도의 허가를 받으면 이러한 조건들은 적용되지 않습니다.

저작권법에 따른 이용자의 권리는 위의 내용에 의하여 영향을 받지 않습니다.

이것은 이용허락규약(Legal Code)을 이해하기 쉽게 요약한 것입니다.

Disclaimer

dCollection

공학박사 학위논문

Nitrogen-doped carbon produced by chlorination process of Ti(C,N) and its electrochemical properties

2019 년 2 월

서울대학교 대학원

재료공학부

이 문 균 (李 文 均)

Nitrogen-doped carbon produced by chlorination process of Ti(C,N) and its electrochemical properties

A Ph.D. thesis submitted

in fulfilment of the requirements for the degree of

Doctor of Philosophy

Approved by Major Advisor

Department of Materials Science and Engineering

Seoul National University

2019

MUN KEUN LEE

Nitrogen-doped Carbon produced by chlorination process of Ti(C,N) and its electrochemical properties

지도교수 정 인 호

이 논문을 공학박사 학위논문으로 제출함

2019 년 2 월

서울대학교 대학원

재 료 공 학 부

이 문 균

이문균의 박사 학위논문을 인준함

2019 년 02 월

위 원 장 박 종 래 (인)

부 위 원 장 정 인 호 (인)

위 원 남 기 태 (인)

위 원 김 용 선 (인)

위 원 연 순 화 (인)

Abstract

MUN KEUN LEE

Dept. of Materials Science & Engineering

The Graduate school

Seoul National University

Since the first demonstration of carbide-derived carbon (CDC), extensive research over varieties of metal carbides has been conducted and examined for use in numerous applications including supercapacitor, catalysis/catalyst support, gas storage/separation etc. Despite outstanding performances from CDC, due to limited variable compositions in metal carbide have drawn back its further uses as advanced material.

Previously, we have demonstrated one-step chlorination process to functionalize CDC materials by heteroatoms-doping (nitrogen and boron) having microporous to hollow structured carbon materials. The functionalized CDC material exhibited an enhancement in several applications, including CO_2 storage and oxygen reduction reaction (ORR). However, the mechanism involving nitrogen doping and the formation of hollow carbon still remained unclear at the time.

In this thesis in part 1, we have revisited the nitrogen-doped carbon (CN) materials produced from the chlorination process using titanium carbonitride to explore and propose a possible mechanism involving nitrogen doping and the formation of hollow carbon material in terms of experimental and theoretical.

In part 2, we explore how to improve the existing N-doped carbon for energy storage material. Based on thermodynamic and crystallographic aspect, we

propose a novel process to synthesize N-doped carbon. The process involves vacuum-annealing of starting material (titanium carbonitride) prior to chlorination reaction and this has confirmed a noticeable improvement in volumetric capacitance that is comparable to graphene materials.

Lastly, part 3 discusses how to prepare atomically dispersed Fe-CNB material and its electrocatalysts applications such as the oxygen reduction reaction. Based on the previous results and understandings, a novel in-situ method for effective doping of transitional metal atoms on the surface of nitrogen-doped carbon materials is proposed. In this work, the introduction of boron significantly increased the availability of pyridinic-N functional groups in CN materials, which allows Fe atoms to effectively bond to the surrounding four nitrogen atoms by forming Fe-N_4 structure. The introduction of boron increases the stability of pyridinic-N in Fe-CN, and maximizes Fe-N_4 formation, which is thermodynamically the most stable coordinated structured form. Consequently, atomically dispersed Fe-CNB demonstrated high electrochemical ORR catalytic properties. Moreover, the large-scale fabrication is also possible by this in-situ route, without any toxic acid leaching or post-treatment process involved.

Keywords: carbide derived carbon, nitrogen-doped carbon, Fe-N/C, atomic dispersion, supercapacitor, and oxygen reduction reaction.

Student number: 2013-30939

Contents

Abstract ..... **i**

List of Tables ..... **vi**

List of Figures ..... **vii**

List of Supporting Information ..... **xii**

1. Introduction ..... **- 1 -**

1.1. Carbon ..... - 1 -

1.2. Heteroatoms-doped porous carbon materials ..... - 4 -

1.3. Single-atom catalysts ..... - 7 -

2. Experimental Procedure ..... **- 11 -**

2.1. Preparation of nitrogen-doped carbons (CN) ..... - 11 -

2.2. Preparation of modified core-shell structured N-doped porous carbons - 14 -

2.3. Preparation of boron and nitrogen co-doped porous carbons (CNB)... - 15 -

2.4. Preparation of atomically dispersed iron, boron and nitrogen co-doped porous carbons (Fe-CNB) ..... - 15 -

2.5. Preparation of iron and nitrogen co-doped porous carbons (Fe-CN)... - 15 -

2.6. Thermodynamic Calculation ..... - 16 -

2.7. Characterization ..... - 16 -

2.7.1. Physical Characterizations ..... - 16 -

2.7.2. X-ray absorption spectroscopy (XAS) measurements ..... - 18 -

2.7.3. Capacitance measurements ..... - 18 -

2.7.4. Oxygen Reduction Reaction measurements ..... - 20 -

3. Results and Discussion ..... - 21 -

3.1. Nitrogen-doped carbon produced by chlorination process of Ti(C,N). - 21 -

3.1.1. Motivation ..... - 21 -

3.1.2. Raw powder analysis ..... - 22 -

3.1.3. Structure analysis ..... - 22 -

3.1.4. Textural and surface chemistry analysis ..... - 24 -

3.1.5. Morphology of carbonitride-derived carbons ..... - 33 -

3.1.6. Chlorination mechanism of titanium carbonitride: Formation of nitrogen-doped hollow carbon structure ..... - 38 -

3.1.7. Application of N-doped porous carbon materials ..... - 45 -

3.1.8. Conclusions ..... - 48 -

3.2. Core-shell structured carbonitride-derived carbon via pre-vacuum annealing with enhanced double-layer capacitance ..... - 49 -

3.2.1. Motivation ..... - 49 -

3.2.2. Vacuum-annealing of $Ti(C_{0.3},N_{0.7})$ ..... - 51 -

3.2.3. Core-shell structured N-doped carbon ..... - 54 -

3.2.4. EDLC application ..... - 68 -

3.2.5. Conclusions ..... - 78 -

3.3. Atomically dispersed Fe-doped CNB ..... - 80 -

3.3.1. Motivation ..... - 80 -

3.3.2. Results and Discussion ..... - 82 -

3.3.3. Conclusions ..... - 97 -

3.4. Appendix ..... - 98 -

3.4.1. Highly developed (002) planes from CN(73) ..... - 98 -

4. Overall Conclusion ..... - 100 -

References ..... - 103 -

Publication lists ..... - 109 -

Abstract (Korean) ..... - 110 -

List of Tables

TABLE 1. SUMMARY OF CORRESPONDING PORE PROPERTIES (BET SURFACE AREA AND PORE VOLUMES) AND NITROGEN ANALYSIS BY XPS OF TI(C_{1-x},N_x) SOLID SOLUTION CHLORINATED AT DIFFERENT TEMPERATURE. ..... - 32 -

TABLE 2. SUMMARY OF BET N_2 ADSORPTION DATA AND NITROGEN CONTENTS ANALYSED BY EA AND XPS. ..... - 61 -

TABLE 3. SUMMARIZED TEXTURAL PROPERTIES AND COMPOSITION CONCENTRATIONS ..... - 94 -

List of Figures

FIGURE 1. CLASSIFICATION OF CARBON MATERIALS AND THEIR POTENTIAL APPLICATIONS (IMAGES REPRINTED FROM [16, 34-40] ..... - 6 -

FIGURE 2. METHOD FOR PRODUCTION OF SILICON TETRACHLORIDE (REPRINTED FROM [17]) ..... - 6 -

FIGURE 3. PRICE OF THE ELEMENTS (IN $/KG) VERSUS THEIR ANNUAL PRODUCTION (IN KG/YR). (REPRINTED FROM [53]). ..... - 10 -

FIGURE 4. THE PRICE FOR 1 G OF PT/C (20 WT.%) IN KRW. (SIGMA-ALDRICH ACCESSED ON 17TH OF NOV. 2018). ..... - 10 -

FIGURE 5. SCHEMATIC DIAGRAM REPRESENTING AN EXAMPLE OF CHLORINATION PROCESS IN TITANIUM CARBONITRIDE SOLID SOLUTIONS. ..... - 13 -

FIGURE 6. SCHEMATIC DIAGRAM REPRESENTING CHLORINATION REACTOR SETUP: (1) GAS CABINET, (2) FLOWMETER, (3) HORIZONTAL QUARTZ-TUBE, (4) TUBE FURNACE, (5) CRUCIBLE CONTAINING STARTING MATERIALS, (6) H_2SO_4 SOLUTION, (7) KOH SOLUTION, AND (8) GAS DETECTOR. ..... - 13 -

FIGURE 7. XRD PATTERNS OF AS-RECEIVED TIC AND TI(C_{1-X},N_X) SOLID SOLUTION ((A) TIC, (B) TI($C_{0.7}$,$N_{0.3}$), (C) TI($C_{0.5}$,$N_{0.5}$), AND (D) TI($C_{0.3}$,$N_{0.7}$)). ..... - 27 -

FIGURE 8. XRD PATTERNS OF (A) TIC-CDC, (B) CN(73), (C) CN(55), AND (D) CN(37) CHLORINATED BETWEEN 600 TO 1200 ℃ FOR 3 HOURS (WHERE, ●: WC AND ▲: CO). ..... - 27 -

FIGURE 9. RAMAN SPECTRA OF (A) TIC-CDC, (B) CN(73), (C) CN(55), AND (D) CN(37), SYNTHESIZED DIFFERENT CHLORINATION TEMPERATURES. ..... - 28 -

FIGURE 10. N_2 ADSORPTION-DESORPTION ISOTHERMS FOR (A) TIC-CDC, (B)

CN(73), (C) CN(55), AND (D) CN(37) SYNTHESIZED AT 600 TO 1200 ℃. SOLID CIRCLES CORRESPOND TO ADSORPTION WHEREAS EMPTY CIRCLES TO DESORPTION OF NITROGEN. ..... - 29 -

FIGURE 11. PORE SIZE DISTRIBUTION OF TIC-CDC AND CN CHLORINATED AT 800 ℃ ESTIMATED USING NLDFT. ..... - 29 -

FIGURE 12. ESTIMATED PORE SIZE DISTRIBUTION USING N_2 ADSORPTION BY MP (LEFT COLUMN) AND BJH (RIGHT COLUMN) METHODS FOR (A) TIC-CDC, (B) CN(73), (C) CN(55), AND (D) CN(37)..... - 30 -

FIGURE 13. XPS ANALYSIS OF N 1S SPECTRA OF CNS SYNTHESIZED AT 600 TO 1000 ℃. EACH SPECTRUM IS DECONVOLUTED INTO FOUR PEAKS: N-1: $N_{PYRIDINIC}$, N-2: $N_{PYRROLIC}$, N-3: $N_{QUATERNARY}$, AND N-4: $N_{OXIDIZED}$, RESPECTIVELY. ..... - 31 -

FIGURE 14. TEM IMAGES OF TIC-CDC AND CN SYNTHESIZED AT 600 TO 1200 ℃ (ALL IMAGES ARE TAKEN IN SAME MAGNIFICATIONS). ..... - 35 -

FIGURE 15. HRTEM IMAGE OF TIC-CDC AND CN SYNTHESIZED AT 600 TO 1200 ℃. ..... - 36 -

FIGURE 16. TEM IMAGE OF CN(37)600 (A – C) AND CN(37)800 (D – F) CHLORINATED FOR 10, 30, AND 90 MINUTES. ..... - 37 -

FIGURE 17. THERMODYNAMIC CALCULATION RESULTS OF THE CHLORINATION OF TI($C_{0.7}$,$N_{0.3}$) (A – B) AND TI($C_{0.3}$,$N_{0.7}$) (C –D) AT 600 AND 800 ℃. ..... - 43 -

FIGURE 18. FORMATION MECHANISM OF (A) TIC-CDC, (B) CN(73), AND (C) CN(37)600 AND CN(37)800, WHERE YELLOW, GREEN, AND GREY BALLS REPRESENT TI, CL, N, AND C ATOMS, RESPECTIVELY. ..... - 44 -

FIGURE 19. CALCULATED (A) GRAVIMETRIC AND (B) VOLUMETRIC CAPACITANCE BASED ON CYCLIC VOLTAMMOGRAM AT VARIOUS SCAN RATES, AND, (C) NYQUIST PLOTS OF TIC-CDC800, CN(73)800, CN(55)800, AND CN(37)800. - 47 -

FIGURE 20. SEM IMAGES OF (A) AS-RECEIVED TIC, (B) AS-RECEIVED TI($C_{0.3}$,$N_{0.7}$), (C) TI($C_{0.3}$,$N_{0.7}$) VACUUM ANNEALED AT 600 ℃-4H, AND (D) TI($C_{0.3}$,$N_{0.7}$) VACUUM ANNEALED AT 1800 ℃-4H. ..... - 52 -

FIGURE 21. XRD PATTERNS OF (A) AS-RECEIVED TIC, (B) AS-RECEIVED TI($C_{0.3}$,$N_{0.7}$), AND TI($C_{0.3}$,$N_{0.7}$) VACUUM ANNEALED AT (C) 1600 ℃-4H AND (D) 1800 ℃-4H. - 52 -

FIGURE 22. EA DATA FOR AS-RECEIVED AND VACUUM-ANNEALED TI($C_{0.3}$,$N_{0.7}$) AT 1600 ℃-4H AND 1800 ℃-4H. ..... - 53 -

FIGURE 23. XRD PATTERNS OF (A) TIC-CDC AND CN(37), AND (B) VAC1600@CN(37) AND VAC1800@CN(37) OBTAINED FROM CHLORINATION AT 800 AND 1000 ℃ ..... - 58 -

FIGURE 24. RAMAN SPECTRA OF CHLORINATED SAMPLES FOR (A) AS-RECEIVED AND (B) VACUUM ANNEALED. (C) ILLUSTRATE THE I_D/I_G RATIO (BLACK LINE), FWHM OF D-BAND (RED LINE) G-BAND (BLUE LINE) OBTAINED FROM RAMAN SPECTRA FOR CN(37)S, VAC1600@CN(37)S, AND VAC1800@CN(37)S SYNTHESIZED AT 800 AND 1000 ℃, RESPECTIVELY. ..... - 59 -

FIGURE 25. NITROGEN ADSORPTION-DESORPTION ISOTHERMS OF (A) TIC-CDC AND CN(37), AND, (B) VAC1600@CN(37) AND VAC1800@CN(37), AND THEIR PORE SIZE DISTRIBUTION DETERMINED BY MP AND BJH PLOTS. ..... - 60 -

FIGURE 26. TEM IMAGES OF (A) TIC-CDC800, (B) TIC-CDC1000, (C) CN(37)800, (D) CN(37)1000, (E) VAC1600@CN(37)800, (F) VAC1600@CN(37)1000, (G) VAC1800@CN(37)800 AND (H) VAC1800@CN(37)1000 ..... - 62 -

FIGURE 27. SEM IMAGES OF (A) AS-RECEIVED TI($C_{0.3}$,$N_{0.7}$), (B) AND (C) TI($C_{0.3}$,$N_{0.7}$) VACUUM-ANNEALED AT 1600 AND 1800 ℃ FOR 4 HOURS, RESPECTIVELY. (D) TEM IMAGE OF 'STEPS' SITES IN VAC1800@CN(37)800. ..... - 63 -

FIGURE 28. SCHEMATICS OF PROPOSED FORMATION MECHANISMS OF TIC-CDC800, CN(37)800, AND VAC1800@CN(37)800. ..... - 64 -
FIGURE 29. HIGH RESOLUTION XPS N 1S CORE LEVEL SPECTRA FOR CN(37)S, VAC1600@CN(37), AND VAC1800@CN(37)S SYNTHESIZED AT 800 AND 1000 ℃. ..... - 67 -
FIGURE 30. CYCLIC VOLTAMMOGRAMS OF (A) TIC-CDC800, (B) TIC-CDC1000, (C) CN(37)800, (D) CN(37)1000, (E) VAC1600@CN(37)800, (F) VAC600@CN(37)1000, (G) VAC1800@CN(37)800, AND (H) VAC1800@CN(37)1000 AT SCAN RATE FROM 30 MV/S TO 200 MV/S. ..... - 74 -
FIGURE 31. GALVANOSTATIC CHARGE/DISCHARGE PROFILES OF (A) TIC-CDC800, (B) TIC-CDC1000, (C) CN(37)800, (D) CN(37)1000, (E) VAC1600@CN(37)800, (F) VAC1600@CN(37)1000, (G) VAC1800@CN(37)800 AND (H) VAC1800@CN(37)1000. EACH INSET DATA PROVIDES OBTAINED PROFILES AT 2, 5 AND 10 A/G. ..... - 74 -
FIGURE 32. CALCULATED (A) GRAVIMETRIC AND (B) VOLUMETRIC CAPACITANCE BASED ON CYCLIC VOLTAMMOGRAM AT VARIOUS CURRENT DENSITY. (C) NYQUIST PLOTS AND (D) THE IMPEDANCE PHASE ANGLE PLOT AS A FUNCTION OF FREQUENCY OF TIC-CDC800, CN(37)800, VAC1600@CN(37)800 AND VAC1800@CN(37)800 AT FREQUENCY RANGE BETWEEN 100 MHZ TO 10 KHZ. (E) LONG TERM CYCLIC STABILITY TEST RESULTS OF VAC1600@CN(37)800 AND VAC1800@CN937)800 AT 5 A/G OF CHARGE/DISCHARGE CURRENT DENSITY FOR 100,000 CYCLES. ..... - 75 -
FIGURE 33. CALCULATED (A) GRAVIMETRIC AND (B) VOLUMETRIC CAPACITANCES OF TIC-CDC1000, CN(37)1000, VAC1600@CN(37)1000 AND VAC1800@CN(37)1000 BASED ON CYCLIC VOLTAMMOGRAM AT VARIOUS

SCAN RATES. ..... - 76 -

FIGURE 34. CALCULATED (A – B) GRAVIMETRIC AND (C – D) VOLUMETRIC CAPACITANCES OF (A AND C) SAMPLES FROM 800 ℃ AND (B AND D) SAMPLES FROM 1000 ℃ BASED ON GALVANOSTATIC CHARGE/DISCHARGE AT VARIOUS CURRENT DENSITIES. ..... - 76 -

FIGURE 35. COMPARISON BETWEEN GRAVIMETRIC AND VOLUMETRIC CAPACITANCE FOR CARBON MATERIALS. (REPRODUCED FROM REFERENCE [20]) ..... - 77 -

FIGURE 36. (A) XRD PATTERNS OF FE-CNBS, (B) TEM IMAGE OF FE-CNB800. INSET: CORRESPONDING SAED PATTERN. (C) HIGH-RESOLUTION TEM IMAGE OF THE FE-CNB AT THE INTERIOR. INSET: CONTRAST PROFILE ON THE ARROW INDICATES INTERLAYER SPACING. (D) ENLARGED TEM IMAGE AT THE SURFACE OF THE FE-CNB PARTICLE. INSET: CORRESPONDING HR-TEM IMAGE. (E) HAADF-STEM IMAGE AND CORRESPONDING EDS SPECTROSCOPY ELEMENTAL MAPPING IMAGES OF C, N, O, AND FE. ..... - 89 -

FIGURE 37. (A) XRD PATTERNS OF FE-CNS, (B) TEM IMAGE OF FE-CN800. INSET: CORRESPONDING SAED PATTERN. (C) ENLARGED TEM IMAGE OF IRON OXIDE PARTICLE AND (D) HIGH-RESOLUTION TEM IMAGE OF THE IRON OXIDE. (E) HAADF-STEM IMAGE AND CORRESPONDING EDS SPECTROSCOPY ELEMENTAL MAPPING IMAGES OF C, N, O, AND FE. ..... - 90 -

FIGURE 38. (A) RAMAN SPECTRA OF FE-CN800 AND FE-CNB800 SAMPLES WITH 10 % OF FE. (B) I_D/I_G RATIO OF FE-CN800 AND FE-CNB800 WITH AMOUNT OF FE PRECURSOR VARYING FROM 1, 5, 10, AND 20 %. ..... - 91 -

FIGURE 39. BINDING ENERGY OF EACH ELEMENTS CALCULATED FROM COHP METHOD. THE RIGHT IMAGES SHOW THE CORRESPONDING ATOMIC POSITIONS FOR THIS CALCULATION. ..... - 91 -

FIGURE 40. HIGH-RESOLUTION XPS N 1S SPECTRA OF (A) CN800, (B) FE-CN800, (C) CNB800, (D) FE-CNB800; HIGH-RESOLUTION XPS B 1S SPECTRA OF (E) CNB800 AND (F) FE-CNB800. - 92 -

FIGURE 41. HIGH-RESOLUTION XPS FE 2P SPECTRA OF (A) FE-CN800 AND (B) FE-CNB800. - 93 -

FIGURE 42. N_2 ADSORPTION-DESORPTION ISOTHERM OF (A) CN, (B) CNB, (C) FE-CN AND (D) FE-CNB SYNTHESIZED AT 600, 800 AND 1000 ℃. - 93 -

FIGURE 43. FE K-EDGE (A) XANES AND (B) K^3-WEIGHTED FT-EXAFS SPECTRA OF FE-CN AND FE FOIL, AND, (C) FE-CNB AND FE FOIL WITH VARIABLE FE STARTING CONTENT. - 95 -

FIGURE 44. (A) LSV CURVE OF FE-CN800, (B) FE-CNB800 WITH DIFFERENT AMOUNT OF STARTING FE PRECURSORS AT 1600 RPM. (C) LSV CURVES OF CN, CNB, FE-CN, FE-CNB, AND PT/C AT 1600 RPM. - 96 -

FIGURE 45. THE ORIGINAL CONTRIBUTION TO KNOWLEDGE. - 102 -

List of Supporting Information

FIGURE S 1. SEM IMAGES OF AS-RECEIVED POWDER OF (A) TIC, (B), TI($C_{0.7}$,$N_{0.3}$), (C) TI($C_{0.5}$,$N_{0.5}$), AND (D) TI($C_{0.3}$,$N_{0.7}$). (E – F) SHOW THE SEM AND TEM IMAGES OF CN(73)800. - 99 -

1. Introduction

1.1. Carbon

Carbon is the most abundant and inexpensive, yet one of the most important material that exists in the form of zero- to three-dimensions with unique physical and chemical characteristics; high thermal and chemical stability, high surface area, wide pore size ranges and electrical conductivity. The significance of carbon materials has been already recognized by some of the greatest scientific awards including the 1996 Nobel prize in Chemistry (fullerenes), the 2008 Kavli Prize in Nanoscience (carbon nanotubes), and the 2010 Nobel Prize in Physics (graphene). In addition, carbon is the only element that has its own name as one of the most impacted peer-reviewed scientific journals published by Elsevier Science. The application of carbon-based materials varies widely. In particular, due to natural resource depletion, an intense research is focused in the renewable energy conversion technologies; electrodes in energy storage, [1] electrocatalysis/catalysis support materials, [2, 3] photocatalysis, [4] etc. Moreover, carbon-based materials are also researched for water purification, [5] gas separation/adsorption. [6]

The most commonly known and used carbon material is activated carbon (AC), fabricated by physical and chemical activations from carbonaceous materials such as coconut shell, coal, and wood, making them very cheap, thus, mass production is readily available. In addition, ACs exhibit large Brauner-Emmett-Teller specific surface area (BET SSA ≈ 800 to 3000 m^2/g). [7, 8] A typical application which requires such large surface area is electrode materials for

electrochemical double-layer capacitors (EDLCs). In EDLCs, the surface electrode charge generation involves surface dissociation and ion adsorption that store electric charge electrostatically through reversible process. [8] Thus, in theory, EDLC is an infinite lifetime energy application. In this regard, ACs with high BET SSA is expected to show large capacitance, but it has found that the specific capacitance does not linearly increase with SSA. This means that only part of pores are effective for charge accumulation. [9, 10]

According to the International Union of Pure and Applied Chemistry (IUPAC), classification of micropores are defined as pores of width less than 2 nm, mesopores range between 2 to 50 nm, and macropores are above 50 nm. [11] The precise control of pore size distributions (PSDs) is essential for specific applications as it influences the chemical and electronic performance of carbon materials. For example, in the case of energy storage applications, i.e. EDLCs, narrow micropore size control is preferred as it provide effective sites for charge storage. [12] However, carbon materials developed with only micropores are not easy for electrolyte to access the complete surface of carbon materials. [13] Consequently, the incapable of controlling pore size distribution of ACs limited from further increasing the capacitance. On the other hand, Yushin et al. [14] has reported that carbon materials having micropore as well as larger mesopore could improve the capacitance by providing larger channels that serve as ion-highway and allow for very fast ionic transport into the carbon materials. In addition, Ferrero et al. [15] reported that larger bimodal micro- and mesopore structured carbon-based materials also demonstrated a better electrocatalytic activity in oxygen reduction reaction than the micropore-only carbon-based materials, due to fast efficient transport toward/from the catalytic sites for both reactant and products.

Carbide-derived carbon (CDC) is a method to synthesize carbon materials having very narrow micro PSDs with large pore volume (up to 1.6 cm^3/g) and BET SSA ≈ 2000 m^2/g without post-activation and up to 3000 m^2/g with post-activation. [1] The process involves chlorination reaction at elevated temperature through conformal reaction, where metals in metal carbides are selectively extracted as metal chloride gases and carbon is left as a solid product. [16] The schematic in Figure 5 illustrates the extraction process of metal by chlorination. The chlorination reaction process based on metal carbide was, in fact, reported long before by Hutchins in 1918 (see Figure 2), [17] whom patented a method for the production of silicon tetrachloride using the following reaction :

$$SiC_{(s)} + 2Cl_{2\,(g)} = SiCl_{4\,(g)} + C_{(s)}$$

At time, the residual carbon was disposed or removed by introducing air to burn the carbon waste. However, ever since Gogotsi et al. [18] optimized and demonstrated the controllability of narrow PSDs using chlorination process, extensive researches over binary to ternary metal carbides, including TiC, SiC, B_4C, VC, NbC, WC, Ti_3SiC_2, Ti_2AlC, Ti_3AlC_2 have been conducted. [1] One of the fascinating results from CDC work was that an anomalous increase in capacitance was found with decrease in pore size. This result was completely different to the traditional view, as decreasing the pore size less than twice the solvated ion size reduces the normalized capacitance. This was due to the compacted ion layers from adjacent pore walls that impinges ions, reducing the available surface area for the double-layer formation. However, using TiC-CDC, Gogotsi et al. [12] has proven that this traditional view was completely reversed by showing an abrupt increase in specific capacitance with a pore size less than that of the solvated ion size.

On the other hand, despite its exclusive narrow PSDs and high BET SSA

characteristics, it was proposed that not all pores may not be electrochemically accessible, and more importantly, it could reduce the volumetric capacitance because of increased void space inside the pore structure that are not electrochemically active. [19, 20] It was also shown that the highly efficient ion transport can be achieved by either using very small nanoparticles [1] or developing additional larger pores in hierarchical structured way. [21] Therefore, in order to widen the use of CDC, control over broader range of PSDs is required, as each application require specific PSDs that matches its purpose.

1.2. Heteroatoms-doped porous carbon materials

Pure sp^2 carbon possesses π electrons that are highly stable which restrains its applicability in the field of electrochemistry. One of the strategies to improve the performance of electrochemical application is to introduce heteroatoms such as nitrogen, oxygen or boron in the carbon lattice. Among these dopants, nitrogen has received the most extensive attention in supercapacitor electrode material due to its effect on capacitance in both aqueous and organic electrolyte, with enhancement in wettability of electrodes. [22] By introducing electron-rich nitrogen atoms into the carbon lattice, the π electrons in carbon are conjugated to the lone-pair electrons of nitrogen atom and enhance the reactivity between active carbon materials and neighbouring molecules. In general, there exist four different types of nitrogen species in carbon-based nanomaterials, pyridinic-N, pyrrolic-N, quaternary-N (graphitic-N), and pyridinic-N-oxide (oxidized-N). [23-25] Recently, by combining classical molecular dynamic (CMD) and Kohn-Sham density functional theory (KS-DFT), Zhang et al. [26] has reported that the graphitic and pyridinic-N doped

carbon strongly affects the capacitance. In addition, nitrogen-doped carbon was also reported to show a significant improvement in electrocatalytic activity in oxygen reduction reaction (ORR) over Pt/C. [27] Among these four nitrogen functional groups, pyridinic-N was also readily reported to have responsible for donating one p-electron to the aromatic π-systems, thereby increasing the electron-donor ability of the carbon materials. [27, 28] It was also reported that increasing the percentage of graphitic-N by thermal annealing increases the overall ORR activity of N-doped carbon materials. [29]

On the other hand, by replacing carbon atoms with electron-deficient atoms such as boron was also reported to activate π electrons in ORR performance. [30] When the vacant $2p_z$ orbital of B conjugates with the carbon π system to extract the electrons, these electrons become active due to the low electronegativity of B, and thus oxygen molecules are reduced on the positively charged B sites. [31] Co-doping B and N is also possible route to improve the electrochemical performance in ORR activity, [32] as well as CO_2 gas adsorption. [33] Regarding doping strategy, most of nitrogen-doping processes employ ammonia gas reaction at high temperature, but this method generally yields low nitrogen content. [8] Therefore, by combining, preceding statement regarding control of PSDs, and, introducing heteroatoms in a simple and facile strategic way, will allow CDCs to extend its spectrum in advance materials technologies.

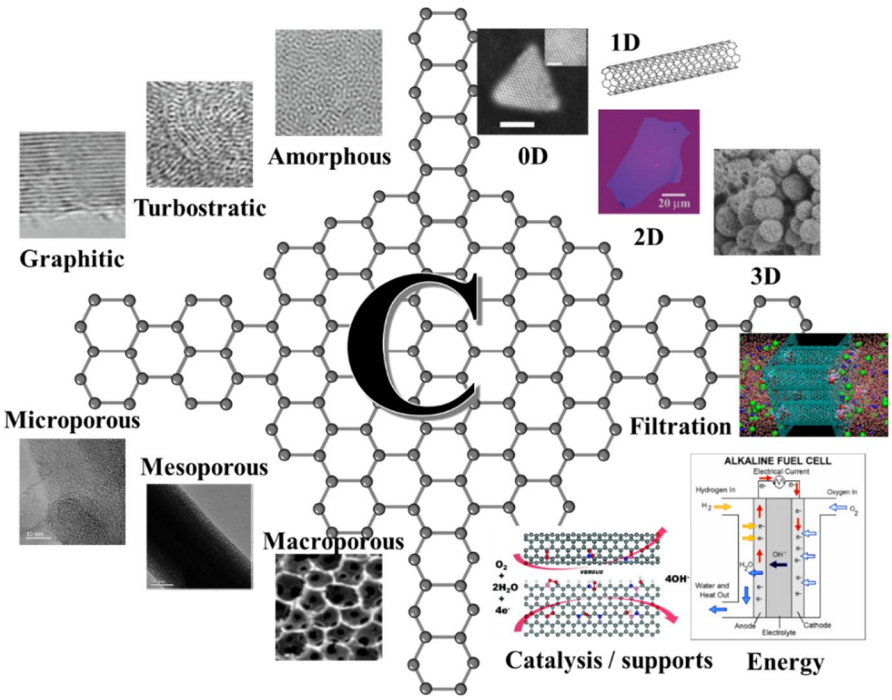

Figure 1. Classification of carbon materials and their potential applications (images reprinted from [16, 34-40]

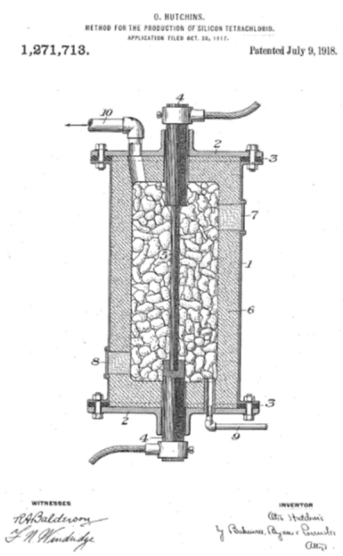

Figure 2. Method for production of silicon tetrachloride (reprinted from **[17]**)

1.3. Single-atom catalysts

Similar to batteries, proton membrane exchange fuel cells (PEMFC) convert chemical energy of fuel and oxidant into electric energy, with high efficiency and zero carbon emission. However, one of the major limitations in PEMFC is the sluggish kinetics of the oxygen reduction reaction (ORR) at the cathode due to high reduction overpotential. Traditionally, platinum has been considered as the best catalyst for the ORR but its uses are largely restricted by limited activity and stability, and most importantly, it was too expensive to be commercialized. The price of elements versus their annual production is shown in Figure 3 and the actual price of commercial Pt/C from Sigma-Aldrich is shown in Figure 4. In this regard, the development of non-Pt group metal (non-PGM) catalysts derived from earth-abundant elements for ORR is vastly demanding.

The development of nonprecious metal catalysts, and metal-free catalysts has been enormously researched over the past years because of their compatibility and at some extent, superior catalytic activity toward ORR performances. [15, 39, 41, 42] Among various non-PGM ORR catalysts developed in last decades, transition metal-nitrogen-carbon catalysts with especially M-N_x coordination active sites embedded in the basal planes of carbon matrixes were shown as the most promising ones due to their superb activity in both acidic and alkaline media and ease of scale-up production. [43] In addition, ever since Dai et al. [27] has demonstrated a superior ORR activity over Pt/C from metal-free nitrogen-doped vertically aligned carbon nanotube, metal-free catalysts has also gained increasing interest and researched as a potential candidate for ORR catalysts.

Heteroatoms-doped carbon often show efficient four electrons pathway

similar to the Pt/C, with high current densities and high onset potential. Although N-doped carbon materials demonstrate compatible or better performances in alkaline media, [44, 45] they usually suffer in strong acidic media after several cycles due to degradation of the carbon matrix. [46, 47] To overcome these drawback, N-doping has been combined with the addition of non-precious metals such as iron, cobalt, and nickel or metal oxides. These catalysts are generally prepared via high-temperature (> 800 ℃) pyrolysis between transition metal, nitrogen, and carbon precursors, during which the metal atoms are very easy to agglomerate into larger particles. Nevertheless, the ORR performance in acidic media is still insufficient and suffers from degradation due to the etching of metal species and/or decomposition of active sites. [48, 49] In ideal case, synthesis of single-atom catalysts (SACs) atomically dispersed M-N_x/C sites could further maximize the accessibility of active sites and improve the stability of metal atoms in acidic media. These SACs are also typically prepared by pyrolysis of transition metal, nitrogen and carbon precursors, followed by HF treatment to remove any bulk nanoparticles from agglomeration. Although SACs demonstrated a promising ORR performance, [50-52] it still remains a great challenge to fabricate SACs for mass production due to complex procedure and use of expensive precursors.

Hence, in this thesis, carbide-derived carbon (CDC) method was chosen as to their simplicity and already commercially available mass production method to produce active carbon material. Nitrogen-doped porous carbon, heteroatoms B, N co-doped porous carbon, and atomically dispersed Fe-N_x/C have been synthesized and evaluated as a potential supercapacitor electrode and/or ORR electrocatalysts. One of the most significant achievement in this study is the development of atomically dispersed Fe-CNB material with superior ORR catalytic performance

over commercially available Pt/C catalyst. The existence of boron played a critical role in atomic dispersion by enhancing the stability of Fe-N_4/C structure. By comparing Fe-CN and Fe-CNB, the synergetic effect of boron doping was explained based on the experimental observation and thermodynamic analysis.

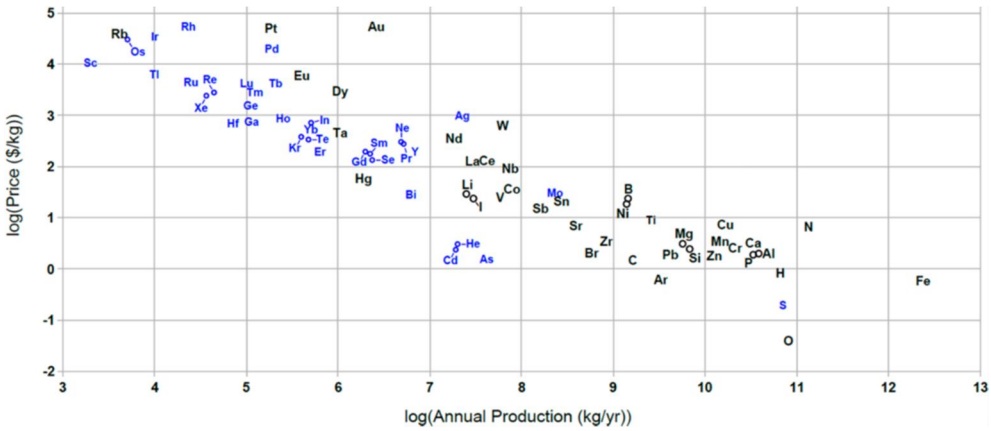

Figure 3. Price of the elements (in $/kg) versus their annual production (in kg/yr). (reprinted from [53])

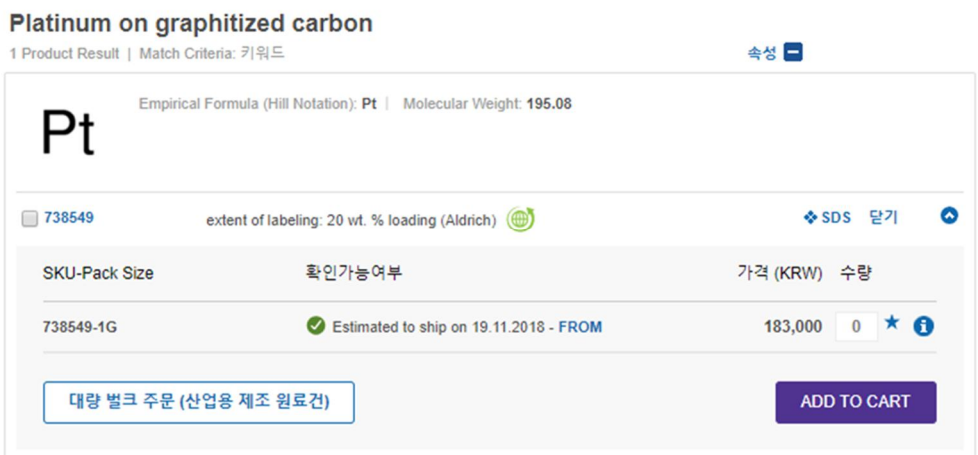

Figure 4. The price for 1 g of Pt/C (20 wt.%) in KRW. (Sigma-Aldrich accessed on 17th of Nov. 2018).

2. Experimental Procedure

The schematic diagram of the chlorination equipment is given in Figure 6, which is applied throughout all chlorination process in this work. All reagents and gases, unless otherwise stated, were obtained from commercial sources (Sigma Aldrich, Alfa Aesar, Shinjin Gas) and were used without further purification.

2.1. Preparation of nitrogen-doped carbons (CN)

Starting materials were commercially available micron-sized TiC (Alfa Aesar, 99.5 %; under 2 μm), $Ti(C_{0.7},N_{0.3})$, $Ti(C_{0.5},N_{0.5})$, and $Ti(C_{.3},N_{0.7})$ solid solutions (Treibacher Industrie AG, 99.5 %; 1 – 2 μm). No pre-treatment was applied. High purity Cl_2 (99.995 %), Ar (99.999 %), and H_2 (99.999 %) gases were introduced as reactive and purging gases to a reaction chamber equipped with carbon sheet boat installed in the horizontal quartz tube. The gas flowrate was controlled with flowmeter, and two grams of starting titanium carbonitride material was loaded in the carbon boat. The temperature of reaction chamber was controlled by SiC heating materials and K-type thermocouple was installed to measure the sample temperature. The quartz tube was purged with Ar gas (50 cc/min) over 30 minutes prior to each experiment and the furnace was heated to desired temperature (600 to 1200 ℃) at the rate of 10 ℃/min. During chlorination experiments, Cl_2 gas was injected for three hours at the flow rate of 20 cc/min. After chlorination reaction, Cl_2 gas was switched back to Ar gas (50 cc/min) and the furnace was cooled down to 600 ℃. At this temperature, H_2 gas (20 cc/min) was employed for

two hours in order to remove any residual Cl_2 trapped in the pores. For the samples chlorinated at 600 ℃, Ar was fed at the same temperature for thirty minutes then switched to H_2 gas.

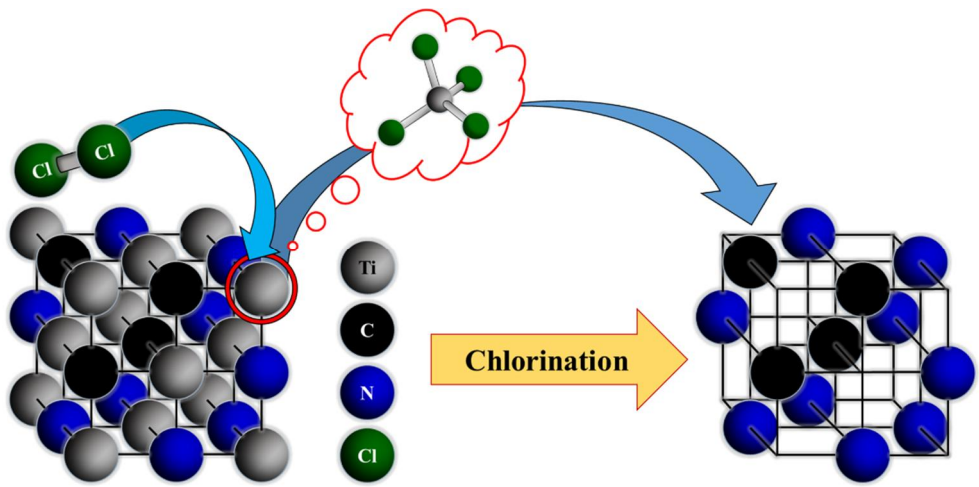

Figure 5. Schematic diagram representing an example of chlorination process in titanium carbonitride solid solutions.

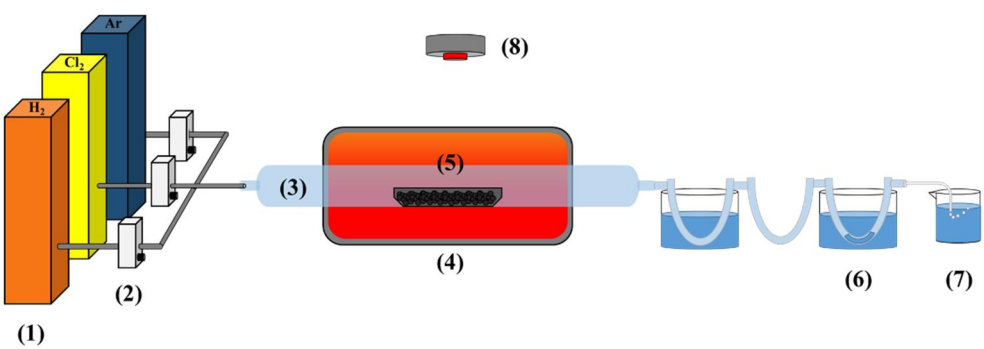

Figure 6. Schematic diagram representing chlorination reactor setup: (1) gas cabinet, (2) flowmeter, (3) horizontal quartz-tube, (4) tube furnace, (5) crucible containing starting materials, (6) H_2SO_4 solution, (7) KOH solution, and (8) gas detector.

2.2. Preparation of modified core-shell structured N-doped porous carbons

$Ti(C_{0.3},N_{0.7})$ starting materials were placed in graphite furnace for high temperature annealing at 1600 and 1800 ℃ for 4 hours under a vacuum (10^{-5}), and then cooled down to room temperature at rate of 10 ℃/min. As vacuum-annealed powders were sintered to form hard particles, they were crushed and ground until it became fine powder by using agate mortar.

For chlorination reaction, a carbon sheet boat containing two grams of vacuum-annealed powders was loaded into a horizontal quartz tube furnace at room temperature. The quartz tube was purged with Ar gas over thirty minutes prior to each experiment. The tube furnace with sample was heated to desired temperature (800 and 1000 ℃) at the heating rate of 10 ℃/min, after which the Ar gas was replaced by Cl_2 gas at the flow rate of 15 cc/min. After chlorination reaction for three hours, the gas was switched back to Ar gas and the furnace was cooled down to 600 ℃ at 10 ℃/min. At this temperature, H_2 gas was injected for two hours in order to remove any residual Cl_2 gas trapped in the pores of the samples.

As-received TiC and $Ti(C_{0.3},N_{0.7})$ starting materials were also chlorinated using the same procedure to clarify the effect of pre-vacuum annealing process of carbon materials to the final performance.

2.3. Preparation of boron and nitrogen co-doped porous carbons (CNB)

CNB were synthesized in the same manner as described in the previous section 2.1, but with the addition of a boron precursor. $Ti(C_{0.5},N_{0.5})$ and TiB_2 were mixed by hand in an agate mortar for fifteen minutes before the chlorination reaction. In this study, chlorination reaction was proceeded at 600, 800, and 1000 ℃ for five hours at heating rate of 10 ℃/min. The rest of schedules are same as in 2.1. The mixing molar ratio of carbon to boron in the precursors were 4:1, 1:1, and 1:4, respectively. For comparison, chlorination reaction was also conducted at 800 ℃ for three and ten hours.

2.4. Preparation of atomically dispersed iron, boron and nitrogen co-doped porous carbons (Fe-CNB)

Fe-CNB were synthesized in similar procedure to previous section 2.3, but with the addition of iron precursor. $Ti(C_{0.5},N_{0.5})$, TiB_2 and $Fe(acac)_3$ were mixed by hand in an agate mortar for fifteen minutes before the chlorination reaction. The chlorination reaction was proceeded at 600, 800, and 1000 ℃ for five hours at same heating rate to the previous section. The rest of schedules are same.

2.5. Preparation of iron and nitrogen co-doped porous carbons (Fe-CN)

For controlled experiment, Fe-CN were also synthesized in the same

procedure as described in section 2.4, but without boron precursor. $Ti(C_{0.5},N_{0.5})$ and $Fe(acac)_3$ were mixed by hand in an agate mortar for fifteen minutes before the chlorination reaction. The chlorination reaction was progressed for five hours at 600, 800, and 1000 ℃. The rest of schedules are same as in section 2.3.

2.6. Thermodynamic Calculation

The FactSage thermochemical software (version 7.2) [54] was employed to perform the thermodynamic equilibrium calculations. FACTPS databases and FSStel database were used for all stoichiometric solids and Ti(C,N) solid solutions, and gas species in the Ti-C-N-Cl system. The thermodynamic calculations were performed for a closed system at constant total pressure of 1 atm.

2.7. Characterization

The yield for carbon products after chlorination was calculated using the following equations:

$$\text{Yield } (\%) = \frac{Obtained\ mass}{Theoretical\ mass\ of\ C{+}N\ in\ Ti(C_{1-x},N_x)} \times 100 \qquad (1)$$

2.7.1. Physical Characterizations

Gas adsorption analysis was performed using BELSORP-mini (BEL JAPAN INC., Japan) with N_2 adsorbate at 77 K from 0.01 atm to 0.15 atm. Before each gas adsorption measurement, the sample was pre-heated at 300 ℃ for 24

hours under vacuum to remove any residual water and other physically adsorbed impurities. The specific surface area of each sample was determined using the Braunauer-Emmett-Teller (BET) method. The pore size distribution (PSDs) was analysed from the nitrogen adsorption data using micropore plot (MP), Barret-Joyner-Halenda (BJH) plot, and non-linear density functional theory (NL-DFT) method with a slit pore model.

X-ray diffraction (XRD) spectra were obtained using X-ray diffractometer (D-MAX2500-PC, Rigaku, Japan) with Cu-Kα radiation. Raman analysis was carried out using Raman spectroscopy (LabRam HV Evolution, HORIBA, Japan) using an Ar ion laser (514.5 nm) at 100x magnification (~2 μm spot size). The Fourier Transform Infrared spectroscopy (FT-IR) spectrophotometer (Nicolet 6700, Thermo Scientific, USA) were obtained under vacuum. X-ray photoelectron spectroscopy (XPS) analysis was carried out using an Electron Spectroscopy for Chemical Analysis (ESCA, Kratos Axis Supra, UK) with Mg in Mg/Al dual anode source. A binding energy of 284.5 eV was selected as a reference for C 1s. The contents of C, N, and O in the CDC products were determined by Elemental Analysis (EA) (Flash2000, Thermo Fisher Scientific, German) and metal contents were determined by Inductively Coupled Plasma-Atomic Emission Spectrometer (ICP-AES) (OPTIMA 4300DV, Perkin-Elmer, USA).

Morphological analyses were conducted by Field Emission Scanning Electron Microscope (FE-SEM) (MERLIN Compact, Zeiss, German) operating at 10 kV, and, High Resolution Transmission Electron Microscope (HR-TEM) (JEM-2100F, JEOL Ltd., Japan) operating at 200 kV. In particular, the samples for TEM analysis were supported on ultrathin carbon film-supported Cu grids.

2.7.2. X-ray absorption spectroscopy (XAS) measurements

X-ray absorption near edge structure (XANES) was used for the chemical state analysis and coordination symmetry, and extended X-ray absorption fine structure (EXAFS) was used to elucidate the local geometric factor around iron. XANES analysis was conducted after background subtraction and normalization. The EXAFS signals for the Fe K-edge of the samples were extracted and were Fourier-transformed (FT) over the k-space range of 2.5 – 10 $Å^{-1}$, using k^3 weight and a Hanning window. All experimental measurements are conducted from 10C Wide-Energy XAFS beamline of Pohang Light Source (PLS-II).

2.7.3. Capacitance measurements

Supercapacitor electrodes for the electrochemical measurements of the prepared samples were fabricated with active material, Super P and Polytetrafluoroethylene (PTFE) in gravimetric ratio of 8:1:1. These components were thoroughly mixed together with few drops of isopropyl alcohol (IPA) until homogeneous black paste was obtained. This paste was shaped into 1×1 cm square and attached on the SUS mesh. After drying under 0.1 Torr vacuum at room temperature for 12 hr, the electrodes were soaked in 6.0 M KOH solution for 1 day before tests. Prior to the electrochemical test, optical images and thicknesses of the prepared electrodes were obtained to calculate the volumes of the electrodes. All the electrochemical tests were proceeded with a standard three-electrode system: Prepared carbon electrode as a working, Pt mesh as a counter and standard Ag/AgCl electrode as a reference. A 6.0 M KOH in deionized water solution was

adopted as an electrolyte. A potentiostat electrochemical instrument (ZIVE SP2, WonATech) was utilized for cyclic voltammetry (CV), Galvanostatic charge/discharge and electrochemical impedance spectroscopy (EIS).

Cyclic voltammetry experiments were proceeded at a potential window from 0 to -0.8 V with various scan rates ranging from 1 mV s^{-1} to 200 mV s^{-1}. Galvanostatic charge/discharge profiles were obtained at a potential window from 0 to -0.8 V at various scan rates from 0.1 A g^{-1} to 10 A g^{-1}. Gravimetric and volumetric capacitance with CV graphs were calculated by following the equation:

$$C = \frac{\int i(E)dE}{2\nu\Delta E(m \text{ or } V)} \quad (2)$$

where ∫i(E)dE is integrated area of the CV graph, ν is scan rate (V/s), ΔE is potential window (V), m and V are the mass and volume of the active material, respectively.

Gravimetric and volumetric capacitance with Galvanostatic charge/discharge graphs were calculated by following the equation:

$$C = \frac{i\Delta t}{\Delta E(m \text{ or } V)} \quad (3)$$

where i is the applied constant discharging current, Δt is the discharging time, ΔE is the voltage range, m and V are the mass and volume of the active material, respectively.

Electrochemical impedance spectroscopy (EIS) was proceeded at a frequency range from 100 mHz to 100 kHz at a bias voltage of -0.4 V and an

amplitude of 10 mV.

2.7.4. Oxygen Reduction Reaction measurements

The electrochemical properties were studied with an Autolab potentiostat (PGSTAT302N, Metrohm) in a standard three-electrode cell with a graphite rod as a counter electrode and a saturated Ag/AgCl as a reference electrode. The catalyst ink was prepared by dispersing 10 mg catalyst in 500 μL Nafion solution (400 μL 2-propanol (Sigma-Aldrich), 50 μL water, and 50 μL Nafion solution (5 wt%, Simga-Aldrich)). The working electrode was prepared by dropping the catalyst ink (8.66 μL) onto the glassy carbon (0.248 cm^2) of the rotating ring-disk electrode (RRDE, Pine, E7R9 series tips) which was left for drying at room temperature. This resulted in a catalyst loading of 700 $\mu g/cm^2$. Before the electrochemical experiments, the Ag/AgCl reference electrode was calibrated against a Pt electrode in the H_2 purged electrolyte. Accordingly, all of the potentials shown are the RHE scale. The ORR performance was measured in an O_2-saturated 0.1 M KOH (Sigma-Aldrich, 99.99 wt%) solution at a rotating rate of 1600 rpm and a scan rate of 10 mV/s at 293 K in a water bath. The non-Faradaic capacitance term was calibrated by reduction of cyclic voltammetry under Ar at the same scan rate. The total electron transfer number was calculated from the disk/ring current of the RRDE system, setting the Pt ring potential at 1.2 V_{RHE}. Supercapacitor performance was conducted by using the same system. The specific capacitance of these carbonaceous materials were measured in a 1 M KOH solution purged with Ar gas.

3. Results and Discussion

3.1. Nitrogen-doped carbon produced by chlorination process of Ti(C,N)

3.1.1. Motivation

In our previous work, [32, 55] N-doped porous carbons and N,B co-doped hollow carbons were synthesized by chlorination reaction of $Ti(C_{1-x},N_x)$ solid solution (x = 0, 0.3, 0.5, 0.7) with TiB_2 as boron precursor.

Although the pore evolution is well described for nitrogen-doped porous carbons, the effect of nitrogen species on N-doped carbon by carbonitride-derived carbon and its formation mechanism still remained undiscussed. Moreover, Kim et al. [32] reported that chlorination of nitrogen-rich $Ti(C_{0.3},N_{0.7})$ experienced structural collapse due to the formation of CNCl and C_xN_y gases, but, the addition of the boron source can successfully stabilize C-N bonding on the surface layer and facilitates the formation of hollow carbon. However, during this study, we have found that the formation of hollow carbon is also possible without the use of boron source. Hence, it is necessary to re-investigate systematically to understand these nitrogen-doped carbon and hollow carbon, considering that there is an increased potential for nitrogen-doped (hollow) carbon materials in energy conversion and storage applications.

3.1.2. Raw powder analysis

According to the XRD analysis, neither any secondary nor impurity phases were found from starting materials, TiC and Ti(C_{1-x},N_x) solid solution powders where x = 0.3, 0.5, and 0.7 (see Figure 7). XRD peaks for Ti(C_{1-x},N_x) solid solutions were shifted to higher 2θ angles compared to TiC because the lattice parameter of TiN (4.24173 Å, JCPDS 38-1420) is known to be smaller than TiC (4.3274 Å, JCPDS 32-1383). Thus, the increase in nitrogen contents in Ti(C_{1-x},N_x) solid solution shifts the patterns to higher angles.

3.1.3. Structure analysis

Figure 8 illustrates the XRD patterns of TiC-CDCs and CNs obtained from chlorination of TiC and Ti(C_{1-x},N_x) solid solutions. All XRD patterns for TiC-CDCs and CNs shows a broad turbostratic XRD patterns without any secondary or unreacted TiC or Ti(C_{1-x},N_x) peaks except for those chlorinated at 600 ℃ showing impurity WC phases. Although longer chlorination (up to 5 hours, not shown) were performed, WC peaks can still be more or less visible. This is because, Ti(C_{1-x},N_x) is commonly produced by WC-Co ball milling between titanium oxide and carbon followed by carbothermal/carbonitriding reduction method. [56, 57] In addition, WC-CDCs are known to have slow mass transport and charge transfer limitation, requiring higher chlorination temperature for a complete carbide-to-carbon transformation. [58] Nevertheless, according to the XRD results, TiC and Ti(C_{1-x},N_x) was completely transformed to carbon materials after chlorination at 800 ℃ and above. At higher temperature, the completion was achieved even less than

three hours. The peak centred at ~26° is observed due to diffraction from (002) planes of graphite along the c-axis having a nanocrystalline structure. Another peak at ~44° is attributed to the (100)/(101) lateral planes of graphite. These two broad diffraction peaks are typical characteristics for porous carbon of turbostratic structure. [59] The development of a sharp and narrow XRD peaks for the samples at 1200 ℃ indicates the increase of crystallization of carbon after the chlorination at high temperature. Another exception was found from CN(73) in Figure 8(b) showing a sharp straight peak at ~26° along with broad XRD patterns throughout all chlorination reaction, suggesting more development of (002) planes of graphitic carbon along the c-axis. This will be discussed further in the Appendix section 3.4.

Raman spectroscopy is a standard non-destructive characterization method for crystalline, nanocrystalline, and amorphous carbons. [60] The Raman spectra of disordered carbon typically exhibit two broad peaks: The peak at 1580 cm^{-1} (G-band) corresponds to in-plane vibrations from E_{2g} modes of graphite and the peak at ~1330 cm^{-1} (D-band) is associated with the out-of-plane vibrations from A_{1g} modes of carbon atoms with turbostratic carbon. [61-63] As can be seen in Figure 9, all of the TiC-CDCs and CNs synthesised between 600 to 1200 ℃ shows both D- and G-peaks, typical of amorphous disordered carbon. In general, both D- and G-band become narrower with increase in chlorination temperature, which can be attributed to the carbon ordering. [64] The highest carbon ordering was achieved from chlorination at 1200 ℃, which is consistent with the XRD analysis in Figure 8. In the case of CN(37)600 in Figure 9(d), a slight different result to that other samples was obtained; narrow D- and G-peaks with a distinct shoulder at 1613 cm^{-1} attributing to D'-peak were observed for CN(37)600. The D' band corresponds to the highest wavenumber feature in the density of state, which is forbidden under

the defect-free conditions [65] but associated with the presence of defects in the lattice and it originates from the double resonance progress. [66, 67] The narrow FWHM and the existence of both D and D'-peaks suggesting that the obtained CN(37)600 is highly defected with non-porous, polycrystalline structure.

3.1.4. Textural and surface chemistry analysis

The N_2 adsorption isotherms of TiC-CDCs and CNs are shown in Figure 10 and obtained results including obtained yields, BET specific surface area and pore volumes are summarized in Table 1. Due to low yield obtained from CN(37)600 (about 3 %), we were not able to characterize the porosity properties. All isotherms of TiC-CDCs up to 1000 ℃ shows Type I in the Brunauer classification (Figure 10(a)), which rise from a rapid adsorption in the low-pressure regime, and then converges during the desorption process. This indicates that TiC-CDCs consist of micropore-rich structure of adsorbent. For TiC-CDC1200, Type IV hysteresis loop was observed with decreased in micropore volume, suggesting formation of cylindrical mesopores due to pore coalescence of micropores along with carbon ordering. [68-71] All TiC-CDCs agrees with the previously reported works. [72-74] On the other hand, all CNs exhibit hysteresis loop with Type IV, also suggesting the formation of mesopores in all cases. In case of CN(37)s, less-porous, yet increase in the adsorption at higher pressure, P/P_0 = 0.90 – 0.99, with H2-type hysteresis loop suggests that the size and shape of the pores are not unimodal, but the pore size spreads from the micro- to the macro-pore regions, showing the development of hierarchical pore structure. CNs generally demonstrated a decrease in adsorption at lower pressure with increasing nitrogen contents in $Ti(C_{1-x},N_x)$, suggesting a

decrease in micropore volume. The pore size distribution (PSD) determined by non-local density functional theory (NLDFT) for those chlorinated at 800 ℃ are illustrated in Figure 11, and the PSD for sample chlorinated at other temperatures are shown, which is determined by micropore plot (MP) and Barret-Joyner-Halenda (BJH) plots illustrated in Figure 12 are further supporting the development of hierarchical pore structure. A decrease in Brunauer-Emmett-Teller (BET) specific surface area is also observed as the nitrogen contents in $Ti(C_{1-x},N_x)$ increases. For example, CNs synthesized at 800 ℃ were found to have 1807 m^2/g for CN(73)800, 1097 m^2/g for CN(55)800, and 842 m^2/g for CN(37)800, respectively. Given that the nitrogen functional groups are highly unstable during high temperature chlorination reactions, $Ti(C_{1-x},N_x)$ with high nitrogen contents tend to partially decompose because of a deficiency in adjacent carbon from the raw powder (the ratio between C to N is 3:7 for CN(37)s), but also due to the formation of ClCN and C_xN_y gases as reported by our previous work. [55] Consequently, lowest yield and micropores volume were obtained with CN(37) (CN(37) yields ≈ 0.8 %, 9.0 %, 25.5 %, and 25.7 % for CN(37)600, 800, 1000 and 1200, respectively). The overall carbon yield, BET SSA and pore volume are summarized in Table 1.

X-ray photoelectron spectroscopy (XPS) analysis was carried out in order to analyse the surface chemistry of obtained carbon. Regardless of loss of nitrogen by decomposition of C_xN_y and ClCN gas phases, XPS results in Figure 13 show that all CNs are found to have nitrogen-containing functional groups, mainly pyridinic (398.7 eV) and graphitic (401.2 eV) nitrogen. [41] It is up to 12 at.% of nitrogen with CN(55)600 and it decreases with increasing chlorination temperature, due to the instability of nitrogen functional group, especially at edge sites, at high

temperatures. The introduction of heteroatoms such as nitrogen is now one of the most common strategy to improve the performance in electrochemical applications, in which graphitic and pyridinic-N usually affecting the electrochemical reactivity. [26, 27] Ammonia gas reaction is one of the most common strategy for nitrogen doping, but this method generally yields low nitrogen contents and it is rather unstable. [8] However, this study demonstrates that high amount of nitrogen (2.9 – 12.3 at.%, see Table 1) can be simultaneously doped by directly chlorinating titanium carbonitride at elevated temperature. The major difference to ammonia gas reaction is that, after extraction of Ti atoms by $TiCl_4$, highly active C and N atoms will be left with small atomic distances. Although N_2 is the most thermodynamically stable known phase, highly active C will rearrange and rebond to adjacent N atoms, resulting higher amount of carbon-nitrogen within carbon network. The amount of nitrogen in CNs are also summarized in Table 1.

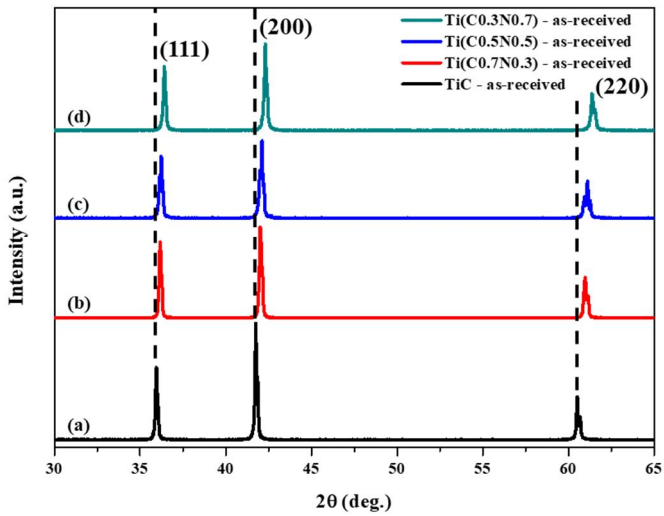

Figure 7. XRD patterns of as-received TiC and Ti(C_{1-x},N_x) solid solution ((a) TiC, (b) Ti($C_{0.7}$,$N_{0.3}$), (c) Ti($C_{0.5}$,$N_{0.5}$), and (d) Ti($C_{0.3}$,$N_{0.7}$)).

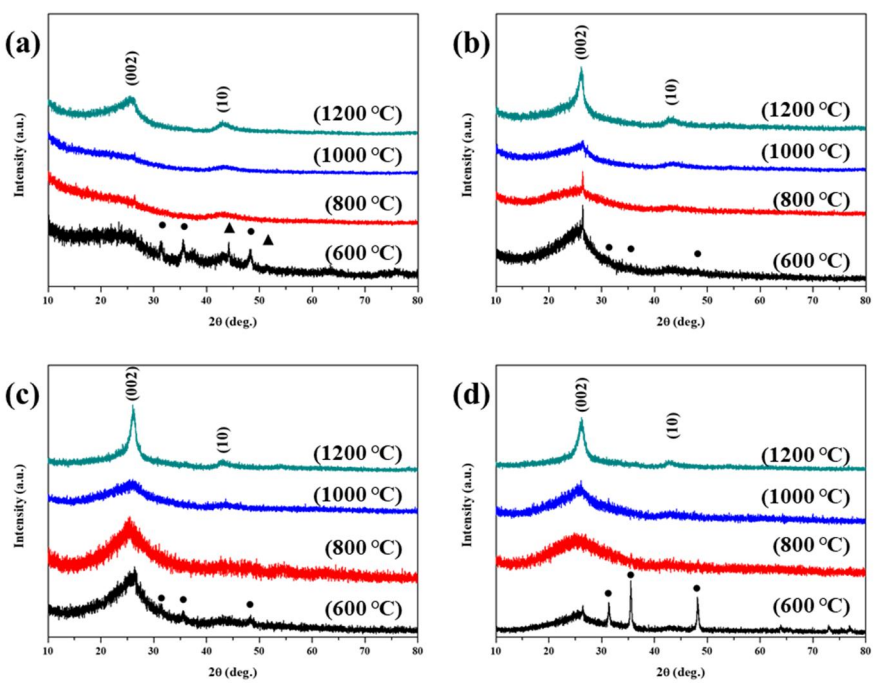

Figure 8. XRD patterns of (a) TiC-CDC, (b) CN(73), (c) CN(55), and (d) CN(37) chlorinated between 600 to 1200 ℃ for 3 hours (where, ●: WC and ▲: Co).

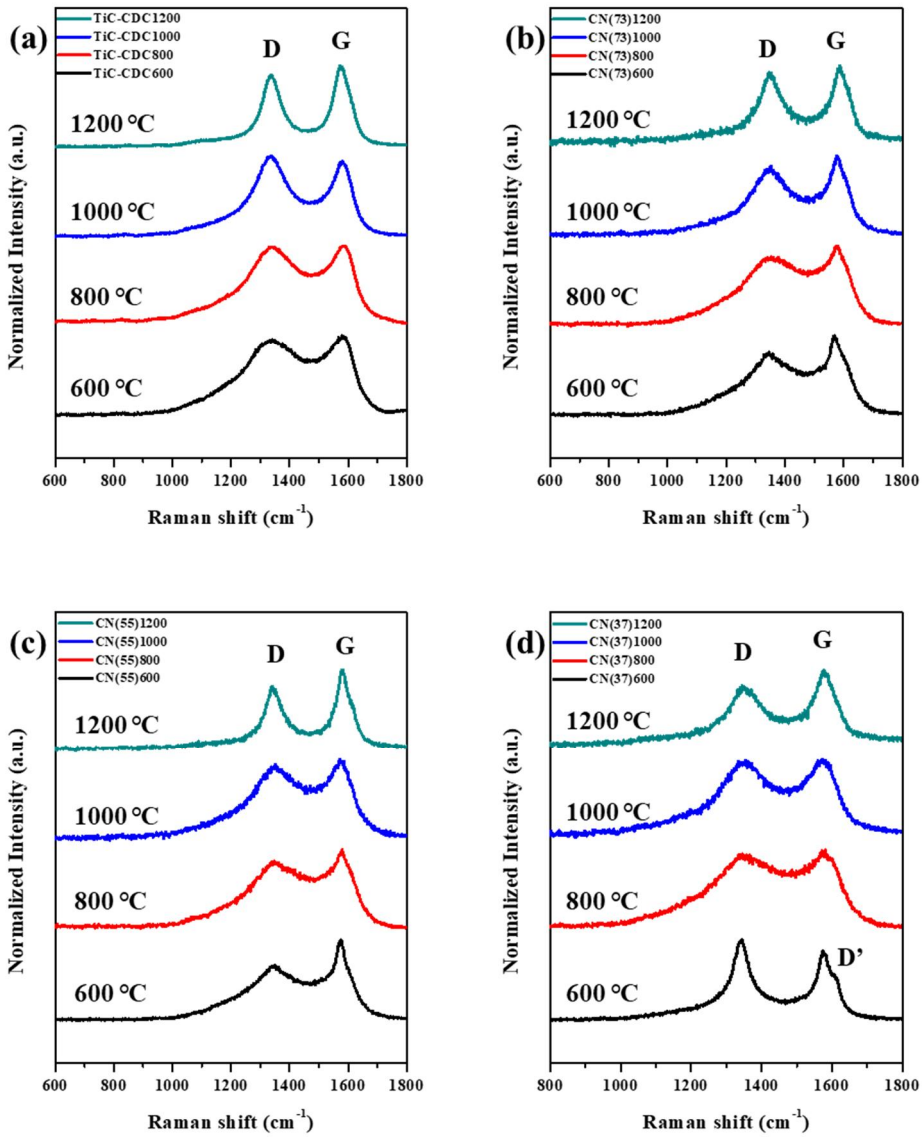

Figure 9. Raman spectra of (a) TiC-CDC, (b) CN(73), (c) CN(55), and (d) CN(37), synthesized different chlorination temperatures.

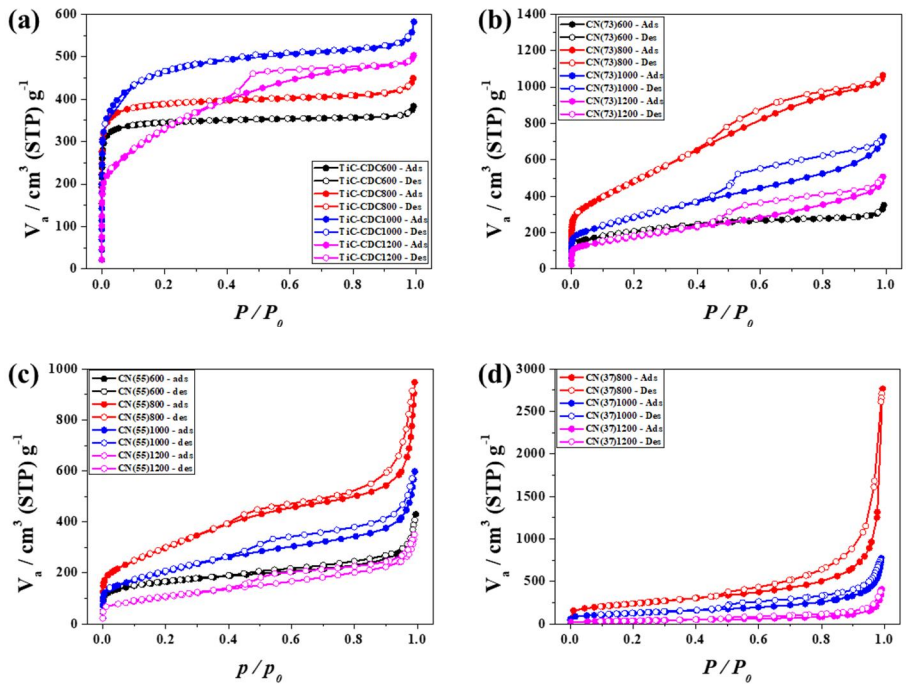

Figure 10. N_2 adsorption-desorption isotherms for (a) TiC-CDC, (b) CN(73), (c) CN(55), and (d) CN(37) synthesized at 600 to 1200 ℃. Solid circles correspond to adsorption whereas empty circles to desorption of nitrogen.

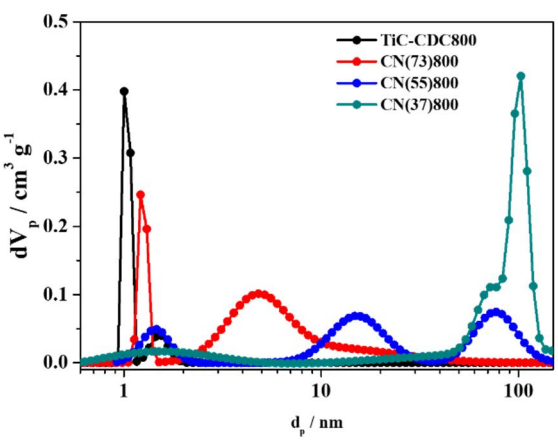

Figure 11. Pore size distribution of TiC-CDC and CN chlorinated at 800 ℃ estimated using NLDFT.

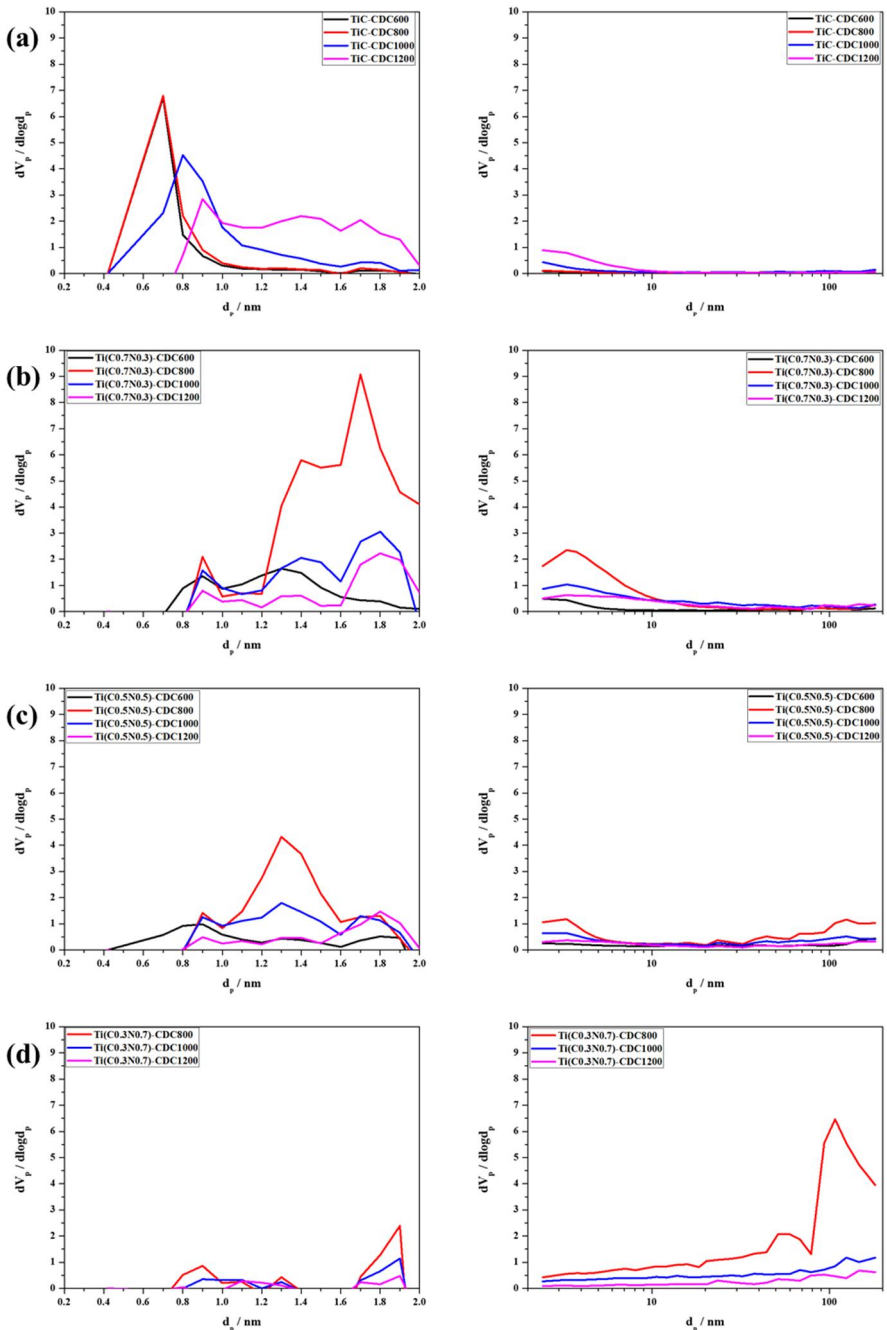

Figure 12. Estimated pore size distribution using N_2 adsorption by MP (left column) and BJH (right column) methods for (a) TiC-CDC, (b) CN(73), (c) CN(55), and (d) CN(37).

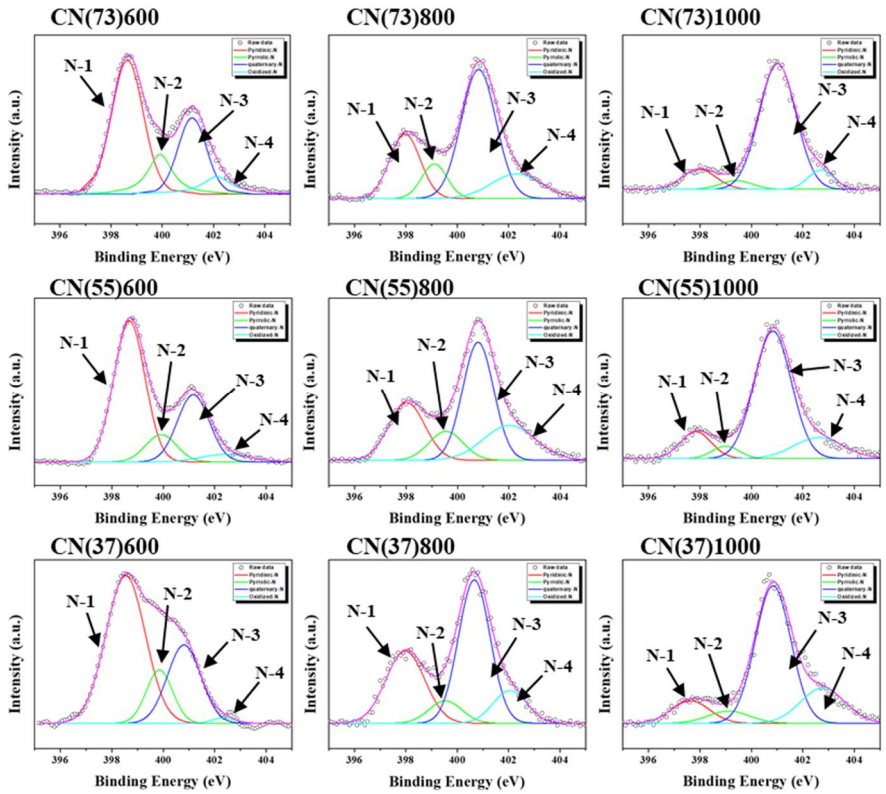

Figure 13. XPS analysis of N 1s spectra of CNs synthesized at 600 to 1000 ℃. Each spectrum is deconvoluted into four peaks: N-1: $N_{pyridinic}$, N-2: $N_{pyrrolic}$, N-3: $N_{quaternary}$, and N-4: $N_{oxidized}$, respectively.

Table 1. Summary of corresponding pore properties (BET surface area and pore volumes) and nitrogen analysis by XPS of $Ti(C_{1-x},N_x)$ solid solution chlorinated at different temperature.

Samples	Yields (%)	BET				XPS		
		Specific Surface Area (m^2/g)	Total Pore Volume (cm^3/g)	Micropore Volume (cm^3/g)	Mesopore Volume (cm^3/g)	Pyridinic, 398 eV (%)	Quarternary-N, 401 eV (%)	Nitrogen (at.%)
TiC-CDC600	102	1179.8	0.5850	0.5232	0.0317	-	-	-
TiC-CDC800	100	1330.7	0.6893	0.5864	0.0526	-	-	-
TiC-CDC1000	97	1662.3	0.8767	0.6673	0.1419	-	-	-
TiC-CDC1200	91	1187.3	0.7704	0.4327	0.3069	-	-	-
CN(73)600	32	735.05	0.5162	0.2796	0.1605	46.75	28.92	8.92
CN(73)800	41	1807.1	1.6448	0.6121	0.9158	17.71	53.32	5.42
CN(73)1000	55	1030.3	1.1068	0.3648	0.5347	10.94	66.57	3.29
CN(73)1200	61	640.34	0.7812	0.2292	0.3870	N/A	N/A	N/A
CN(55)600	20	582.41	0.5914	0.2304	0.3610	50.32	23.99	12.34
CN(55)800	36	1096.8	1.4327	0.3828	0.4555	17.75	52.72	5.69
CN(55)1000	42	743.19	0.8982	0.2649	0.3159	12.44	69.27	4.1
CN(55)1200	45	381.29	0.5308	0.1366	0.2096	-	-	-
CN(37)600	0.8	-	-	-	-	49.2	28.8	2.95
CN(37)800	9.0	842	3.6770	0.3160	0.7050	24.1	54.4	7.92
CN(37)1000	25.5	442	1.1780	0.1630	0.3480	6.5	15.7	4.02
CN(37)1200	25.8	126	0.5300	0.0470	0.1250	6.0	18.0	2.33

3.1.5. Morphology of carbonitride-derived carbons

TEM analysis was used to investigate the morphology of obtained nitrogen-doped porous carbon. Figure 14 shows the TEM image of TiC-CDCs and CNs chlorinated between 600 to 1200 ℃ for 3 hours. The resulting morphology of TiC-CDCs and CNs are almost the same in shape and volume as those of starting material due to conformal reaction. [16, 18] In addition, short-range ordered (002) carbon with interlayer distance of 0.34 – 0.36 nm (confirming the turbostratic characteristic) become aligned and interlayer distance decreases down to 0.335 nm with increase in chlorination temperature, as observed in Figure 15. Note that, CN(37)600 experience structural collapse, leaving carbon sheets only. These CN(37)600 only yielded less than 1 %, suggesting that the remaining products are leftovers from decomposed unstable carbons, or infinitesimally crystallized carbon due to impurities. This explains the observations of highly defected D'-peak from Raman spectra in Figure 9(d). On the other hand, chlorination reaction at 800 ℃ or above shows that with increase in nitrogen contents in $Ti(C_{1-x},N_x)$ from x = 0.0, 0.3, 0.5, and 0.7, gradual formation of hollow carbon granule can be observed.

In order to investigate the developing sequence of hollow carbon, $Ti(C_{0.3},N_{0.7})$ was chlorinated at 600 and 800 ℃ for a different time interval (10, 30, 90 minutes) and further characterized by TEM. The results are presented in Figure 16. In case for CN(37)600, a highly porous carbon shells around the unreacted $Ti(C_{0.3},N_{0.7})$ core (see Figure 16(a)) was produced in the first 10 minutes of chlorination process. With increasing the chlorination reaction time up to 30 minutes, these porous carbon shells leaving noticeable mesopores were destructed and the core of titanium carbonitrides (Figure 16(b)) was further decomposed. In

90 minutes of chlorination process at 600 ℃, the removal of Ti (Figure 16(c)) was almost completed, severe carbon decomposition occurred, and highly defected carbon sheets were obtained. Chlorination reaction at 800 ℃ for 10 minutes illustrated formation of carbon shells around the unreacted $Ti(C_{0.3},N_{0.7})$ core (Figure 16(a)) like the case at 600 ℃. At 800 ℃, the active carbon seemed to begin to nucleate on the $Ti(C_{0.3},N_{0.7})$ surface and produce more ordered carbon shell. Further chlorination reaction up to 30 minutes at 800 ℃ shows hollow carbon shells containing smaller $Ti(C_{0.3},N_{0.7})$ core (Figure 16(e)) than earlier stage. Continuing reaction up to 90 minutes (Figure 16(f)) almost completed the carbonitride-to-carbon structure. No significant change in the shell thickness of obtained carbon can be observed.

The results of the present work can be important contribution to the application of CDC materials, because of increasing potential for nitrogen-doped carbon materials in energy conversion and storage devices. [75] The significance of this study is that, pore size engineering from micro- to macroporous (hollow) nitrogen-doped carbon materials was synthesized by simply controlling the nitrogen composition $Ti(C_{1-x},N_x)$ starting material. Among them, nitrogen-doped hollow structured carbon was obtained by chlorination reaction of nitrogen-rich starting material, $Ti(C_{0.3},N_{0.7})$. Despite its moderate specific surface area (840 m^2/g), relatively high amount of nitrogen is well-retained within the carbon network even after 800 ℃ of chlorination reaction.

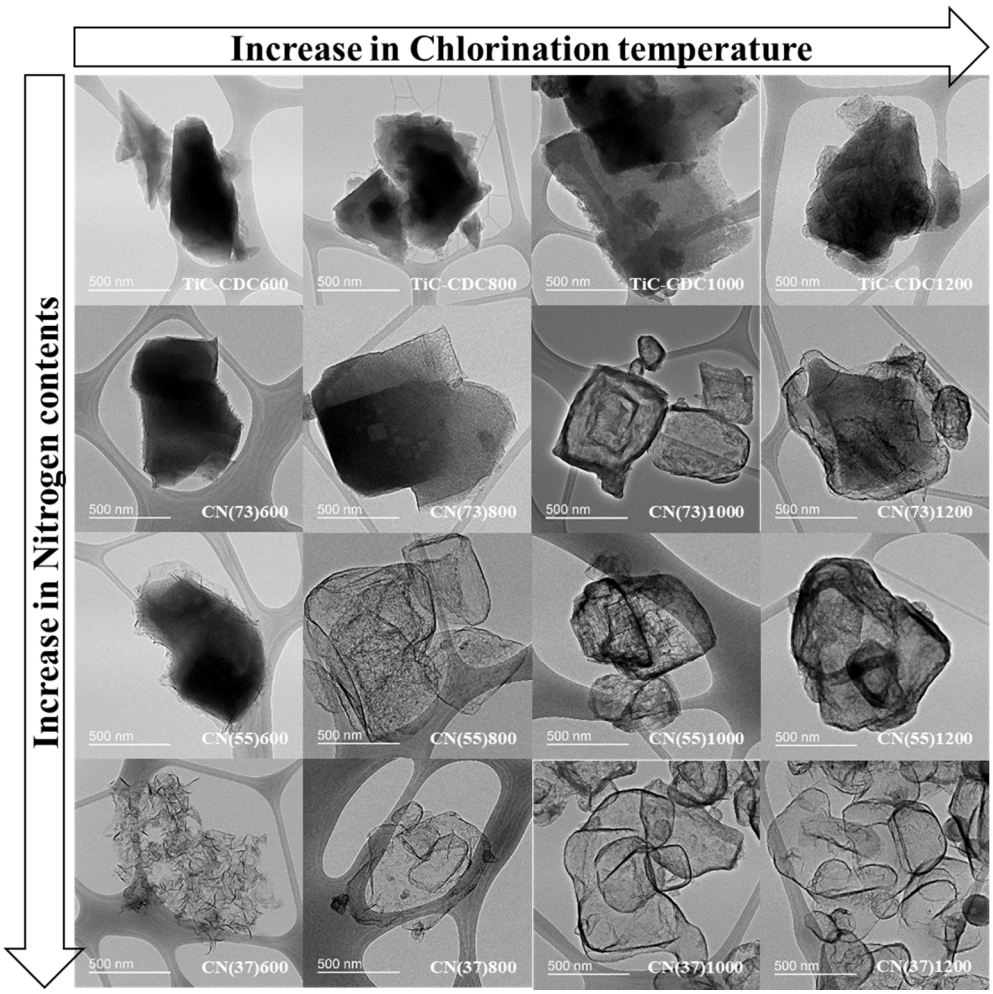

Figure 14. TEM images of TiC-CDC and CN synthesized at 600 to 1200 ℃ (All images are taken in same magnifications).

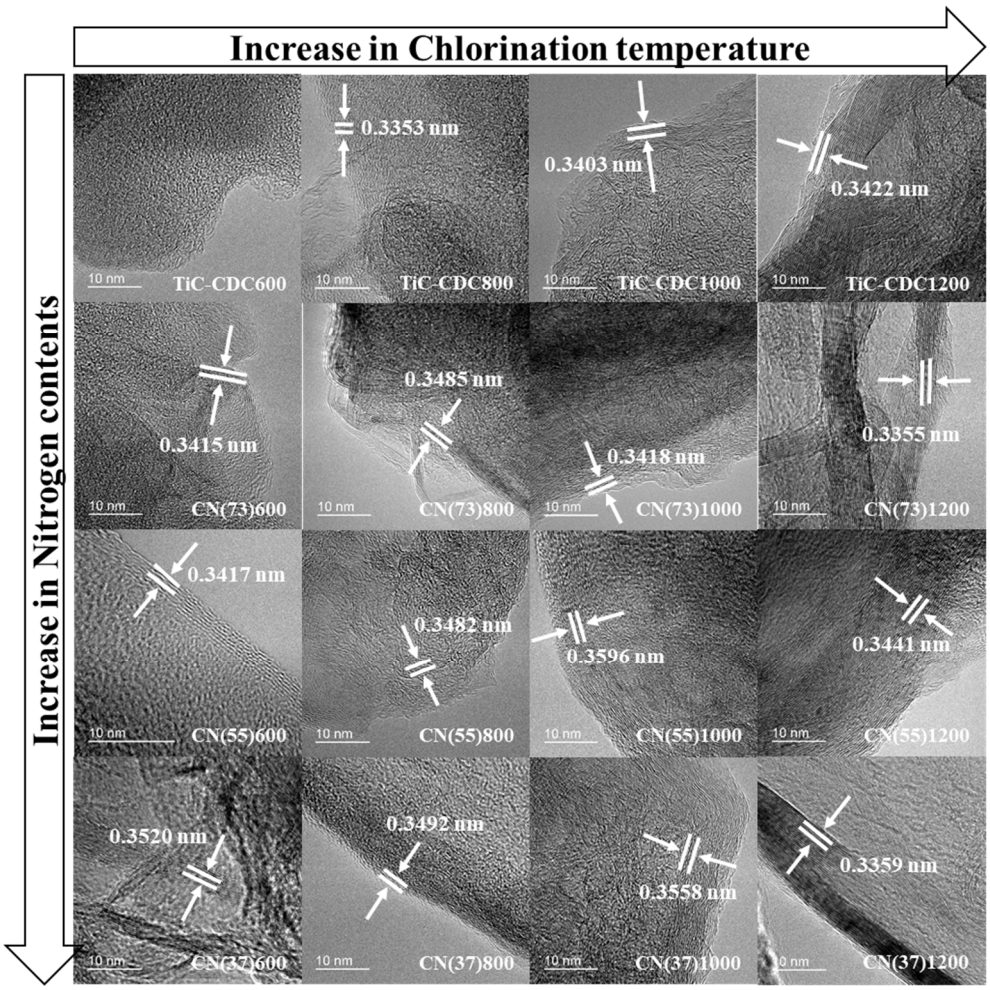

Figure 15. HRTEM image of TiC-CDC and CN synthesized at 600 to 1200 ℃.

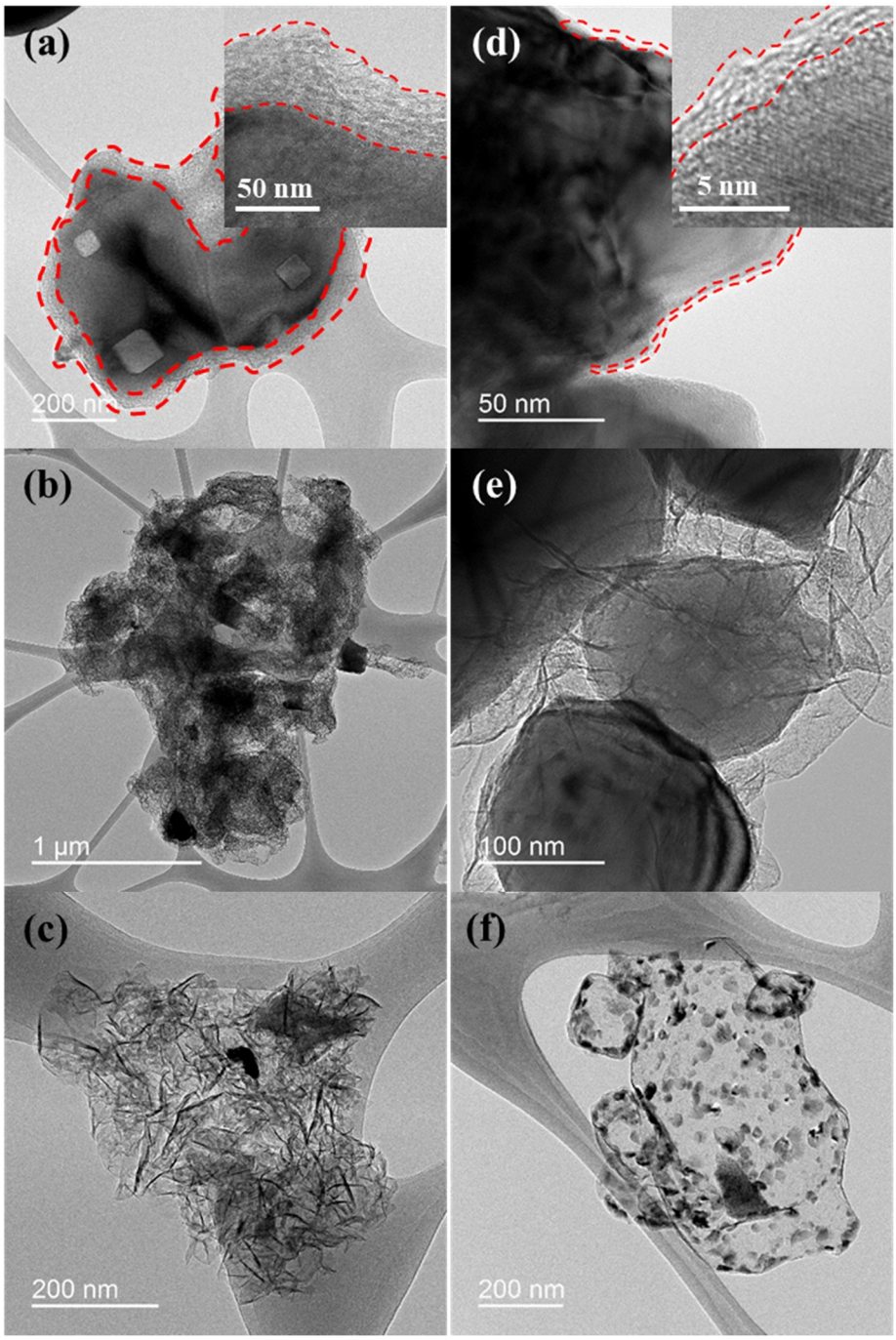

Figure 16. TEM image of CN(37)600 (a – c) and CN(37)800 (d – f) chlorinated for 10, 30, and 90 minutes.

3.1.6. Chlorination mechanism of titanium carbonitride: Formation of nitrogen-doped hollow carbon structure

The overall chlorination reactions of TiC and $Ti(C_{1-x},N_x)$ solid solutions can be expressed as followings:

$$TiC_{(s)} + 2Cl_{2(g)} \rightarrow TiCl_{4(g)} + C_{(s)} \quad (1)$$

$$Ti(C_{1-x},N_x)_{(s)} + 2Cl_{2(g)} \rightarrow TiCl_{4(g)} + x(1-z)/2N_{2(g)} + xCN_{z(s)} + (1-2x)C_{(s)} \quad (2)$$

Compared to the chlorination of TiC in reaction (1), nitrogen loss is considered in reaction (2) due to the formation of N_2 or CN_z gases species. It is also possible to form CCl_4, C_xN_y and ClCN gases. [55]

In order to understand the chlorination reaction process more comprehensively, thermodynamic calculations for the chlorination of $Ti(C_{0.7},N_{0.3})$ and $Ti(C_{0.3},N_{0.7})$ at 600 and 800 ℃ were performed using the FactSage thermodynamic software [54] and the results are presented in Figure 17. The present thermodynamic calculations considered the full thermodynamic equilibrium of system. Non-ideal Ti(C,N) solid solutions [76] was also considered for more accurate description of the chemical reaction of carbonitride with Cl_2 gas. As the thermodynamic Gibbs energy of nano-sized amorphous-carbon materials is difficult to define, graphite (bulk crystalline carbon) was used to represent carbon: In reality, the Gibbs energy of carbon materials from the present experimental study should be more positive than that of graphite because the carbon materials obtained in the chlorination is chemically more active than graphite. No nitrogen doping to carbon was taken into account as such surface bonding of carbon is not considered in the FactSage thermodynamic database yet. As the doped nitrogen content is relatively small, however, the calculated results can still give the overall

picture of chlorination reaction process.

Although the amounts of reaction products can be varied by chlorination temperature, amount of incoming Cl_2 gas and starting titanium carbonitride materials, the overall feature of the chlorination process seems to be similar. In the early stage of chlorination process where only small amount of Cl_2 gas is fed, Cl_2 gas reacts with titanium carbonitride phase and produces solid C, $TiCl_4$ and N_2 gas. After the completion of degradation of carbonitride, C can react back with Cl_2 to form CCl_4 gas phase and the amount of C product can decrease. The formation of CCl_4 gas is much significant at lower chlorination temperature. This explains much lower yields of $Ti(C_{0.7},N_{0.3})$ and $Ti(C_{0.3},N_{0.7})$ chlorination at 600 ℃ than that of 800 ℃. It should be also noted that the amount of ClCN gas is much smaller than CCl_4 gas.

In order to understand the role of nitrogen in the chlorination process, the early stage of chlorination process should be more carefully analysed. As can be seen in Figure 17, TiC component in the carbonitride reacts with Cl_2 gas prior to TiN component in both $Ti(C_{0.7},N_{0.3})$ and $Ti(C_{0.3},N_{0.7})$ regardless of temperature. This happen because TiC is chemically less stable than TiN. Thermodynamically, the following internal equilibrium in the carbonitride solution can be considered:

$$TiC_{s.s} + N_{2\,(g)} = TiN_{s.s} + C_{\,(s)} \qquad (3)$$

where $TiC_{s.s}$ and $TiN_{s.s}$ represent the carbide and nitride components in titanium carbonitride solid solution. This calculation result indicates the possibility that TiN can still exist for a short time after TiC is reduced to carbon and partial carbon network is formed at the surface in early chlorination process. Then, when TiN is decomposed by Cl_2 gas, nitrogen atoms may interact with existing carbon network to form nitrogen-doped carbon structure. This sequential chlorination process of

TiC and TIN will certainly help to retain more nitrogen in carbon structure. According to the reaction (3), the sequential chlorination process can be even further controlled by the partial pressure of nitrogen. For example, when partial pressure of N_2 gas can be increased by increasing total pressure, the TiN decomposition can be further delayed, which may be more effective for nitrogen doping in carbon network.

Based on the experimental observation and thermodynamic calculation results, the chlorination process of titanium carbonitride solid solution can be summarized as following, and schematically presented in Figure 18:

(a) TiC: In the entire temperature range, TiC can be gradually converted to carbon with development of only micropores. The chlorination processes of TiC and other metal carbides have been well explained by shrinking core mechanism. [77-79]

(b) Ti(C,N) with low nitrogen content: In general, this chlorination process is similar to that of TiC. However, because most of nitrogen in the Ti(C,N) lattice should be changed to N_2 gas during chlorination process, the vacancy site generated by the removal of nitrogen can contribute to the development of larger micropores than TiC-CDCs and even mesopores. As summarized in PSD in Figure 12 and Table 1, increasing in pore size and pore volume can be found.

(c) Ti(C,N) with high nitrogen content: When nitrogen content in the strating Ti(C,N) solid solution is high enough (in the present study, $Ti(C_{0.3},N_{0.7})$), hollow carbon material can be produced. In the early stage of the chlorination process, as explained in above thermodynamic analysis, Ti associated with C is dissociated to $TiCl_4$ gas prior to the dissociation of TiN to $TiCl_4$ and N_2 gas.

This sequential reaction process of TiC and TiN can help to retain more nitrogen in carbon network at the surface of titanium carbonitride. In comparison to low nitrogen starting materials $Ti(C_{0.7},N_{0.3})$, larger pores are developed in carbon materials starting from $Ti(C_{0.3},N_{0.7})$ because the higher amount of nitrogen can generate more vacancy sites. Larger pore in the carbon shell can accelerate the chemical reaction between carbon shell and Cl_2 gas due to large surface reaction area. For example, highly porous disordered carbon shell can be generated at low temperature (600 ℃ in this study) by the chemical reaction between carbon and Cl_2 gas to produce CCl_4 gas, as explained in the thermodynamic calculations (see Figure 17). Such phenomenon is less significant in low nitrogen content titanium carbonitride materials. Such large pores in the carbon shell at the surface of Ti(C,N) can also play a role as channels for Cl_2 gas to meet unreacted Ti(C,N) materials below the carbon shell. Then, Cl_2 gas can continuously chlorinate Ti(C,N) inside of carbon shell. The enhanced chemical reaction of Cl_2 gas with inner Ti(C,N) can make it possible to disconnect the atomic bonding between unreacted Ti(C,N) core and pre-formed surface carbon shell. As chlorination process proceeded, the more pore channels will be generated at the inner Ti(C,N) particle, and even break down the particles into small pieces (see Figure 16(f) at 90 minutes). This chlorination process eventually produce a hollow carbon structure. The hollow carbon materials can be graphitized at high temperature such as 1200 ℃ (see Figure 14 and Figure 15). At low temperature (600 ℃), no hollow carbon can be observed because the severe chemical reaction between carbon and Cl_2 gas after the chlorination of Ti. It should be noted that this chlorination reaction mechanism for high nitrogen

Ti(C,N) materials is solely from etching process and it is complete different from the simple shrinking core mechanism for TiC.

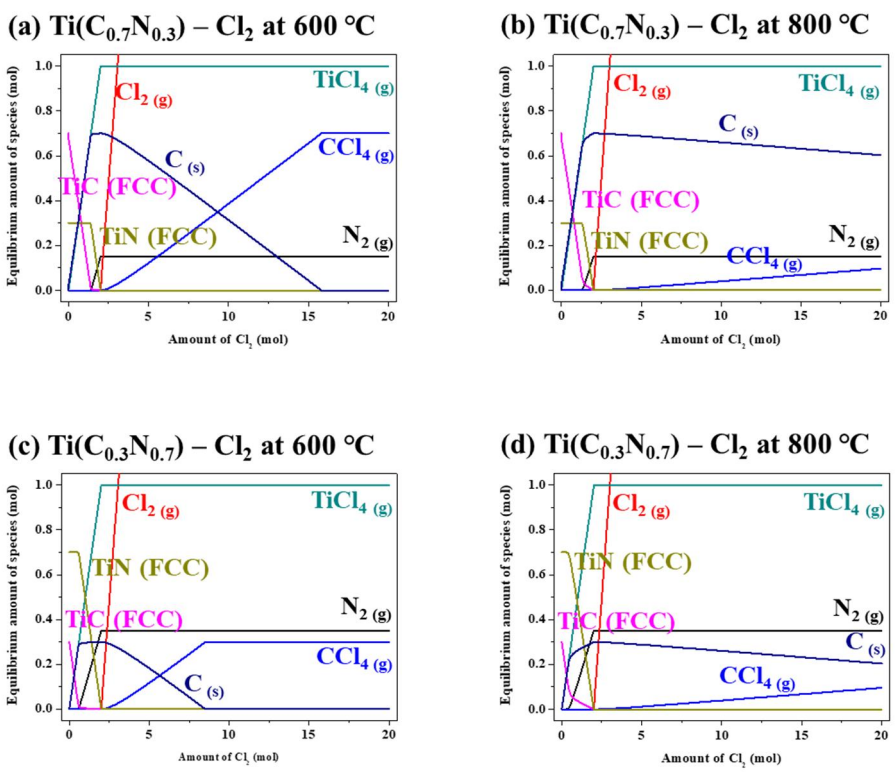

Figure 17. Thermodynamic calculation results of the chlorination of $Ti(C_{0.7},N_{0.3})$ (a – b) and $Ti(C_{0.3},N_{0.7})$ (c –d) at 600 and 800 ℃.

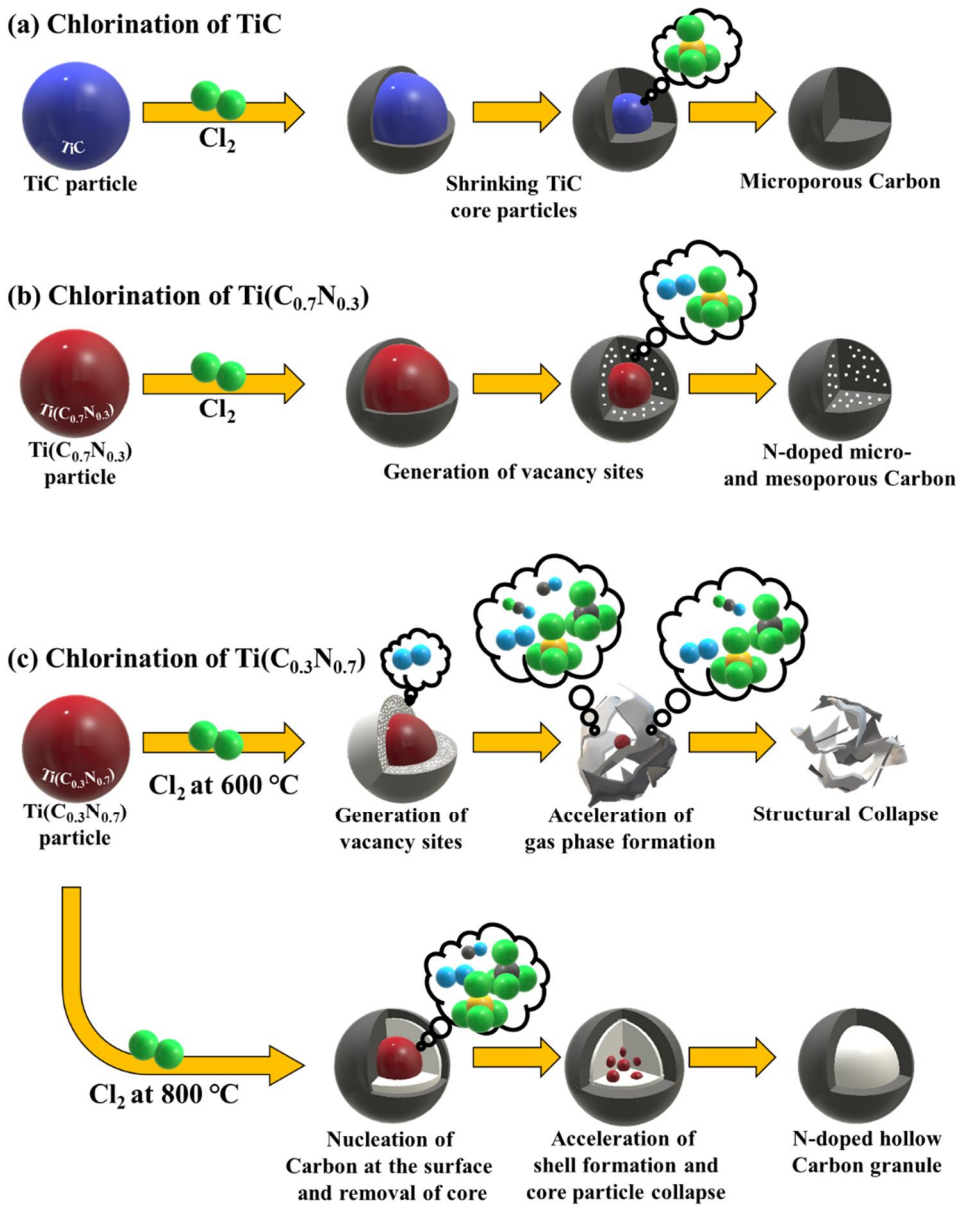

Figure 18. Formation mechanism of (a) TiC-CDC, (b) CN(73), and (c) CN(37)600 and CN(37)800, where yellow, green, and grey balls represent Ti, Cl, N, and C atoms, respectively.

3.1.7. Application of N-doped porous carbon materials

Nitrogen-doped porous carbon having hierarchical pore structure, from micro- to mesopores, is known to enhance the charge storability for a high power applications by allowing efficient mass transport through the pores. [8] In addition, introduction of heteroatoms such as nitrogen could further enhance the charge storability of carbon material in Electrochemical Double-Layer Capacitances (EDLCs). Hence, the electrochemical capacitance behaviour for CNs are analysed based on the cyclic voltammetry (CV) profiles using equation (2). For comparison, TiC-CDC800 was also analysed. Samples obtained at 800 ℃ were chosen for this study due to their largest BET SSA and the highest nitrogen contents. The calculated gravimetric and volumetric capacitances are depicted in Figure 19. According to the results in Figure 19(a), the highest gravimetric capacitance at scan rate of 1 mV/s was achieved from CN(73)800 (194.3 F/g) with the highest BET SSA, followed by CN(55)800 (161.9 F/g), TiC-CDC800 (154.4 F/g), and CN(37)800 (120.6 F/g). On the other hand, CN(37)800 showed the lowest performances among these four samples at low scan rates even though it possesses the highest nitrogen content among the samples. The low BET SSA and larger macropore development may be the reason for such low performance. Figure 19(b) displays the electrochemical impedance spectroscopy (EIS) spectra for this work. The Nyquist plots of the CNs consist of a small semicircle at high frequency and almost vertical line at low frequency. All samples, including TiC-CDCs, intercept Z_{Re} at very high frequency with low R_s values of 0.62 – 0.71 Ω, which corresponds to electric series resistance (ESR). The low ESR indicates the higher electrical conductivity of the carbon electrodes, and the lowest ESR was achieved from

CN(37)800. The diameter of the semicircle on the Z_{Re} axis in the high frequency region referred to the polarisation resistance (R_{ct}) is associated with the surface properties of the porous electrode, corresponding to the interfacial faradic charge transfer resistance. The lowest R_{ct} was also observed from CN(37)800 (0.72 Ω) . The relatively low internal resistance of CN(37)800 in 6 M KOH aqueous solution indicates the high mass transfer/diffusion rate of ions into the pores. Such reduced resistance is due to the improved electric conductivity of the carbon material from nitrogen doping that facilitates the charge transfer between electrode and electrolyte at much faster rate, resulting decrease in R_{ct}. The volumetric performance of energy storage device is also an important factor especially for microscale devices applications. In Figure 19(c), the capacitance of all CNs markedly decreased only by converting to volumetric measurements. Chlorination of titanium carbonitride phase induces larger voids that are developed from N_2 gas. Moreover, these larger voids become much severe when nitrogen contents in $Ti(C_{1-x},N_x)$ solid solution increases, in this case $Ti(C_{0.3},N_{0.7})$. On the other hand, TiC-CDC800 do not show much differences in capacitances.

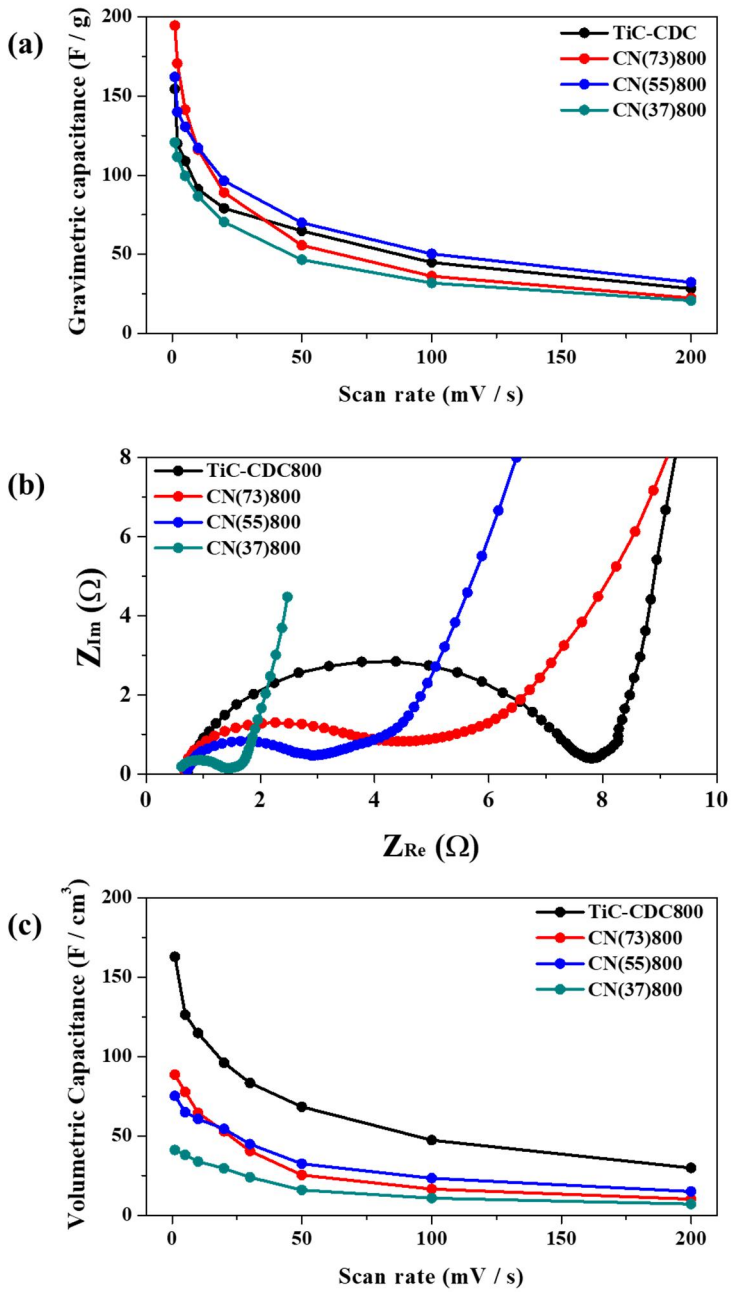

Figure 19. Calculated (a) gravimetric and (b) volumetric capacitance based on cyclic voltammogram at various scan rates, and, (c) Nyquist plots of TiC-CDC800, CN(73)800, CN(55)800, and CN(37)800.

3.1.8. Conclusions

Nitrogen-doped porous carbon materials were investigated by chlorination reaction of $Ti(C_{1-x},N_x)$ solid solutions, where x = 0.0, 0.3, 0.5, 0.7 at the temperatures from 600 to 1200 ℃. The amount of N-doping increased with nitrogen contents in the starting materials $Ti(C_{1-x},N_x)$. As high as 12.3 at.% N-doping content was obtained from the chlorination of $Ti(C_{0.5},N_{0.5})$ at 600 ℃, and 7.9 at.% N from $Ti(C_{0.3},N_{0.7})$ at 800 ℃. The highest BET specific surface area (1807.1 m^2/g) and total pore volume (1.6 cm^3/g) were achieved with CN(73)800. Moreover, nitrogen-doped hollow carbon structure using a single-step chlorination process was achieved from $Ti(C_{0.3},N_{0.7})$ at 800 ℃. The study demonstrates that pore structure from highly microporous-rich to meso- and macropore can be achieved by controlling the nitrogen contents in starting titanium carbonitride solid solution, without any physical or chemical post-treatment.

Furthermore, the electrochemical behaviour of the supercapacitor was analysed. The nitrogen-doped porous carbon from CN(73)800 exhibit an enhancement of gravimetric capacitance over the conventional TiC-CDC. However, by simply converting to volumetric measurement, all CNs show markedly decrease in volumetric capacitance. Although lowest capacitance was found from CN(37)800, it illustrate the highest electrical conductivity and highest charge transfer between electrode and electrolyte at much faster rate due to high amount of nitrogen contents.

3.2. Core-shell structured carbonitride-derived carbon via pre-vacuum annealing with enhanced double-layer capacitance

3.2.1. Motivation

In section 3.1 synthesis of N-doped porous carbon was successfully achieved by chlorination reaction of $Ti(C_{1-x},N_x)$ solid solution (where x = 0.0, 0.7, 0.5, 0.3). After chlorination reaction at 800 ℃, the highest BET SSA (~1800 m^2/g) was obtained from the low nitrogen containing $Ti(C_{0.7},N_{0.3})$ solid solution, whereas, highest nitrogen doping contents (~8 at.%) with hollow structured carbon was produced from high nitrogen containing $Ti(C_{0.3},N_{0.7})$ solid solution. Consequently, highest gravimetric capacitance was achieved from CN(73)800, whereas, the lowest performance was shown from CN(37)800. However, all CNs exhibited poor performance when converted to volumetric capacitance.

Although lowest capacitance was found from CN(37)800, the high rate-dependent charge storability from development of larger pores and high amount of nitrogen dopants makes this material very appealing properties. However, low micropore volume from CN(37)800 may also hinder from achieving high EDLC performance. Therefore, a modification was requisite. Jung et al. [80] calculated the Gibbs energy of $Ti(C_{1-x},N_x)$ solid solution at various temperatures and reported that TiN became stable at T <1500 K and TiC became stable at T > 1500 K. Hence, in this section, we have systematically engineered the pore structure of carbon by vacuum-annealing of $Ti(C_{0.3},N_{0.7})$ in order to modify the C/N ratio in $Ti(C_{0.3},N_{0.7})$ starting material prior to chlorination reaction. Yeon et al. [81] has recently

reported the effect of high temperature pre-vacuum-annealing of TiC starting material prior to chlorination process during this manuscript preparation. However, their work did not concern any vacuum-annealing nitrogen containing Ti(C,N) solid solution, and the resulting capacitance only focused on gravimetric capacitance.

3.2.2. Vacuum-annealing of $Ti(C_{0.3},N_{0.7})$

Powder SEM analysis results of as-received TiC and $Ti(C_{0.3},N_{0.7})$, and vacuum-annealed $Ti(C_{0.3},N_{0.7})$ are illustrated in Figure 20. The particle size of as-received powders ranges from sub-micron to 2 μm, as can be seen in Figure 20(a – b). On the other hand, vacuum-annealed $Ti(C_{0.3},N_{0.7})$ powders have more uniform size distribution. The average particle size of vacuum-annealed powders also becomes larger with higher temperature, as shown in Figure 20(c – d). Such increase in the particle size can be explained by the Ostwald ripening process.

The results of powder XRD analyses of as received TiC and $Ti(C_{0.3},N_{0.7})$, and vacuum-annealed $Ti(C_{0.3},N_{0.7})$ at 1600 and 1800 ℃ for four hours are presented in Figure 21. The XRD results of as-received powders match well with JCPDS 32-1383 for TiC and JCPDS 42-1488 for $Ti(C_{0.3},N_{0.7})$. On the other hand, vacuum-annealed $Ti(C_{0.3},N_{0.7})$ sample at 1600 ℃ shows a small additional peaks at about 36°, 42°, and 60° (Figure 21(c), pointed with arrows) along with the original $Ti(C_{0.3},N_{0.7})$ peaks. Vacuum-annealed sample at higher temperature (1800 ℃) also shows these extra peaks with much higher intensity (Figure 21(d), pointed with arrows). In fact, these extra peaks are close to TiC. That is, during the vacuum-annealing of $Ti(C_{0.3},N_{0.7})$ samples, a phase separation from nitrogen-rich $Ti(C_{0.3},N_{0.7})$ to form nitrogen-lean $Ti(C_{0.3},N_{0.7-x})$ happens. This is also consistent with our EA results (see Figure 22) which show the decrease in nitrogen content in the samples after vacuum annealing.

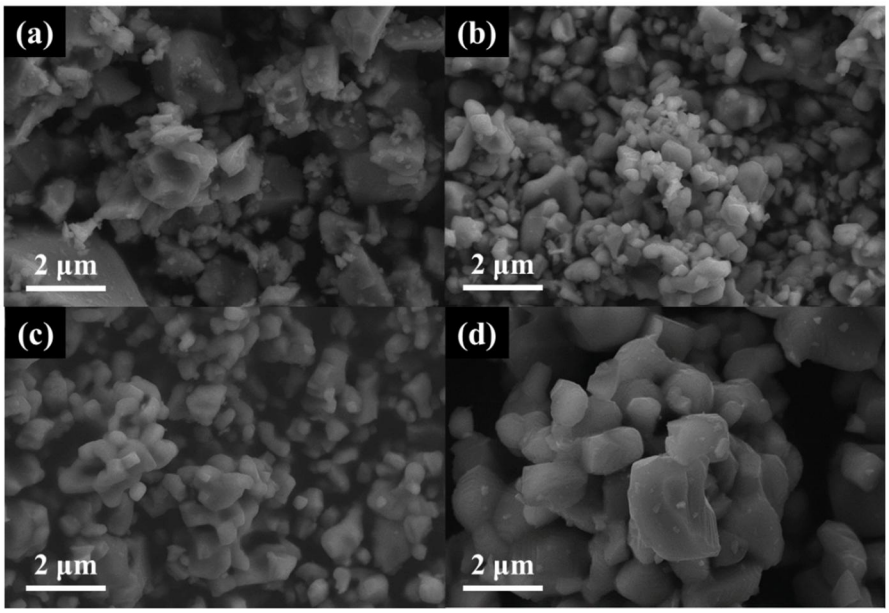

Figure 20. SEM images of (a) as-received TiC, (b) as-received $Ti(C_{0.3},N_{0.7})$, (c) $Ti(C_{0.3},N_{0.7})$ vacuum annealed at 600 ℃-4h, and (d) $Ti(C_{0.3},N_{0.7})$ vacuum annealed at 1800 ℃-4h.

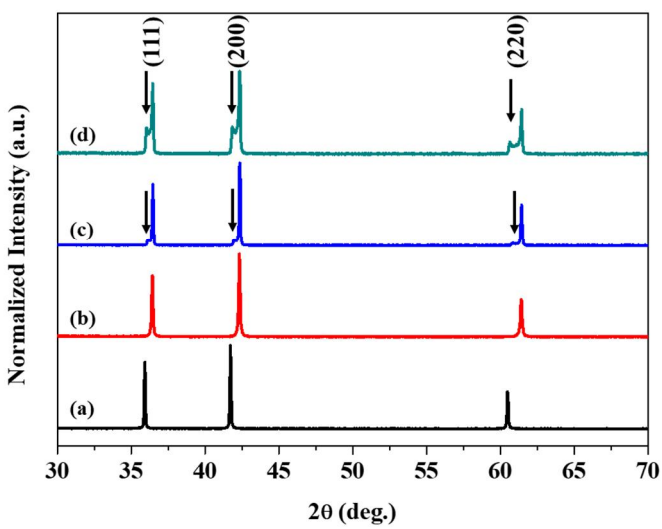

Figure 21. XRD patterns of (a) as-received TiC, (b) as-received $Ti(C_{0.3},N_{0.7})$, and $Ti(C_{0.3},N_{0.7})$ vacuum annealed at (c) 1600 ℃-4h and (d) 1800 ℃-4h.

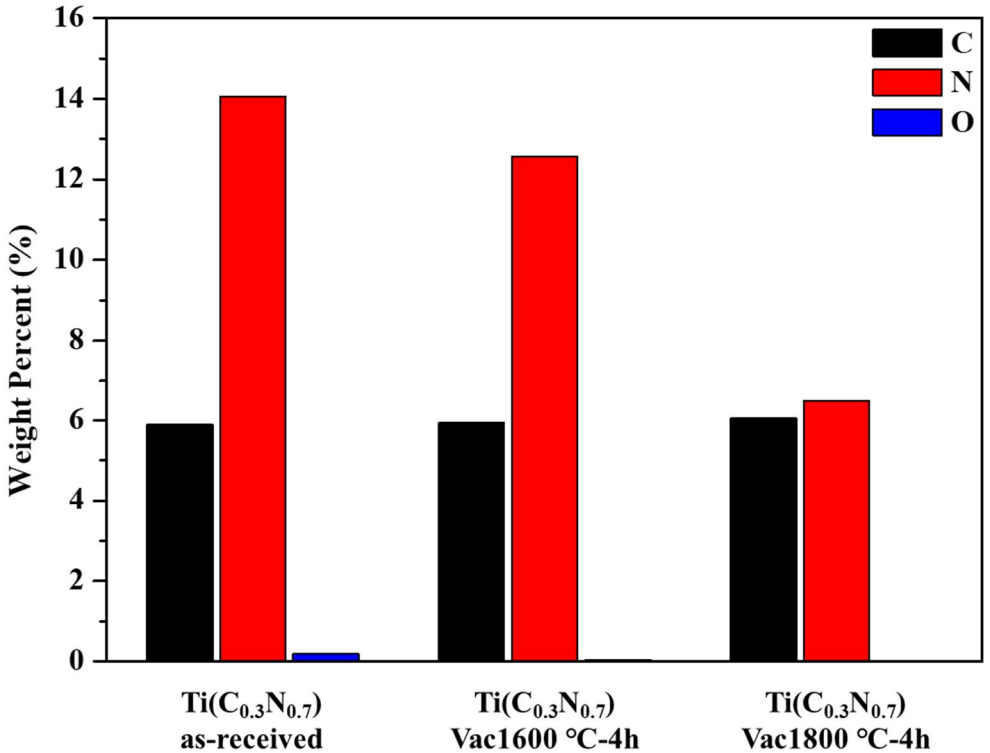

Figure 22. EA data for as-received and vacuum-annealed $Ti(C_{0.3},N_{0.7})$ at 1600 ℃-4h and 1800 ℃-4h.

3.2.3. Core-shell structured N-doped carbon

Figure 23 shows the XRD patterns of obtained carbon materials from chlorination of TiC, $Ti(C_{0.3},N_{0.7})$, and vacuum-annealed $Ti(C_{0.3},N_{0.7})$ (1600 and 1800 ℃) at 800 and 1000 ℃. In general, no secondary or unreacted phases are observed for all samples. Two broad diffraction patterns at ~26° and ~44° suggest that the obtained carbon materials are typical of turbostratic carbon. [82] In addition, as the chlorination temperature increases from 800 to 1000 ℃, the broad XRD patterns become slightly narrower, suggesting increase in carbon ordering.

The carbon ordering characteristics can be better understood with Raman spectroscopy. As illustrated in Figure 24(a – b), all samples show both D-band (~1330 cm^{-1}) and G-band (1580 cm^{-1}), which are typical characteristics of the amorphous disordered carbon materials. From Lorentzian fits, the intensity ratio of the D- and G-bands (I_D/I_G) and the full width half maximum (FWHM) of D- and G-bands of CN(37)s and pre-vacuum-annealed samples were calculated and presented in Figure 24(c). The intensity ratios were found to be more or less similar. The calculated results for TiC-CDCs are similar to the values reported in many previous literatures, [1, 18, 79, 81] so they are not shown in this study. As presented in Figure 24(c), the FWHM of D-band decreases at higher chlorination reaction temperature (1000 ℃). This means that more ordered carbon materials are synthesized by the chlorination at higher temperature, which can be confirmed from the XRD patterns obtained in Figure 23. On the other hand, the FWHM of D-band is 267 cm^{-1} for non-vacuum-annealed CN(37)800, whereas those for Vac1600@CN(37)800 and Vac1800@CN(37)800 are 287 cm^{-1} and 299 cm^{-1}, respectively. That is, pre-vacuum-annealed samples chlorinated at 800 ℃ show

broader D- and G-band FWHM than non-treated samples, which tells an increasing disorderness in the final carbon materials by pre-vacuum annealing process.

The nitrogen adsorption-desorption isotherms of TiC-CDCs, CN(37)s and pre-vacuum-annealed samples (Vac1600@CN(37)s and Vac1800@CN(37)s) synthesized at 800 and 1000 ℃ were conducted at 77 K and their corresponding pore size distributions (PSDs) are also presented in Figure 25. The corresponding TiC-CDC and CN(37) are well explained in section 3.1.4. In case of pre-vacuum-annealed chlorinated samples, all exhibit the type IV curve with H2-type hysteresis loop, similar pore structure to CN(37)s, except for Vac1800@CN(37)800. Vac1800@CN(37)800 shows larger degree of microporosity than other CN(37)s and Vac1600@CN(37)s. All PSD patterns of the pre-vacuum-annealed samples are also similar to those of CN(37)s. The micro/mesopores volume ratios can be used to illustrate how much portion of micropore volume are occupied over mesopores volume. The calculated values in the present study are 0.45 for CN(37)800, 0.68 in Vac1600@CN(37)800, and 2.98 for Vac1800@CN(37)800, indicating that micropore volume can be increased through pre-vacuum-annealing $Ti(C_{0.3},N_{0.7})$ starting material. The summary of pore texture including calculated BET SSA, total pore volume, and micro- and mesopores volume ratio are listed in Table 2.

Figure 26 shows TEM images of all carbon materials synthesized at 800 and 1000 ℃. TiC-CDC and CN(37) are also depicted for comparison and its detailed explanation can be found in section 3.1.5. When $Ti(C_{0.3},N_{0.7})$ was pre-vacuum-annealed at 1600 ℃ followed by chlorination reaction at 800 and 1000 ℃ (Vac1600@CN(37)s), similarly, hollow carbons were produced, as illustrated in Figure 26(e – f), except that particles are partially sintered together due to high temperature annealing process. On the other hand, both Vac1800@CN(37)800 and

Vac1800@CN(37)1000 illustrate an exceptional morphology, where core-shell structured carbon is observed (Figure 26(g – h)).

In general, $Ti(C_{1-x},N_x)$ solid-solutions consists of face centered cubic (FCC) lattice, a simple rocksalt structure ($Fm\bar{3}m$, 255) just like NaCl. However, depending on the synthesizing method, a various crystallographic morphology shapes with a non-equilibrium state can be attained. In Figure 27, high magnification SEM images of as-received $Ti(C_{0.3},N_{0.7})$ (Figure 27(a)), $Ti(C_{0.3},N_{0.7})$ vacuum-annealed at 1600 ℃ for 4 hours (Figure 27(b)), and 1800 ℃ for 4 hours (Figure 27(c)) are shown at same magnification. Unlike as-received $Ti(C_{0.3},N_{0.7})$ and vacuum-annealed $Ti(C_{0.3},N_{0.7})$ at 1600 ℃, vacuum annealing at 1800 ℃ induces a growth of 'steps' planes with hexagonal geometry (Figure 27(c), indicated with white arrows). The presence of the 'steps' growth with hexagonal geometry indicates that the two-dimensional nucleation growth of the {111} planes was favourable during vacuum-annealing process. [83] The 2D nucleation growth is also one of the most general growth modes known for the ceramic crystals. [84] The growth of the 'steps' is very important as the formation of graphene layers is known to nucleate on these 'step and the terraces' sites of the substrate. [85] As chlorination process is a conformal reaction, the 'steps'-like morphology from vacuum annealing is retained in the final product as illustrated in Figure 27(d). This 'steps' site allows the active carbons to nucleate during the early stage of chlorination reaction. Then, more active carbon atoms grow and cover the surface with the progress of chlorination, and finally grow into graphitic layers.

The TEM images (Figure 27(e – f) and N_2 adsorption-desorption analysis results (Table 2) of Vac1800@CN(37)800 and Vac1800@CN(37)1000 reveal that the inner core is occupied by highly microporous-rich carbons. This means that the

high temperature vacuum-annealing process at 1800 ℃ created not only these 'steps' sites, but also carbon-rich phases, $Ti(C_{0.3},N_{0.7-x})$ (see EA analysis result in Figure 22). Having carbon-rich precursor, the amount of degradation by evolution of gas phases such as CNx and/or ClCN during the chlorination reaction would be lower, [55] and as a consequence, the degree of mesoporosity decreases while the microporosity increases with increasing vacuum-annealing temperature, which also explains the change in micro-/mesopores volume obtained from N_2 adsorption-desorption analysis (see Table 2). Based on the observation in this study, the effect of vacuum annealing treatment on developments of Vac1800@CN(37)800 is schematically illustrated in Figure 28 in comparison to TiC-CDC800, CN(37)800.

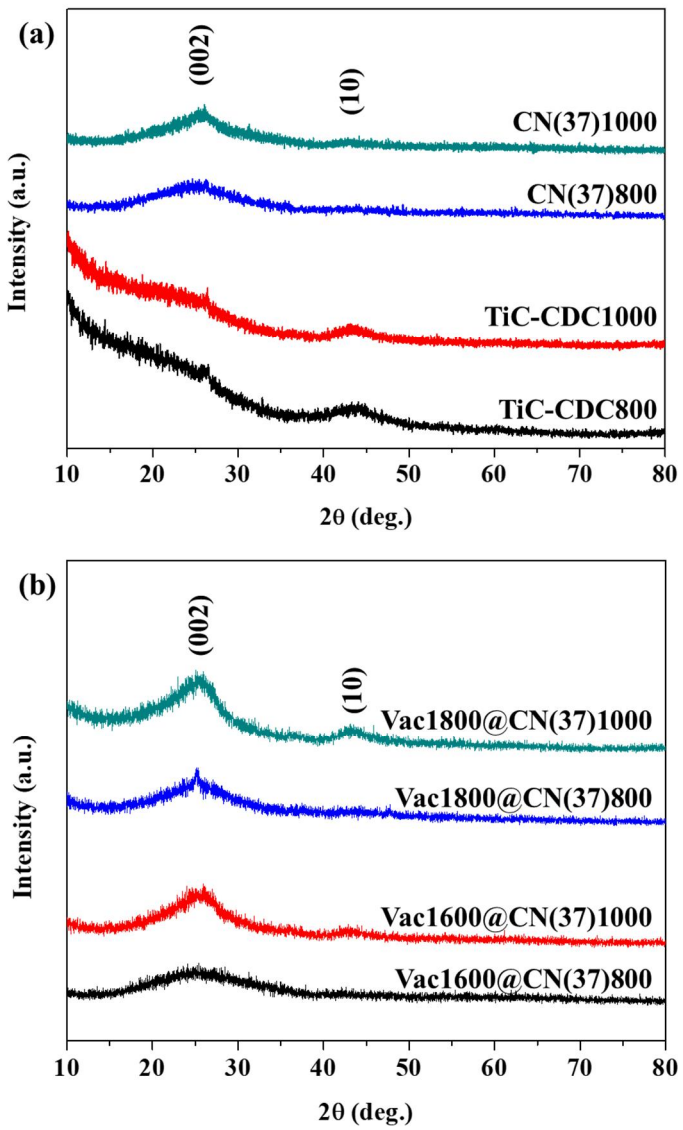

Figure 23. XRD patterns of (a) TiC-CDC and CN(37), and (b) Vac1600@CN(37) and Vac1800@CN(37) obtained from chlorination at 800 and 1000 ℃.

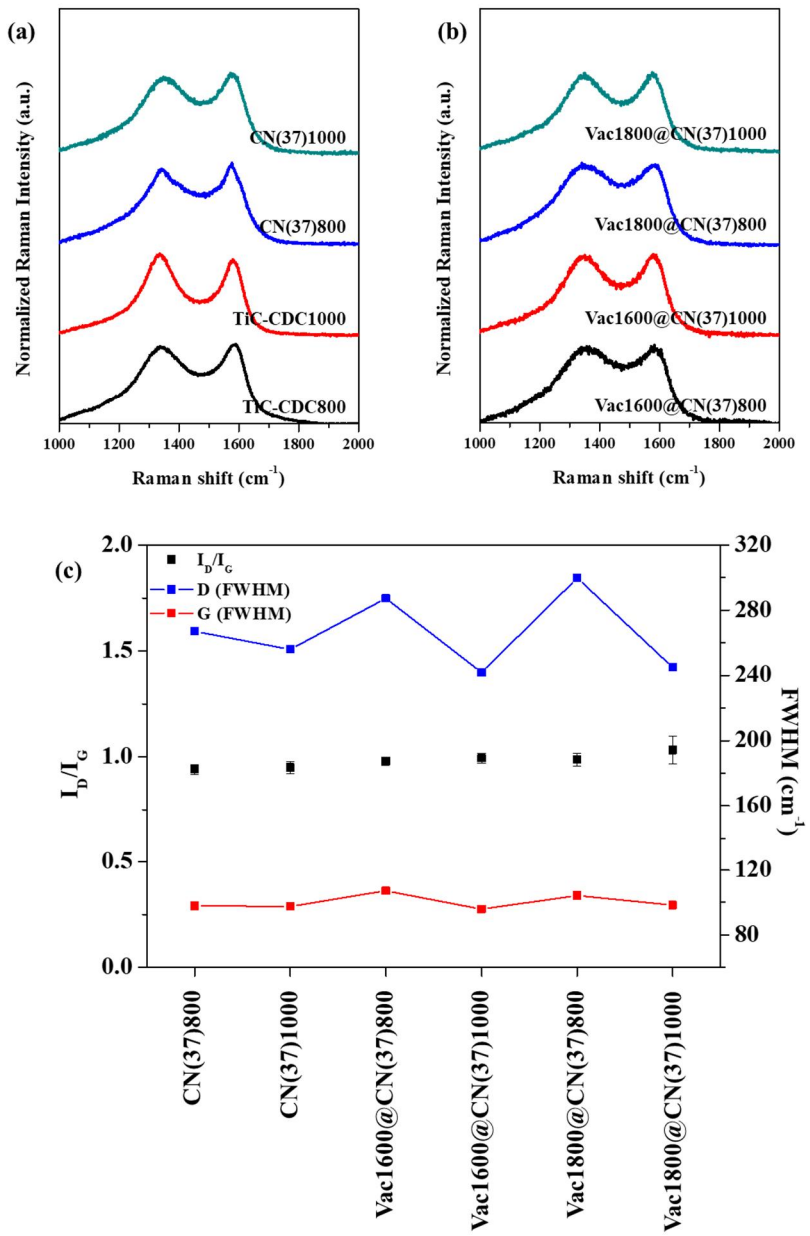

Figure 24. Raman spectra of chlorinated samples for (a) as-received and (b) vacuum annealed. (c) illustrate the I_D/I_G ratio (black line), FWHM of D-band (red line) G-band (blue line) obtained from Raman spectra for CN(37)s, Vac1600@CN(37)s, and Vac1800@CN(37)s synthesized at 800 and 1000 ℃, respectively.

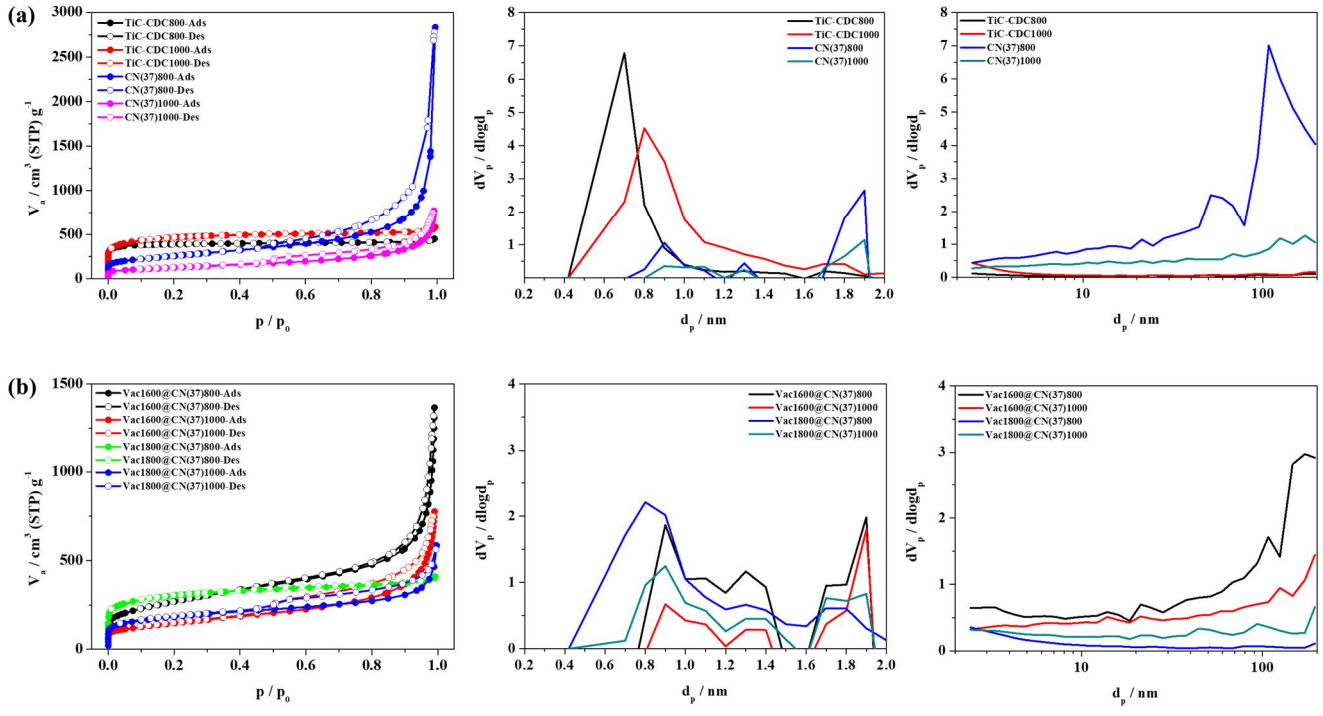

Figure 25. Nitrogen adsorption-desorption isotherms of (a) TiC-CDC and CN(37), and, (b) Vac1600@CN(37) and Vac1800@CN(37), and their pore size distribution determined by MP and BJH plots.

Table 2. Summary of BET N_2 adsorption data and nitrogen contents analysed by EA and XPS.

Precursors	SSA (m^2/g)	Total pore volume (cm^3/g)	Micropore volume (cm^3/g)	Mesopore volume (cm^3/g)	Micro/Mesopore volume ratio	N contents	
						EA (wt. %)	XPS (wt.%)
TiC-CDC800	1330	0.6893	0.5864	0.0526	11.1	-	-
TiC-CDC1000	1662	0.8767	0.6673	0.1419	4.70	-	-
CN(37)800	842	3.6774	0.3156	0.7051	0.45	6.77	8.57
CN(37)1000	441	1.1784	0.1634	0.3477	0.47	4.62	4.50
Vac1600@CN(37)800	970	2.1004	0.3539	0.5240	0.68	6.42	8.23
Vac1600@CN(37)1000	524	1.1988	0.1942	0.3713	0.52	3.90	6.08
Vac1800@CN(37)800	1079	0.6255	0.4312	0.1448	2.98	4.78	7.26
Vac1800@CN(37)1000	646	0.7458	0.2506	0.2242	1.12	3.78	6.91

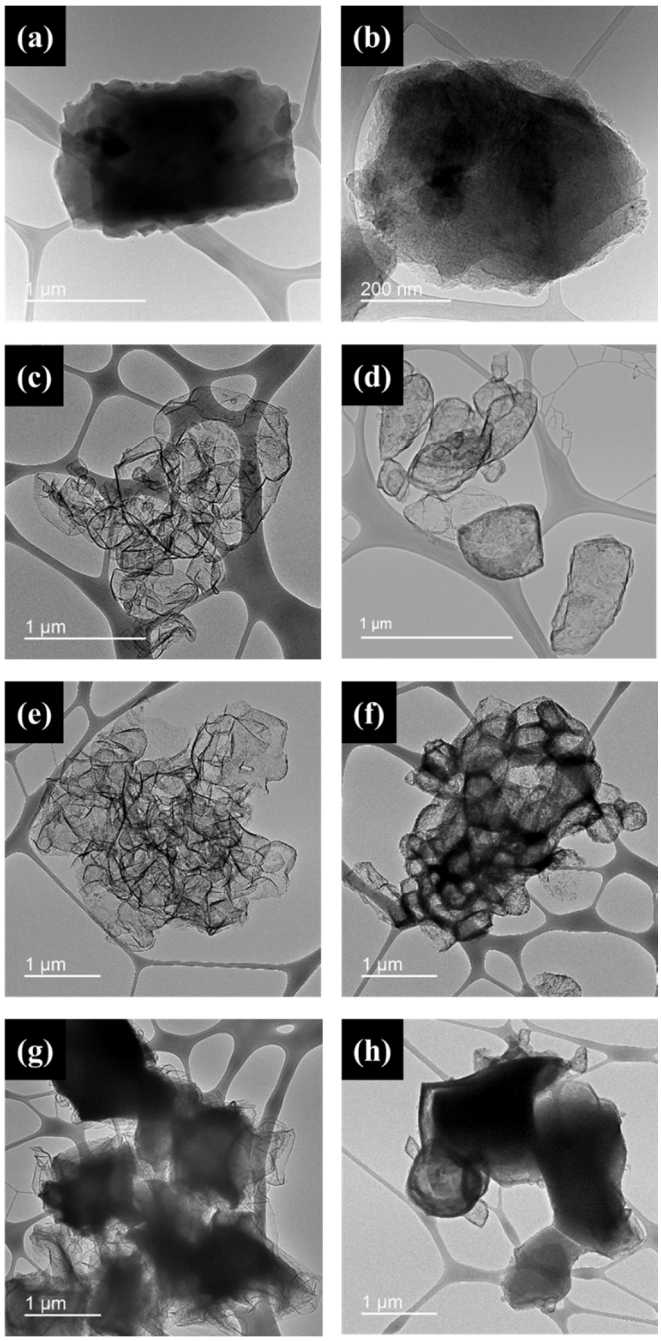

Figure 26. TEM images of (a) TIC-CDC800, (b) TiC-CDC1000, (c) CN(37)800, (d) CN(37)1000, (e) Vac1600@CN(37)800, (f) Vac1600@CN(37)1000, (g) Vac1800@CN(37)800 and (h) Vac1800@CN(37)1000.

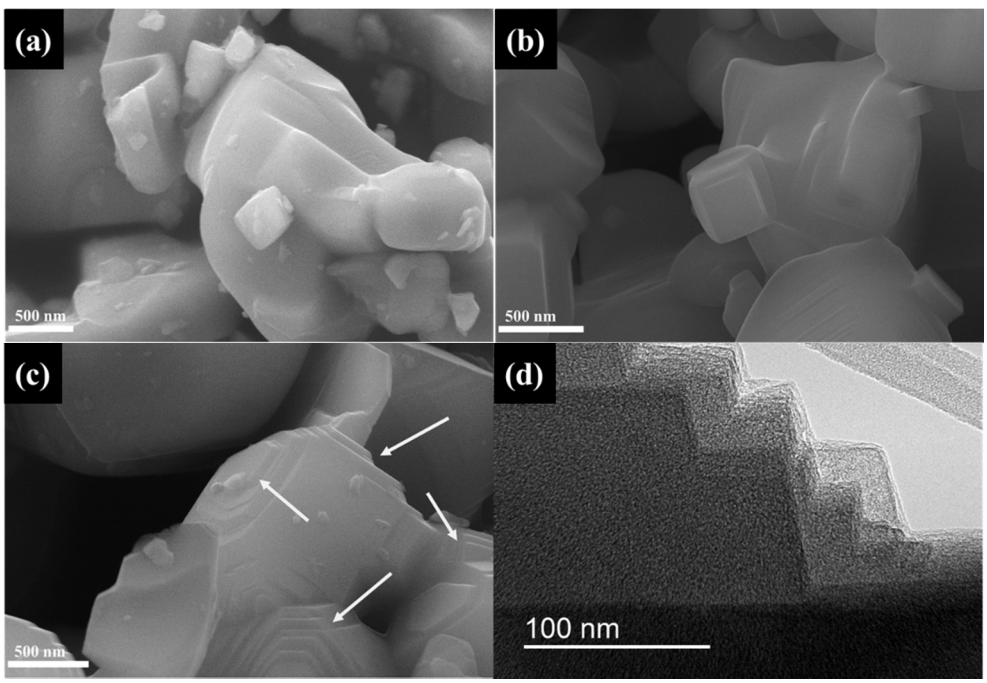

Figure 27. SEM images of (a) as-received $Ti(C_{0.3},N_{0.7})$, (b) and (c) $Ti(C_{0.3},N_{0.7})$ vacuum-annealed at 1600 and 1800 ℃ for 4 hours, respectively. (d) TEM image of 'steps' sites in Vac1800@CN(37)800.

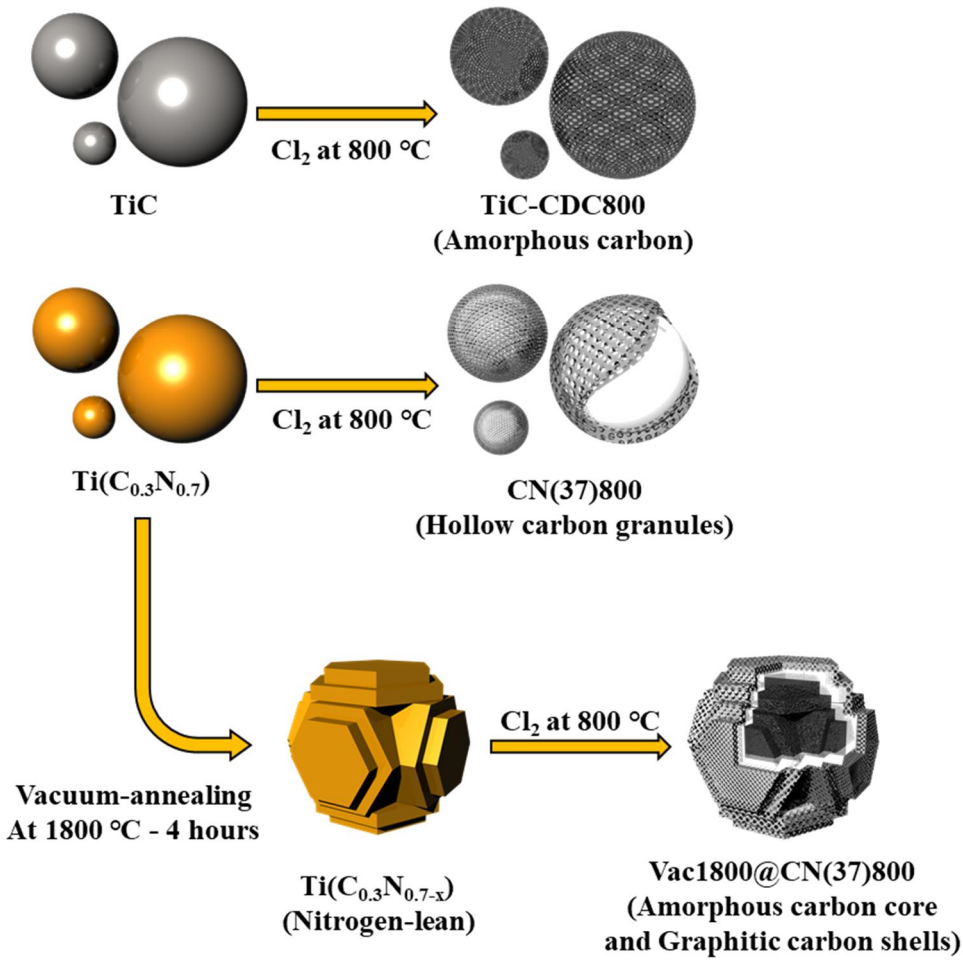

Figure 28. Schematics of proposed formation mechanisms of TiC-CDC800, CN(37)800, and Vac1800@CN(37)800.

As mentioned in the introduction, the surface chemistry of carbon electrode also plays an important role in achieving high capacitance. To determine the presence of nitrogen functionality and their bonding nature, CN(37)s and pre-vacuum-annealed samples chlorinated at 800 and 1000 ℃ were analysed by X-ray photoelectron spectroscopy (XPS). Regardless of pre-vacuum-treatment, all carbon samples synthesized at 800 ℃ exhibit about 7 ~ 8 wt.% of nitrogen doping, whereas samples at 1000 ℃ contain less nitrogen. This can be explained by the instability of nitrogen functional groups at high temperature. The elemental analysis (EA) was also used to determine the overall nitrogen contents in the samples. It is found that the nitrogen concentration on the surface (from XPS results) is slightly higher than that in bulk (from EA). In case of Vac1800@CN(37)800, a large decrease in nitrogen contents in bulk was found compared to Vac1600@CN(37)800. The high-resolution N1s core level XPS spectra for chlorinated carbon samples are analysed in Figure 29. The obtained spectra are deconvoluted into 4 peaks; pyridinic N (~398.7 eV), pyrrolic N (~400.3 eV), quaternary N (~401.2 eV), and N-oxides of pyridinic N (402.8 eV), respectively. [41] For all CNs and pre-vacuum-annealed samples consist of large amount of pyridinic N and quaternary N which is generally known for the active nitrogen functionalities for the application of supercapacitors. [86] However, as shown in Figure 29, increasing chlorination temperature decreases pyridinic N functional group, but increases N-oxides of pyridinic N. It was reported that high temperature annealing increases the incorporation of oxygen to form carbonyl and ether groups, [87] thus, increasing temperature does not always decrease oxygen content and transform relatively unstable pyridinic N at the edge carbon into N-oxides.

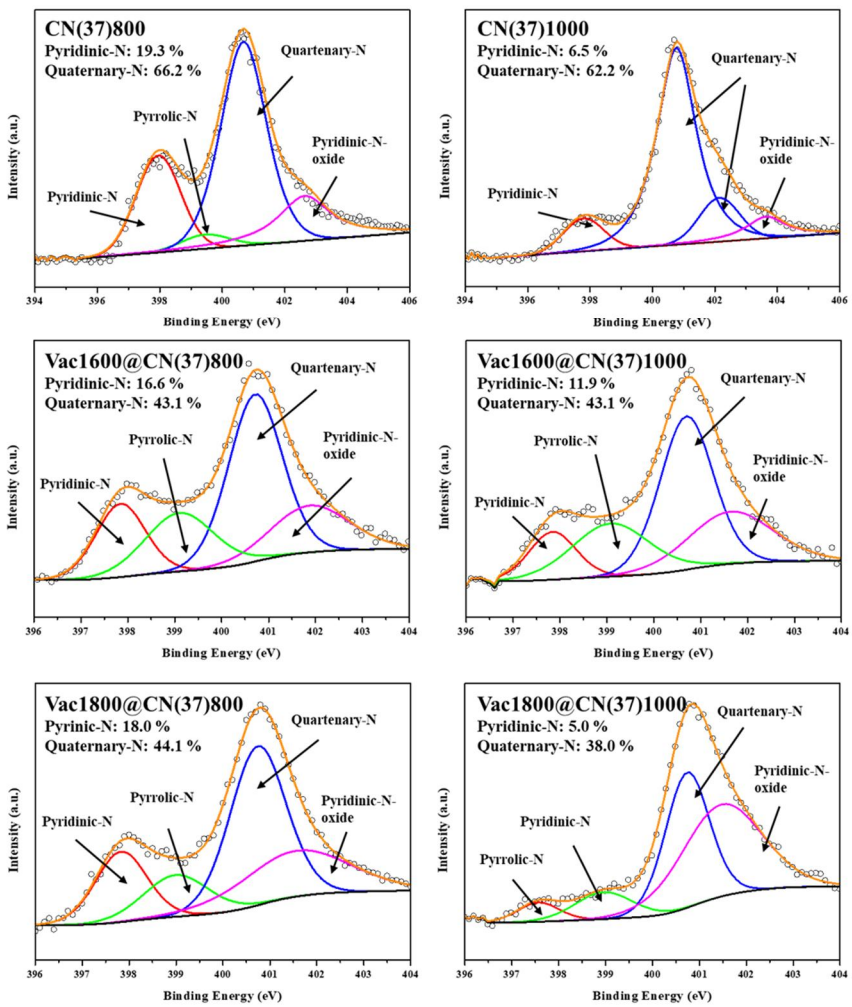

Figure 29. High resolution XPS N 1s core level spectra for CN(37)s, Vac1600@CN(37), and Vac1800@CN(37)s synthesized at 800 and 1000 ℃.

3.2.4. EDLC application

Electrochemical measurements were proceeded to investigate the capacitive behaviour of the prepared carbon materials with various fabricating conditions. Figure 30 shows the cyclic voltammetry (CV) graphs at scan rate from 1 mV/s to 20 mV/s. As can easily be noticed, the inner areas of CV profiles of the samples chlorinated at 800 ℃ are at least as twice larger than that of the samples chlorinated at 1000 ℃, which directly represents the large difference in charge storability. This difference between TiC-CDC800 and TiC-CDC1000 is also remarkable, which means that the difference in nitrogen content cannot be the main factor for such large differences in capacitive performance of samples depending on the chlorination temperature. Pores smaller than 1 nm highly enhances the capacitance of the material due to the reduced surface area for double-layer charge storage with smaller solvation radius. [12, 88] During graphitization processes at higher temperature (1000 ℃ in this study), the rearrangement of disordered carbon atoms into more ordered ones can decrease the populations of small pores (< 1 nm), as shown in XRD analyses (Figure 23) and Raman analyses (Figure 24) and pore size distributions (Figure 25); such narrow pores were always diminished for the samples chlorinated at 1000 ℃ (Figure 25). Therefore, it can be concluded that the exacerbated capacitive behaviour for the carbons chlorinated at 1000 ℃ is due to the degeneration of pores smaller than 1 nm during graphitization processes. Based on these observations, the electrochemical properties of carbons chlorinated at 1000 ℃ was not further investigated.

The CV graphs of CN(37)800, Vac1600@CN(37)800 and Vac1800@CN(37)800 show well-maintained the box-shaped profile up to 20 mV/s

as shown in Figure 30, but that of TiC-CDC800 starts to slightly distort from 10 mV/s, being originated from the resistive behaviour. Such difference becomes more definite for the CV profiles at higher scan rates over 30 mV/s. No more box-shaped profiles are observed for TiC-CDC800 at the scan rates of above 50 mV/s, and a certain extent of such distortions is also observed for other samples at high scan rates. Galvanostatic charge/discharge results showed similar tendency as CV profiles. As shown in Figure 31, significant IR drop of TiC-CDC800 indicates its high resistive behaviour compared to other samples. At the current density of 2 $A g^{-1}$, IR drop value of TiC-CDC800 ($\Delta V = 0.13$ V) is much higher than other samples, CN(37)800 ($\Delta V = 0.05$ V), Vac1600@CN(37)800 ($\Delta V = 0.07$ V) and Vac1800@CN(37)800 ($\Delta V = 0.07$ V).

Volumetric capacitance as well as gravimetric capacitance is an important parameter to evaluate the electrochemical performance of the material particularly for applying to micros-scale electric devices. To quantify electrochemical performances of the samples chlorinated at 800 ℃, gravimetric and volumetric capacitance of the samples were calculated based on the charge/discharge profiles using equation (3) and plotted in Figure 32(a – b), respectively. According to the results in Figure 32(a), the highest gravimetric capacitance at current density of 0.1 A/g was achieved by Vac1600@CN(37)800 (174.0 F/g), followed by Vac1800@CN(37)800 (168.0 F/g), TiC-CDC 800 (148.0 F/g) and CN(37) 800 (135.0 F/g). The abundance of nitrogen in Vac1600@CN(37)800 and Vac1800@CN(37)800 seems to induce the surfaces more electrochemically active and enable to achieve higher capacitance than conventional TiC-CDC800. In addition, core-shell structure of Vac1800@CN(37)800 seems to enhance the ion transport inside the pore to maximize the charge storage. On the other hand,

CN(37)800 showed the lowest performances among these four samples at low current density even though it possesses the highest nitrogen content among the samples. This is because most of the pores in CN(37)800 are in the range between meso- to macropores in size, which are not advantageous in surface charge storage. However, because ion diffusion inside CN(37)800 was facilitated by larger pore size and hollow core structure, the rate-dependent charge storability of CN(37)800 is higher than any other samples, and it shows the improvement of electric conductivity due to the highest nitrogen content. At the current density of 10 A/g, the capacitance of CN(37)800 was measured as 42.0 F/g, maintained 31.1 % of capacitance at 0.1 A/g (6.3 % for TiC-CDC, 17.4 % for Vac1600@CN(37)800 and 21.0 % for Vac1800@CN(37)800). For the comparison, capacitance values for the samples chlorinated at 1000 ℃ were plotted in Figure 33. In addition, capacitance values calculated using equation (2) based on the CV profiles for the whole samples were shown in Figure 34. The gravimetric/volumetric capacitances were in similar values.

In the case of volumetric capacitances of prepared carbon chlorinated at 800 ℃ in Figure 32(b), interestingly, Vac1800@CN(37)800 showed exceptionally high capacitance value than other three materials (240.0 F/cm^3 at 0.1 A/g). Also, the capacitance of Vac1600@CN(37)800 and CN937)800 markedly declined only by converting to volumetric measurements. A decrease in volumetric capacitance was already observed in section 3.1.7. Also, according to TEM images (Figure 26) and pore size distribution plots (Figure 25), carbon-rich domain of Vac1800@CN(37)800 is composed of dense and narrow micropore structures, whereas nitrogen-rich domain of Vac1600@CN(37)800 and CN(37)800 consists of hollow empty structure that lowers density. Therefore, although

Vac1800@CN(37)800 has smaller total pore volume than Vac1600@CN937)800 and CN(37)800, its densely packed narrow micropores lead high volumetric charge storing capacity. To investigate the electrochemical robustness of fabricated samples for long-term charging/discharging periods, Vac1600@CN(37)800 and Vac1800@CN(37)800 were charged and discharged for 100,000 cycles, as depicted in Figure 32(e). These two carbon materials showed no fades in performance up to the tested periods. This result shows that our method for preparing carbon materials for supercapacitor applications involved no impurities that could exacerbate the charge-storing electrochemical processes.

The rate-dependent performances of the samples are well-correlated with EIS analysis results, as shown in Nyquist plots in Figure 32(c). The electrical conductivity of the active material is usually included with circuit resistance (R_s), which can be derived from x-axis intersection at high frequency ranges. All samples from Ti($C_{0.3}$,$N_{0.7}$) starting material have similar R_s values (0.49 Ω, 0.67 Ω, 0.58 Ω for Vac1600@CN(37)800, Vac1800@CN(37)800 and CN(37)800, respectively, while TiC-CDC800 shows relatively high R_s value (1.01 Ω). In addition, as smaller semicircle indicates the lower charge transfer resistance (R_{ct}) between electrode and electrolyte, CN(37)800 is advantageous at higher scan rates or current densities by improved electrochemical charge storage kinetics while TiC-CDC800, with larger semicircle shows the worst rate performance: 1.539 Ω, 1.09 Ω, 0.728 Ω and 1.671 Ω for Vac1600@CN(37)800, Vac1800@CN(37)800, CN(37)800 and TiC-CDC800, respectively. These reduced values of electrochemical impedance elements in CN(37) samples can be explained by the effect of nitrogen content. Because R_s involves not only external circuit resistance but also electric conductivity inside the electrode, the lower R_s values in CN(37)

samples are due to the improved electric conductivity of active material. Also, surface activation by nitrogen doping facilitates the charge transfer between electrode and electrolyte, which results in the decrease in R_{ct} values in CN(37) samples. In addition, because CN(37)800 possesses the highest nitrogen content among the samples, it shows the lowest R_{ct} value. On the other hand, R_{ct} of Vac1600@CN(37)800 is relative high because electrochemically active domain of Vac1600@CN(37)800 is nitrogen-lean core.

To observe the frequency-dependent behaviours on the real and imaginary part of the capacitance of the samples, Bode plot of impedance phase angle vs. frequency is prepared in Figure 32(d). TiC-CDC800 shows frequency response profile similar to conventional carbonaceous materials, that capacitive behaviour is dominant at low frequency range and resistive behaviour at high frequency range. [89] Such behaviour means that most of the charge storage of TiC-CDC800 comes from electrochemical double-layer capacitors (EDLC). However, in case of CN(37) samples, additional capacitive behaviours are observed at high frequency range, which is originated from pseudocapacitive charge storage. [89] Vac1600@CN(37)800 shows the lowest phase angle among the CN(37) samples at high frequency ranges. In addition, in case of CN(37)800 and Vac1800@CN(37)800, the peak frequency is shifted to higher frequency than Vac1600@CN(37)800, which represents the reduced diffusive resistance.

The volumetric capacitance of the carbon-based materials was summarized by Wang et al. [20] As can be seen in Figure 35, the graphene and ACs show capacitance superior to carbide-derived carbons (CDCs), template carbons (TCs) and carbon nanotubes (CNTs). The present nitrogen-doped carbon materials chlorinated from pre-vacuum-annealed $Ti(C_{0.3},N_{0.7})$ at 1800 ℃ show much higher

volumetric capacitance value than CDCs reported in the literature, and it is even comparable to graphene materials. This demonstrate that the process proposed in this study can provide a new route to produce a prospective candidate carbon-based material for the EDLCs materials.

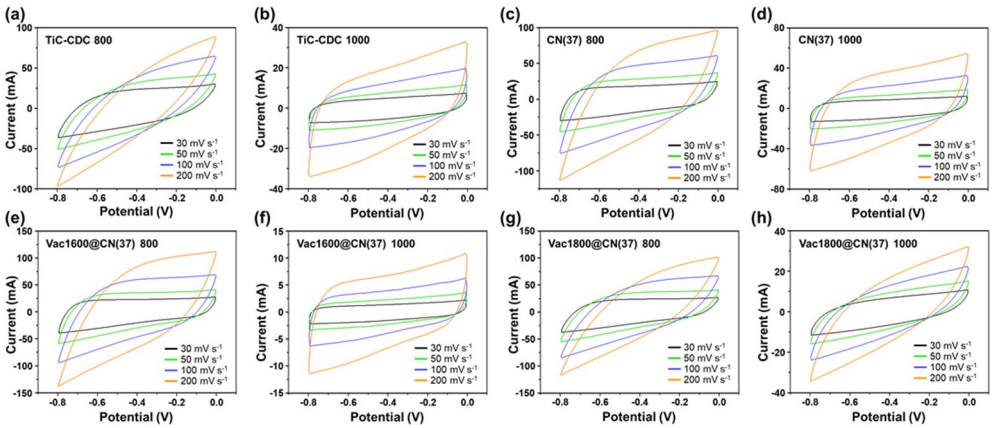

Figure 30. Cyclic voltammograms of (a) TiC-CDC800, (b) TiC-CDC1000, (c) CN(37)800, (d) CN(37)1000, (e) Vac1600@CN(37)800, (f) Vac600@CN(37)1000, (g) Vac1800@CN(37)800, and (h) Vac1800@CN(37)1000 at scan rate from 30 mV/s to 200 mV/s.

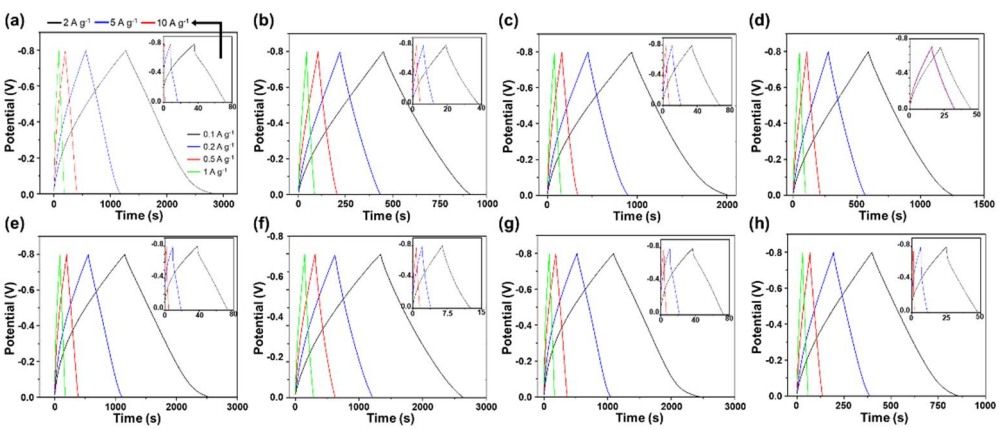

Figure 31. Galvanostatic charge/discharge profiles of (a) TiC-CDC800, (b) TiC-CDC1000, (c) CN(37)800, (d) CN(37)1000, (e) Vac1600@CN(37)800, (f) Vac1600@CN(37)1000, (g) Vac1800@CN(37)800 and (h) Vac1800@CN(37)1000. Each inset data provides obtained profiles at 2, 5 and 10 A/g.

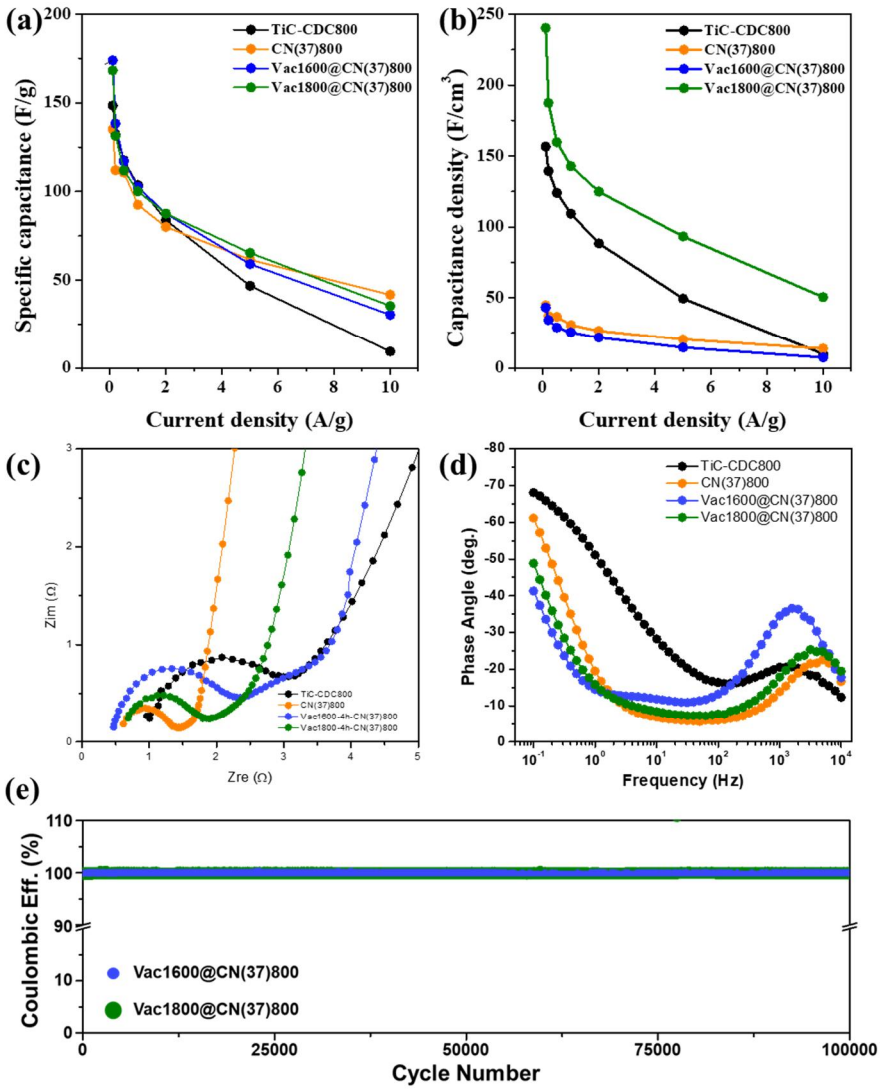

Figure 32. Calculated (a) gravimetric and (b) volumetric capacitance based on cyclic voltammogram at various current density. (c) Nyquist plots and (d) the impedance phase angle plot as a function of frequency of TiC-CDC800, CN(37)800, Vac1600@CN(37)800 and Vac1800@CN(37)800 at frequency range between 100 mHz to 10 kHz. (e) long term cyclic stability test results of Vac1600@CN(37)800 and Vac1800@CN937)800 at 5 A/g of charge/discharge current density for 100,000 cycles.

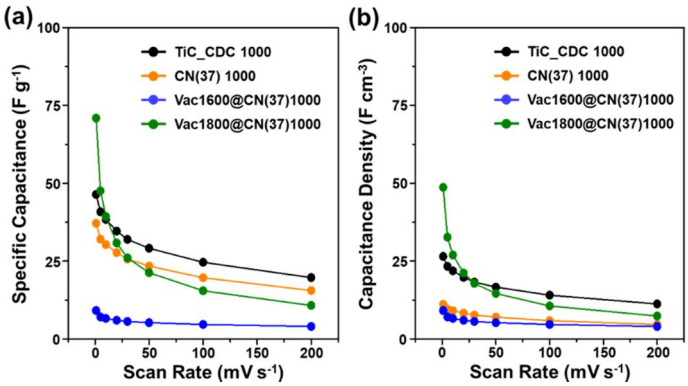

Figure 33. Calculated (a) gravimetric and (b) volumetric capacitances of TiC-CDC1000, CN(37)1000, Vac1600@CN(37)1000 and Vac1800@CN(37)1000 based on cyclic voltammogram at various scan rates.

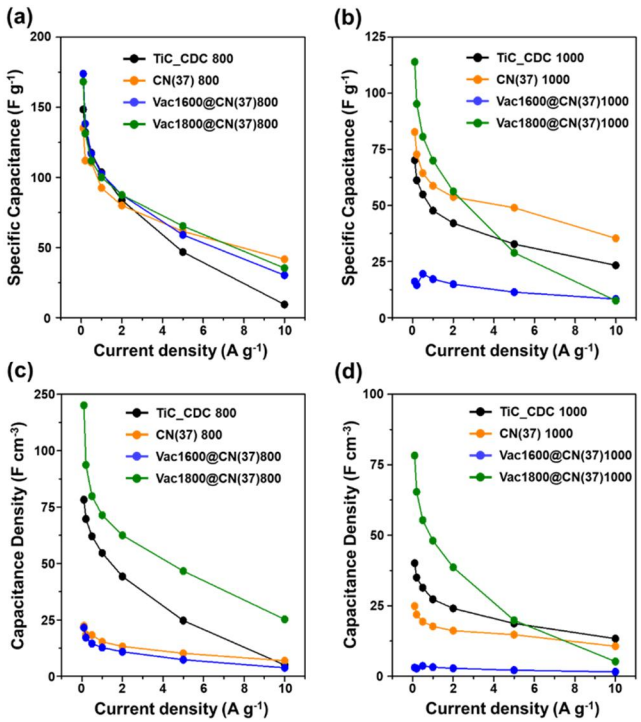

Figure 34. Calculated (a – b) gravimetric and (c – d) volumetric capacitances of (a and c) samples from 800 ℃ and (b and d) samples from 1000 ℃ based on Galvanostatic charge/discharge at various current densities.

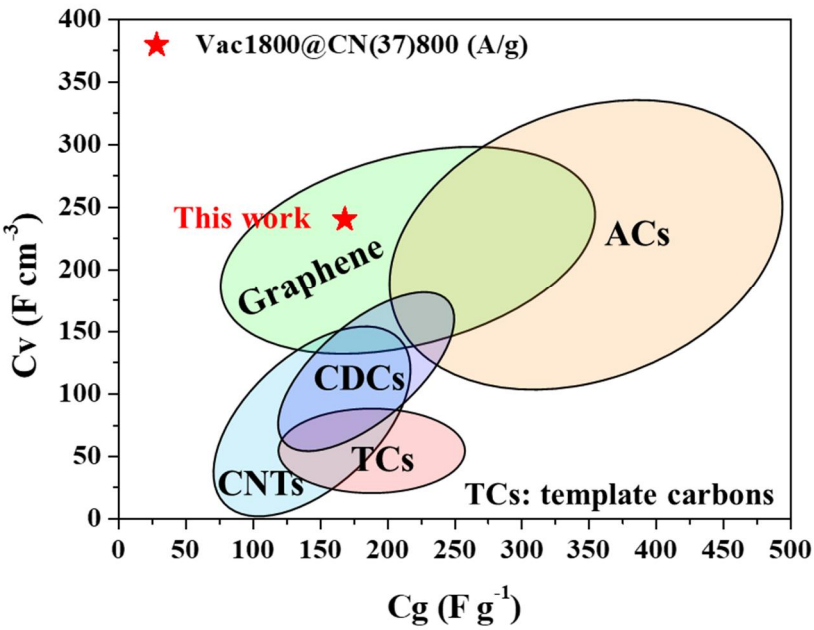

Figure 35. Comparison between gravimetric and volumetric capacitance for carbon materials. (Reproduced from reference [20])

3.2.5. Conclusions

Although CN(37)800 exhibited the highest nitrogen contents among all CNs, due to low BET SSA and low carbon density, its poor performance in EDLCs was inevitable. To solve this problem, the effect of high temperature vacuum-annealing treatment of $Ti(C_{0.3},N_{0.7})$ starting material at 1600 and 1800 ℃ prior to chlorination reaction were investigated. The structure and specific capacitance performance of carbon material synthesized by subsequent chlorination process at 800 ℃ is presented in comparison to the conventional TiC-CDC. All carbon materials produced by chlorination of $Ti(C_{0.3},N_{0.7})$ showed high nitrogen doping content and large BET SSA values regardless of vacuum-annealing treatment.

In particular, vacuum-annealing at 1800 ℃ developed hexagonal 'steps' sites in $Ti(C_{0.3},N_{0.7})$, which led the formation of core-shell structured carbon (microporous-rich core and graphitic shell) with relatively high nitrogen doping. These 'steps' sites induced by vacuum-annealing acted as nucleation sites for the active carbon in the subsequent chlorination process and grew into graphitic layers to form shells, and microporous-rich core. The nitrogen-doped carbon materials produced by chlorination of vacuum-annealed $Ti(C_{0.3},N_{0.7})$ at 1600 and 1800 ℃ both exhibited high gravimetric specific capacitance (174.0 F/g and 168.0 F/g, respectively) than non-vacuum-annealed samples. Particularly, a remarkable increase in volumetric capacitance was obtained from vacuum-annealed sample at 1800 ℃ (240.0 F/cm^3) due to densely packed core-shell structure. The capacity of nitrogen-doped carbon materials produced from vacuum-annealed $Ti(C_{0.3},N_{0.7})$ at 1600 and 1800 ℃ were also proved to be highly stable for 100,000 cycles.

This study presents a simple and effective processing route to produce

carbon materials having superb volumetric capacitance comparable to graphene. The newly synthesized carbon materials of hierarchical pore structure with high micropore volume and nitrogen functionality can be employed in various electrochemical applications.

3.3. Atomically dispersed Fe-doped CNB

3.3.1. Motivation

From the previous work by Kim et al., [32] demonstrated that the addition of boron can overcome the instability of C-N bonding and produce hollow CNB materials. However, as we have seen from section 3.1 and from Kim's work [32], the overall obtained mass was still low due to low carbon density in starting material, $Ti(C_{0.3},N_{0.7})$. Although the use of hollow CNB showed an improvement of ORR performance compared to CN material, [33] it was still inferior to Pt/C catalyst.

The single-atom catalysts (SACs) or atomically dispersed $M\text{-}N_x/C$ is now one of the most promising candidates for electrocatalysts, due to maximized accessibility of active sites and improved stability of metal atoms from acidic media as these metals are strongly bonded within the carbon matrix. SACs are typically produced from pyrolysis of metal-nitrogen-carbon organic precursors followed by HF solution treatment to remove any agglomerated and/or bulk metal particles, which restrict the large-scale production.

Since, co-doping through gas and/or diffusion process has been realized from our previous work, addition of extra metal element could also be made. After experimental work, we have successfully synthesized Fe-CNB material by chlorination reaction process. In this study, instead of using nitrogen-rich $Ti(C_{0.3},N_{0.7})$, instead, $Ti(C_{0.5},N_{0.5})$ was chosen as the C and N precursor due to higher carbon density with relatively comparable nitrogen doped contents when $Ti(C_{0.5},N_{0.5})$ was chlorinated. Moreover, from the previous work, the addition of

boron promoted the nitrogen stability and increased the occupancy of pyridinic-N functional group. Overall, atomically dispersed Fe-CNB were successfully synthesized and this material demonstrated a superior ORR performance than any other CNs, CNBs, or Fe-CNs, and even commercially available Pt/C.

3.3.2. Results and Discussion

$Ti(C_{0.5},N_{0.5})$ solid solution was used as carbon and nitrogen source, TiB_2 and $Fe(acac)_3$ were used as boron and iron sources, respectively. For detailed experimental procedure, see section 2.4. Previous study demonstrated that chlorination temperature is critical to the catalytic performance of N-doped porous carbon and N,B co-doped porous carbon. [33] Since the previous study was based on $Ti(C_{0.3},N_{0.7})$, first, we have conducted a series of experiments for the preparation of Fe-CNBs using $Ti(C_{0.5},N_{0.5})$, TiB_2, and $Fe(acac)_3$ at various chlorination temperature (600, 800, 1000 ℃, see section 2.4 for detailed experimental procedure). In addition, nitrogen-doped porous carbon (CNs) using $Ti(C_{0.5},N_{0.5})$, boron, nitrogen co-doped porous carbon (CNBs), and iron and nitrogen co-doped porous carbon (Fe-CNs) using $Ti(C_{0.5},N_{0.5})$ and $Fe(acac)_3$ were also prepared as control samples. The detailed experimental procedure can be found in section 2.1, 2.3, and 2.5, respectively. The obtained carbon catalysts were denoted as Fe-CNBT, Fe-CNT, CNBT, and CNT, where T = 600, 800, and 1000 ℃. The C/B ratio are kept 1:1, unless otherwise stated.

In the X-ray diffraction (XRD) patterns of Fe-CNB from all chlorination temperatures (600 to 1000 ℃) (Figure 36(a)), only two broad characteristic peaks around 26° and 44° were found, which could be assigned to (002) and (100)/(101) planes of turbostratic carbon, [82] and no clear crystalline phases related to Fe, and/or Fe_3C were observed. In addition, the (002) peak of Fe-CNB (26.07°) shifted to a smaller Bragg angle compared with pristine graphite (26.57°), indicating increased interlayer spacing compared with graphite. In the transmission electron microscopy (TEM) analysis in Figure 36(b), the resulting morphology of Fe-CNB800 were almost the same in shape and volume as their starting materials due

to conformal reaction. [18] The selected-area electron diffraction (SAED, inset of Figure 36(b)) pattern obtained from Fe-CNB800 show diffusive rings with 0.36 nm, 0.21 nm, and 0.12 nm d-spacing that corresponds to (002), (100)/(101) and (110)/(112), respectively. Due to similar morphology regardless of chlorination temperature (600, 800, and 1000 ℃), Fe-CNB800 will be discussed as a typical example throughout this study. As shown in High-Resolution TEM (HRTEM) image at the interior of the particle, Fe-CNB800 consisted ordered nanographites with an average d-spacing of 0.36 nm (Figure 36(c)). The enlarged TEM image at the surface of the Fe-CNB and its HRTEM image is presented in Figure 36(d). Growth of multi-walled carbon nanotubes (MWCNT) on the surface can be found with no sign of Fe related particles. MWCNTs are commonly synthesized by pyrolysis of acetylene over nanoparticles of iron, cobalt, and other metals dispersed over a solid substrate. [90] Such ordered nanographite layers on the surface and the growth of MWCNT could facilitate the effective electron transport necessary for efficient electrocatalysis. Further, Fe-CNB800 was investigated using high-angle annular dark-field scanning TEM (HAADF-STEM) as shown in Figure 36(e). The HAADF-STEM elemental mapping images, C, N, O, and Fe, demonstrate the uniformly distribution over the entire particles. It is important to note that, atomically dispersed Fe-CNB were achieved without any leaching process.

To explore whether atomic dispersion of Fe can be achieved without boron, Fe-CN samples were synthesized without boron source, TiB_2. The XRD patterns of Fe-CN in Figure 37(a) also do not show any Fe-related peaks, but only two broad characteristic peaks around 26° and 44° throughout all chlorination temperature. However, the TEM analysis in Figure 37(b) demonstrated formation of nanoparticles with diameter up to 50 nm. This formation of nanoparticles was not

observed from Fe-CNBs. Figure 37(c) also demonstrate that, these nanoparticles are surrounded by graphitic shells restricting from observation by XRD analysis. These graphitic shells are mostly due to catalytic effects of iron particles. [91] From HRTEM analysis, the average d-spacing was 0.249 nm, suggesting that these nanoparticles are Fe_3O_4. Furthermore, the HAADF-STEM elemental mapping images in Figure 37(e) confirms that these nanoparticles consist of iron confined within carbon shells, and no iron traces over the carbon surface was detected. These contrasting results suggest that boron may play a significant role in suppressing Fe particles from formation of large nanoparticles.

To further investigate the effect of boron, the amount of $Fe(acac)_3$ was varied from 0, 1, 5, 10, and 20 % for Fe-CN800 and Fe-CNB800, and analysed by Raman spectroscopy (Figure 38). Higher D-band intensity (~1330 cm^{-1}, see Figure 38(a)) was noticeable from Fe-CNB800 compared to Fe-CN800. In case of Fe0CNB800, as demonstrated in Figure 38(b), the I_D/I_G ratios for Fe-CNB800 almost maintain constant regardless of the amount of added Fe precursors from 1 – 20 %, whereas, gradual decrease in I_D/I_G ratios was observed for Fe-CN800. This indicates that the introduction of boron promotes disorderness in Fe-CNBs, but there may be a limited space for Fe atoms to co-exist within carbon lattices.

In recent investigation, Yuan et al. [92] has calculated thermodynamically the most stable state for Fe-BNC material. The position of the boron atom was varied around the $Fe-N_4$ square-planar structure. From this result, we have taken the most stable boron position, then calculated the bonding cohesive energy between solid atoms using Crystal Orbital Hamilton Population (COHP) method for boron and boron-free system. Figure 39 demonstrate the obtained result in Table and the corresponding model used for Fe-CN and Fe-CNB. The result show

that with addition of boron, the binding energy between Fe-N increased from -1.35 eV for boron-free Fe-CN to -1.39 eV for boron-containing Fe-CNB. This increased in bonding energy could be the reason for its stable bonding within four pyridinic-N, which promotes atomic dispersion rather than agglomeration into a larger particle. Moreover, because the most stable position for Fe is next to pyridinic-N functional groups, the addition of boron is expected to increase the pyridinic-N functional group which may also enhance the ORR catalytic performance.

The compositions and valence states of CN, CNB, Fe-CN, and Fe-CNB catalysts were obtained by X-ray photoelectron spectroscopy (XPS), Elemental Analysis (EA), and Induced Coupled Plasma-Atomic Emission Spectrum (ICP-AES). The wide scan XPS spectra confirmed that all samples consisted of Fe, C, N, and O (not shown). The high-resolution XPS in Figure 40 and Figure 41 also confirms the incorporation of B and Fe dopants in Fe-CN800 and Fe-CNB800. The Table 3 summarizes atomic surface concentrations of C, N, O, Ti, B and Fe. From the surface analysis, the nitrogen concentration was more or less similar for Fe-CN800 (XPS: 4.31 at.% and EA: 4.4 wt.%) and Fe-CNB800 (XPS: 3.15 at.% and EA: 4.3 wt.%). On the other hand, difference in the iron concentration from surface analysis and bulk analysis from XPS and EA were found, where 0.24 at.% and 2.0 wt.% for Fe-CN800, and, 0.08 at.% and 2.21 wt.% for Fe-CNB800, respectively. The difference in concentration at the surface is because in case of Fe-CN800, large size of Fe-particles are formed, whereas, Fe-CNB800 consists of uniformly dispersed over the particles as already observed in Figure 36(e) and Figure 37(e). The high-resolution XPS of N 1s spectra could be deconvoluted into four bonding peaks: 398.1 – 398.3 eV for pyridinic N, 399.4 eV for pyrrolic N and Fe-N_x species, 400.4 – 400.7 eV for graphitic N, and > 402 eV for oxidized-N species. The most

notable difference in the XPS spectra is the increase of pyridinic N intensity with addition of boron. The boron effect become significant when iron is co-doped, showing the most dominant peak as pyridinic N. In contrast, in boron-free catalyst, i.e. CN800 and Fe-CN800, graphitic-N is the most dominant peak. It was reported that [93] high content of pyridinic-N function enhance the ORR catalytic activity. Moreover, the increase in Fe-N_x moieties could promote the pyridinic-N due to their nature in bonding. [94] Therefore, the increase in pyridinic-N in Fe-CNB along with Fe-N_x moieties and boron are expected to show enhancement of ORR activity.

Figure 42 illustrate the N_2 adsorption-desorption isotherm of CN, CNB, Fe-CN and Fe-CNB. The result demonstrates that the addition of boron source into the system tend to increase the mesopores as indicated by increase in hysteresis at higher pressure regime. Nevertheless, the general shape is same. The summarized Brunauer-Emmett-Teller (BET) specific surface areas and pore volumes of the CN, CNB, Fe-CN, and Fe-CNB samples prepared at different temperatures are presented in Table 3. The results indicate that the highest BET SSA were achieved at 800 ℃ for all samples. On the other hand, with increase in amount of Fe in Fe-CN800 shows a decrease in BET SSA, whereas, Fe-CNB800 almost stayed constant. When Fe starting content was increased up to 10 %, the BET SSA started to show a decrease down to 1033 m^2/g and 754 m^2/g when 20 % of Fe was added. Nevertheless, BET SSA for Fe-CNBs were higher than Fe-CNs at all temperature and Fe contents.

To investigate the status of the iron coordination environment and the chemical state of the centre iron atoms in the dispersed in the Fe-CNB and Fe-CN catalyst, X-ray absorption near-edge structure (XANES) and Fourier transform

extended X-ray absorption fine structure (EXAFS) spectrometry are used. This technique is powerful and well established technique even if their concentration is very low (concentration of Fe in Fe-CNB ≈ 0.08 at.%, and Fe-CN ≈ 0.24 at.%). Figure 43(a) illustrate the XANES spectra at the Fe K-edge of the Fe-CNB800 and Fe-CN800, compared with Fe-foil as reference. The absorption edge of the XANES for Fe-CNB featured a weak pre-edge peak at around 7114.2 eV. This peak is the fingerprint of Fe-N_4 square-planar structure. [92] By contrast, the Fe K-edge XANES spectrum of the Fe-CN800 catalyst do not have such sharp peak at around 7114 eV, but rather broad spectra is observed. This is more similar to those of Fe_3C peak. [92] Figure 43(b – c) shows the K^3-weighted FT-EXAFS spectra of Fe-CN and Fe-CNB, respectively. The most dominant peak for Fe-CNB800 (Figure 43(c)) was from the characteristic of N-coordinated iron. The main signal of Fe-CNB at 1.5 Å which could be assigned to the Fe-N bonding distance, stemming from a nitrogen shell surrounding iron atoms which was reported for iron phthalocyanine (FePc), [92] confirming the existence of Fe-N_4. On the other hand, Fe-CN shows peak shift in higher distance compared to Fe-CNB. There exist two main peaks, where first peak near 1.75 Å and the later one at 2.2 Å. The peak at 1.75 Å is close to the Fe-O bond coordination. The latter peak at 2.2 Å is similar to Fe foil, where Fe-Fe coordination is. The result show that, when boron is added into the system, Fe agglomeration and bonding with oxygen is minimized and form Fe-N_4. However, in boron-free system, the addition Fe precursor rather reacts with oxygen to form iron oxide, most likely Fe_3O_4 (analysis from TEM in Figure 37(d)) and hence, Fe-Fe bonding distance is distinctively observed. Hence, it can be suggested that Fe-CNB catalyst is the dominant ORR active catalysts.

On the basis of results, atomically dispersed Fe, N and B co-doped porous

carbon materials, the Fe-CNB materials were directly evaluated by depositing on a glassy carbon electrode and used as working electrode in a typical three-electrode setup with a rotating ring disk electrode (RRDE) in O_2 saturated 0.1 M KOH electrolyte. The polarization curve of CN, CNB, Fe-CN and the commercially available Pt/C catalyst is also displayed. As shown in Figure 44(a), the onset for Fe-CN800 is similar regardless of the iron starting amount. The only difference was that increase in current density was observed with increased amount of Fe precursor. The onset for Fe-CN800 were ≈ 0.90 V vs RHE. On the other hand, the onset for Fe-CNB slightly varied depending on the amount added iron precursors, whereas, the current density was similar (see Figure 44(b)). The highest onset (0.92 V vs RHE) was achieved when 10 % of $Fe(acac)_3$ was added, which has more positive ORR onset potential than Fe-CN800. When comparing with CN, CNB, Fe-CN, Fe-CNB, and Pt/C, Fe-CNB exhibited the highest ORR onset potential and this value is higher than Pt/C. This can be directly visualized in Figure 44(c). Moreover, when half-wave potential of Fe-CNB, Fe-CN and Pt/C are compared, Fe-CN and Pt/C both show 0.81 V, whereas, 0.85 V for Fe-CNB, demonstrating superior performance of Fe-CNB and suggesting efficient electron process of Fe-CNB material.

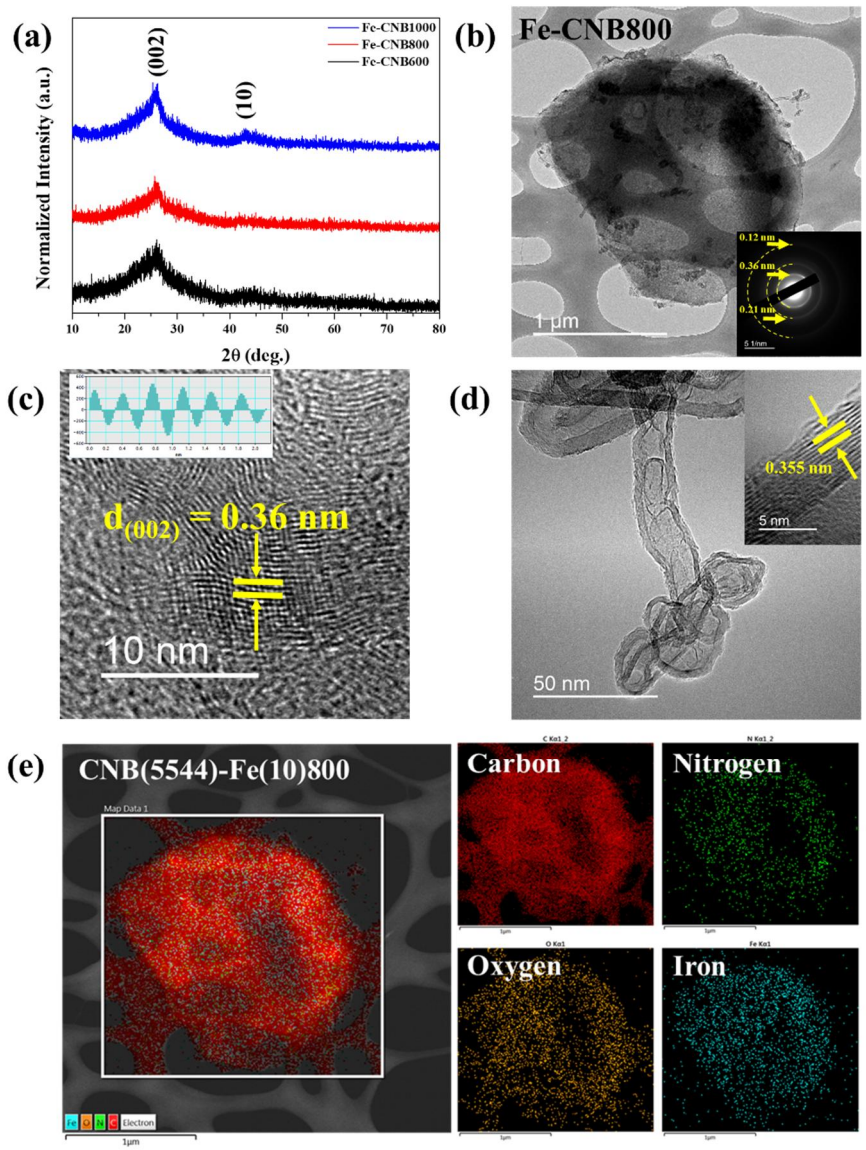

Figure 36. (a) XRD patterns of Fe-CNBs, (b) TEM image of Fe-CNB800. Inset: corresponding SAED pattern. (c) High-resolution TEM image of the Fe-CNB at the interior. Inset: contrast profile on the arrow indicates interlayer spacing. (d) Enlarged TEM image at the surface of the Fe-CNB particle. Inset: corresponding HR-TEM image. (e) HAADF-STEM image and corresponding EDS spectroscopy elemental mapping images of C, N, O, and Fe.

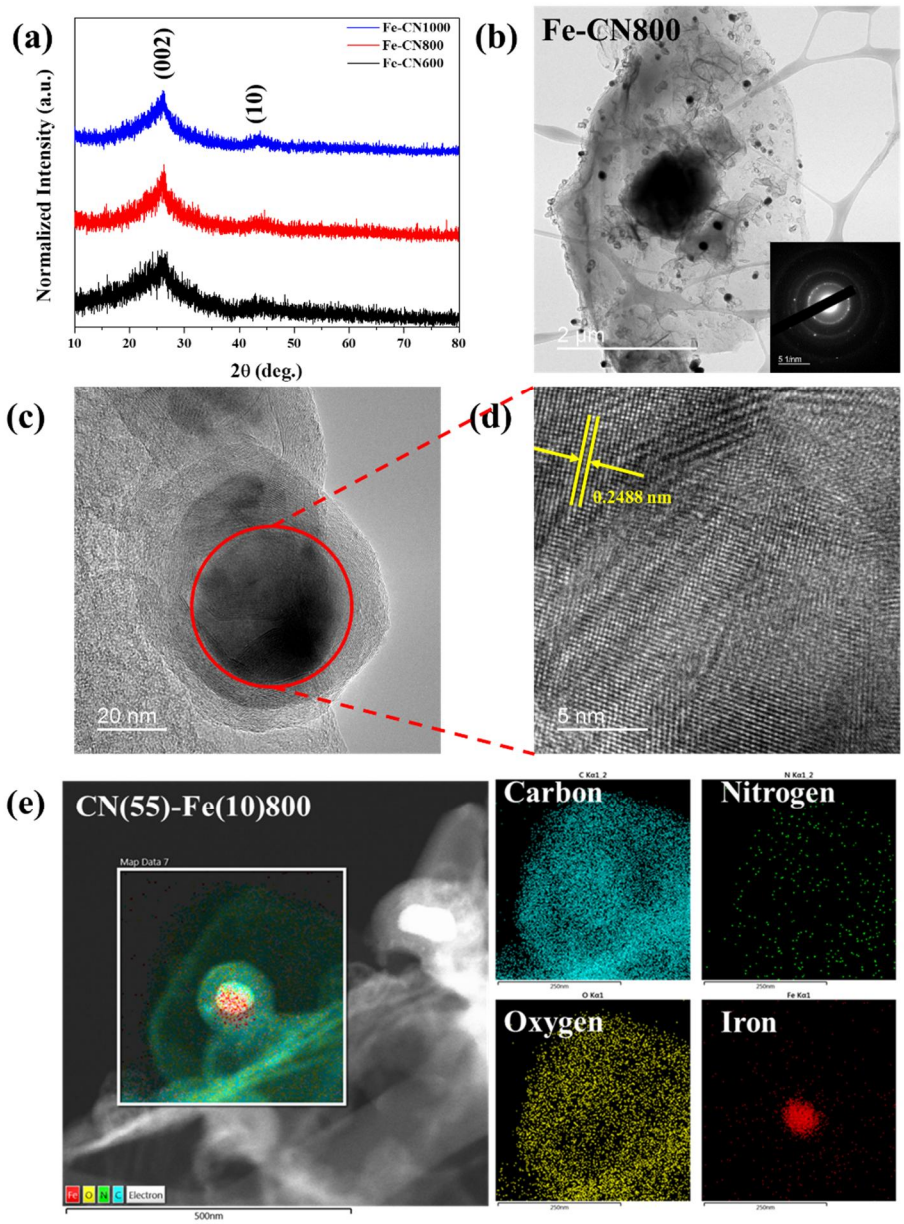

Figure 37. (a) XRD patterns of Fe-CNs, (b) TEM image of Fe-CN800. Inset: corresponding SAED pattern. (c) Enlarged TEM image of iron oxide particle and (d) High-resolution TEM image of the iron oxide. (e) HAADF-STEM image and corresponding EDS spectroscopy elemental mapping images of C, N, O, and Fe.

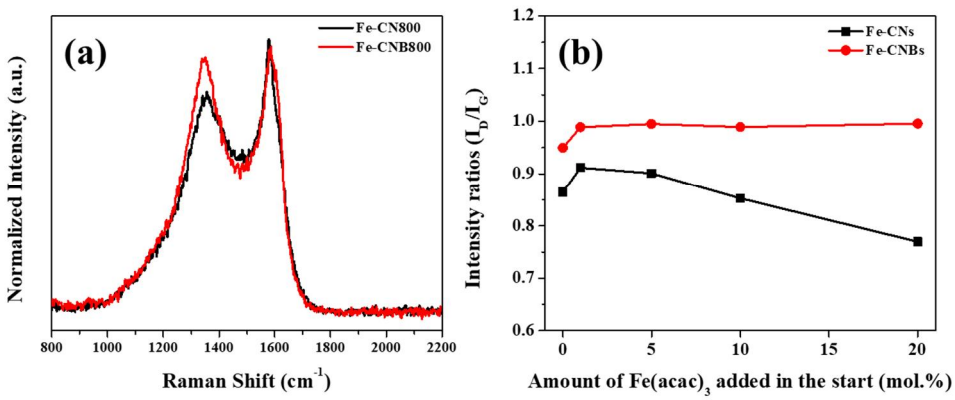

Figure 38. (a) Raman spectra of Fe-CN800 and Fe-CNB800 samples with 10 % of Fe. (b) I_D/I_G ratio of Fe-CN800 and Fe-CNB800 with amount of Fe precursor varying from 1, 5, 10, and 20 %.

(eV)	Fe	N	C
Fe		-1.3523	
N	-1.3523		-6.4027
C		-6.4027	

(eV)	Fe	N	B	C
Fe		-1.3874		
N	-1.3874		-5.2745	-6.6073
B		-5.2745		
C		-6.6073		

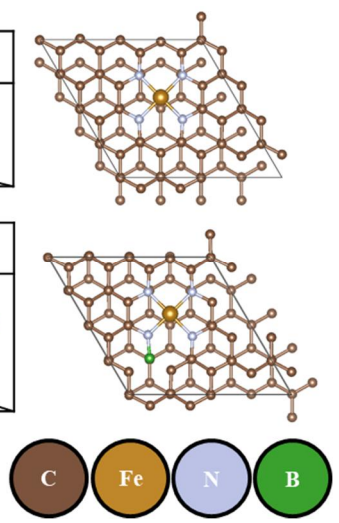

Figure 39. Binding energy of each elements calculated from COHP method. The right images show the corresponding atomic positions for this calculation.

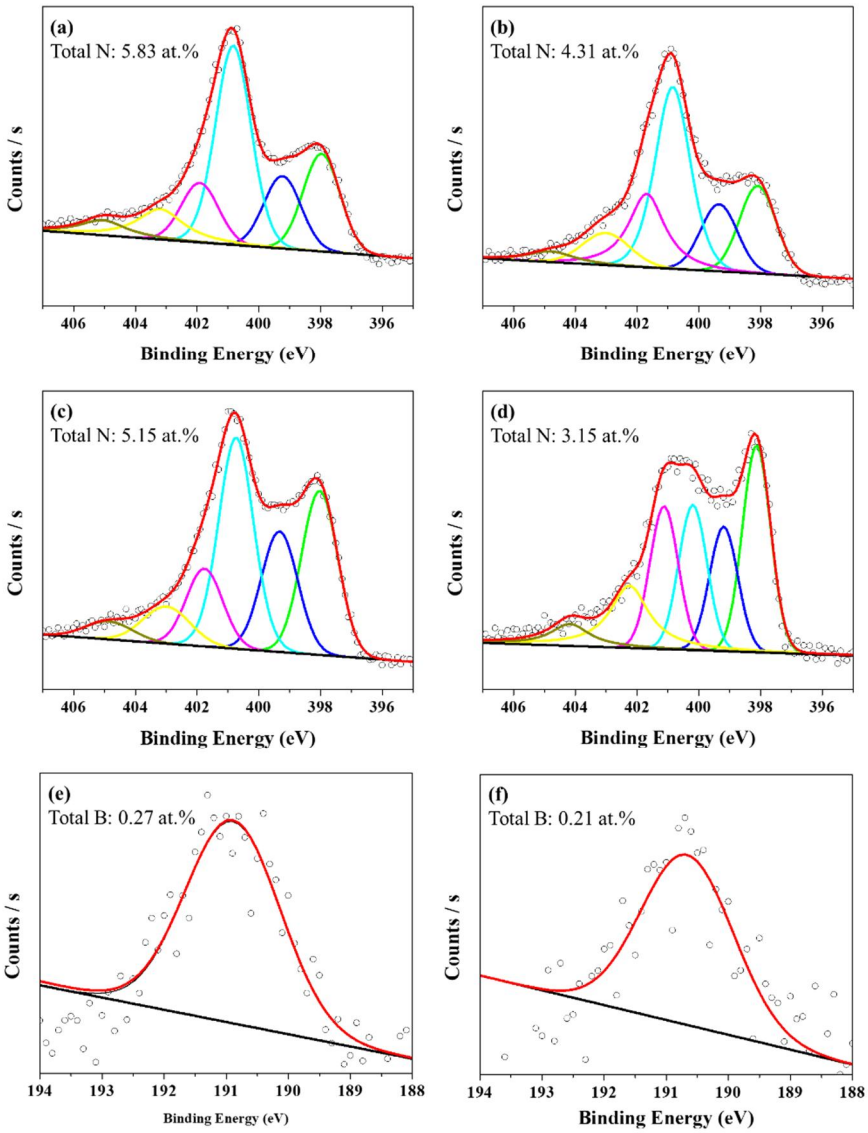

Figure 40. High-resolution XPS N 1s spectra of (a) CN800, (b) Fe-CN800, (c) CNB800, (d) Fe-CNB800; High-resolution XPS B 1s spectra of (e) CNB800 and (f) Fe-CNB800.

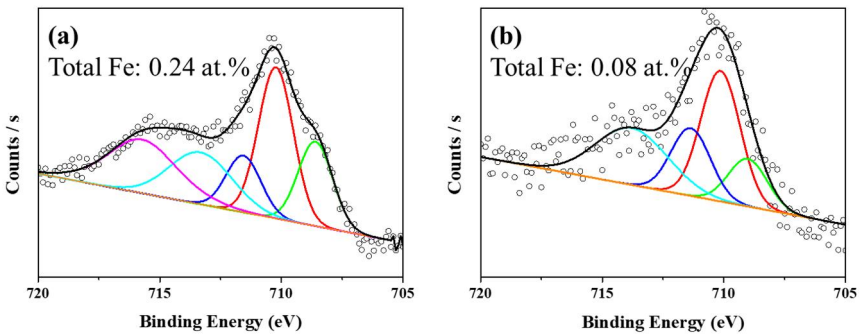

Figure 41. High-resolution XPS Fe 2p spectra of (a) Fe-CN800 and (b) Fe-CNB800.

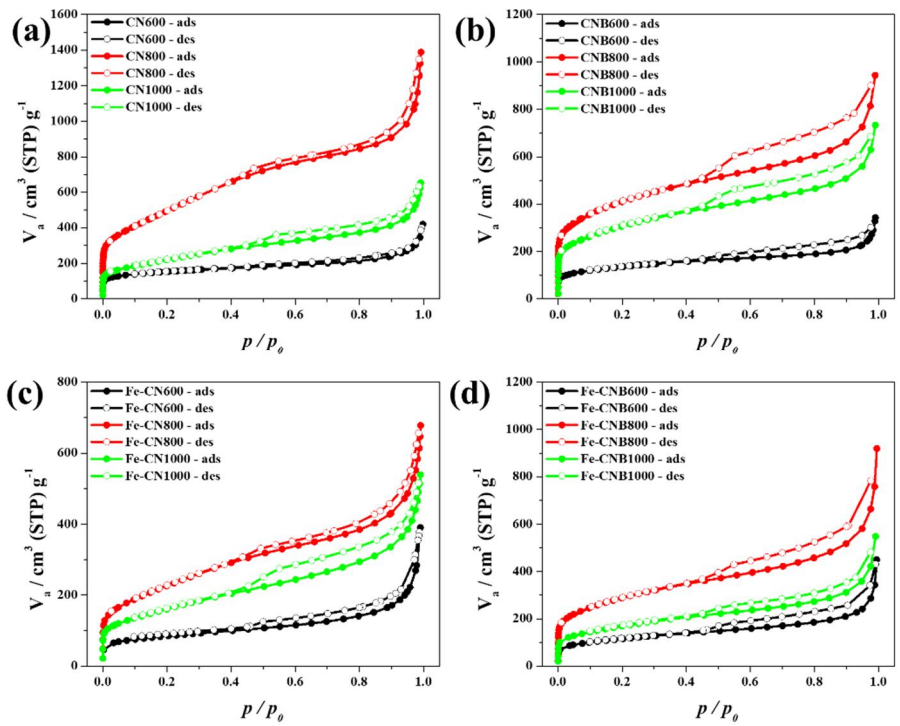

Figure 42. N_2 adsorption-desorption isotherm of (a) CN, (b) CNB, (c) Fe-CN and (d) Fe-CNB synthesized at 600, 800 and 1000 ℃.

Table 3. Summarized textural properties and composition concentrations

Characterization	BET				XPS (at.%). EA and ICP in bracket (wt.%)					
Samples	**Specific Surface Area (m^2/g)**	**Total Pore Volume (cm^3/g)**	**Micropore Volume (cm^3/g)**	**Mesopore Volume (cm^3/g)**	**C**	**N**	**O**	**Ti**	**B**	**Fe**
CN600	537.98	0.5459	0.2161	0.1576	86.94	8.69	3.25	N/D	N/A	N/A
CN800-5h	1835.6	2.0553	0.634	0.7724	91.3 (72.5)	5.83 (7.1)	1.77 (5.2)	N/D	N/A	N/A
CN1000	800.87	0.9798	0.2857	0.357	92.75	4.17	1.96	0.12	N/A	N/A
CNB600	476.85	0.5161	0.1853	0.1338	75.54	11.38	6.41	0.03	5.58 (1.80)	N/A
CNB(11)800	1469.4	1.457	0.5527	0.472	90.94 (74.2)	5.15 (6.1)	2.67 (6.6)	0.06	0.27 (0.11)	N/A
CNB1000	1099.7	1.1276	0.4079	0.3807	91.22	2.54	5.11	N/D	0.45 (0.17)	N/A
Fe-CN600	295.91	0.5944	0.1167	0.147	86.24	5.9	3.53	0.28	N/A	0.33 (4.49)
Fe(1)-CN800	1535.8	1.6514	0.5284	0.6268	88.02	4.46	5.59	0.26	N/A	0.06 (0.94)
Fe(5)-CN800	1081.3	1.1719	0.3778	0.5044	85.58	4.42	6.73	0.29	N/A	0.09 (1.32)
Fe(10)-CN800	824.48	1.0179	0.2919	0.3755	89.9 (76.2)	4.31 (4.4)	2.37 (6.0)	0.16	N/A	0.24 (2.00)
Fe(20)-CN800	716.24	0.9593	0.2542	0.3336	92.91	2.27	3.33	0.05	N/A	0.82 (1.68)
Fe-CN1000	582.85	0.8249	0.2093	0.3124	93.34	2.8	2.12	0.14	N/A	0.07 (0.83)
Fe-CNB600	410.66	0.565	0.1559	0.1704	83.57	6.81	4.83	N/D	2.56 (0.65)	0.21 (3.28)
Fe(1)-CNB800	1291	1.4397	0.4824	0.4447	88.27	4.96	5.14	N/D	0.51 (0.13)	0.07 (2.45)
Fe(5)-CNB800	1202.8	1.3186	0.4506	0.438	90.39	3.85	4.66	N/D	0.51 (0.13)	0.03 (2.13)
Fe(10)-CNB800	1033.1	1.2448	0.3823	0.4186	93.65 (79.6)	3.15 (4.3)	1.8 (7.5)	N/D	0.21 (0.23)	0.08 (2.21)
Fe(20)-CNB800	754.18	1.1542	0.2846	0.3569	94.18	2.04	2.52	N/D	0.16 (0.34)	0.02 (1.55)
Fe(10)-CNB(41)800	1037.4	1.2831	0.3822	0.4014	92.09	3.14	3.15	N/D	0.26 (0.14)	0.14 (2.47)
Fe(10)-CNB(48)800	1079	1.3148	0.4046	0.4302	90.7	3.78	3.36	N/D	1.04 (0.24)	0.03 (2.20)
Fe-CNB1000	602.55	0.833	0.2229	0.2606	95.57	1.39	1.59	N/D	0.39 (0.47)	0.05 (0.70)

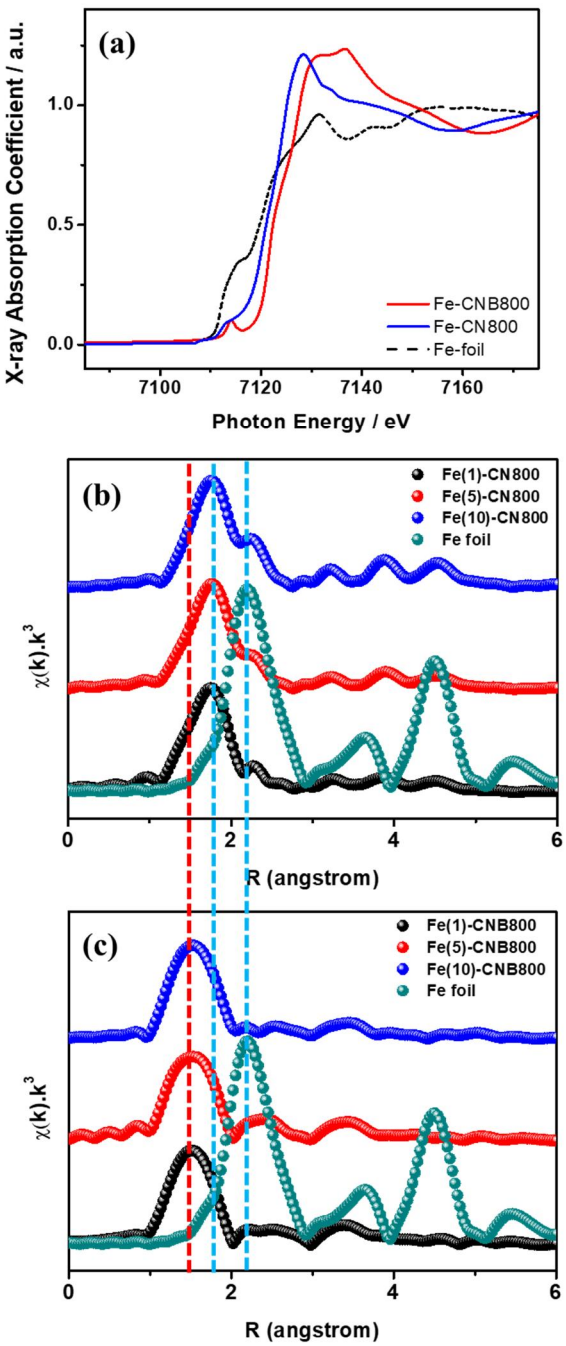

Figure 43. Fe K-edge (a) XANES and (b) k^3-weighted FT-EXAFS spectra of Fe-CN and Fe foil, and, (c) Fe-CNB and Fe foil with variable Fe starting content.

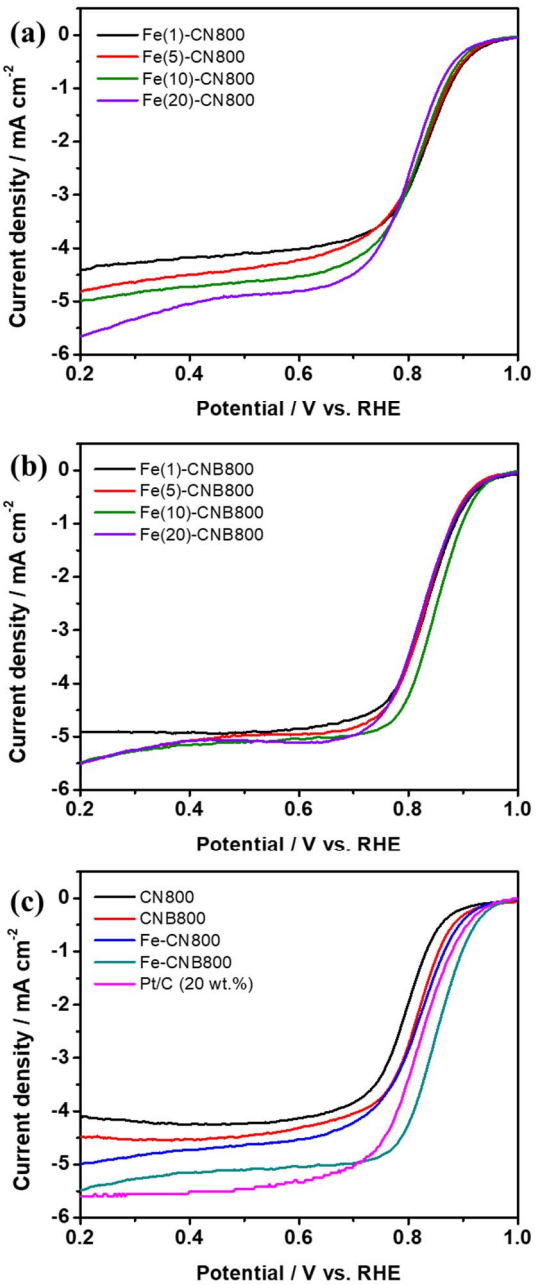

Figure 44. (a) LSV curve of Fe-CN800, (b) Fe-CNB800 with different amount of starting Fe precursors at 1600 rpm. (c) LSV curves of CN, CNB, Fe-CN, Fe-CNB, and Pt/C at 1600 rpm.

3.3.3. Conclusions

In this study, atomically dispersed Fe-CNB has been successively synthesized by addition of boron and iron source and chlorinated at elevated temperature. Just like in CDC process, this provided large surface area of 1200 m^2/g with hierarchical pore structure from micro to mesoporous carbon. Although it is still not clear the reason for the atomic dispersion of Fe-N, but according to COHP calculation, the addition of boron promotes the binding energy between iron and nitrogen, promoting thermodynamically stable states. The atomic dispersion of Fe-N was further confirmed by using XANES and EXAFS analysis. On the other hand, when Fe-CN was synthesized without the addition of boron, the Fe agglomerate each other to form a larger particle with size up to 50 nm, showing a critical role of boron. Moreover, when boron and iron are co-doped in CN, increase in pyridinic-N functional group was observed. In addition, the process does not involve with any leaching making more desirable for large-production.

The increased in pyridinic-N with atomically dispersed Fe-N carbon materials was further evaluated as a potential ORR electrocatalysts. In comparison to CN, CNB, Fe-CN, and Pt/C, the obtained Fe-CNB material show superior ORR performance with more positive onset-potential and half-wave potential than commercially available Pt/C. This study provided a facile and cost-effective process to synthesize atomically dispersed Fe-CNB material using a single-step chlorination reaction, and the additional works for further improvement and the development of variable applications, based on atomically dispersed Fe-CNB, are now in progress and will be discussed in our future publication.

3.4. Appendix

3.4.1. Highly developed (002) planes from CN(73)

In Figure 8b, a sharp straight peak at ~26° and broad XRD patterns co-exist together for CN(73), even at low chlorination temperature. Norimatsu et al. [85] demonstrated the formation process of graphene layers on SiC (0001) initially begin with sublimation of Si atoms and aggregation of remaining carbon atoms which forms curved graphene layers on the 'step' and the 'terraces' of the SiC substrate. The SEM image of as-received TiC, $Ti(C_{1-x},N_x)$ raw powders illustrated in Figure S 1. The shape of carbonitride particles is more rounded with increasing nitrogen content. Most 'step'-like morphology can be found in $Ti(C_{0.7},N_{0.3})$ (pointed by white arrows in Figure S 1(b)). Since CDC is a conformal reaction, the 'step'-like morphology is retained as found in Figure S 1(e). During chlorination reaction, the active carbons could nucleate at these 'step' sites and form graphene layers. With the progress of chlorination process, these graphene layers can continue to cover the surface and grow into graphitic layers, which result in sharp (002) peak in XRD analysis (see Figure 8(f)). The results of the Raman spectra in Figure 9 can be also explained consistently.

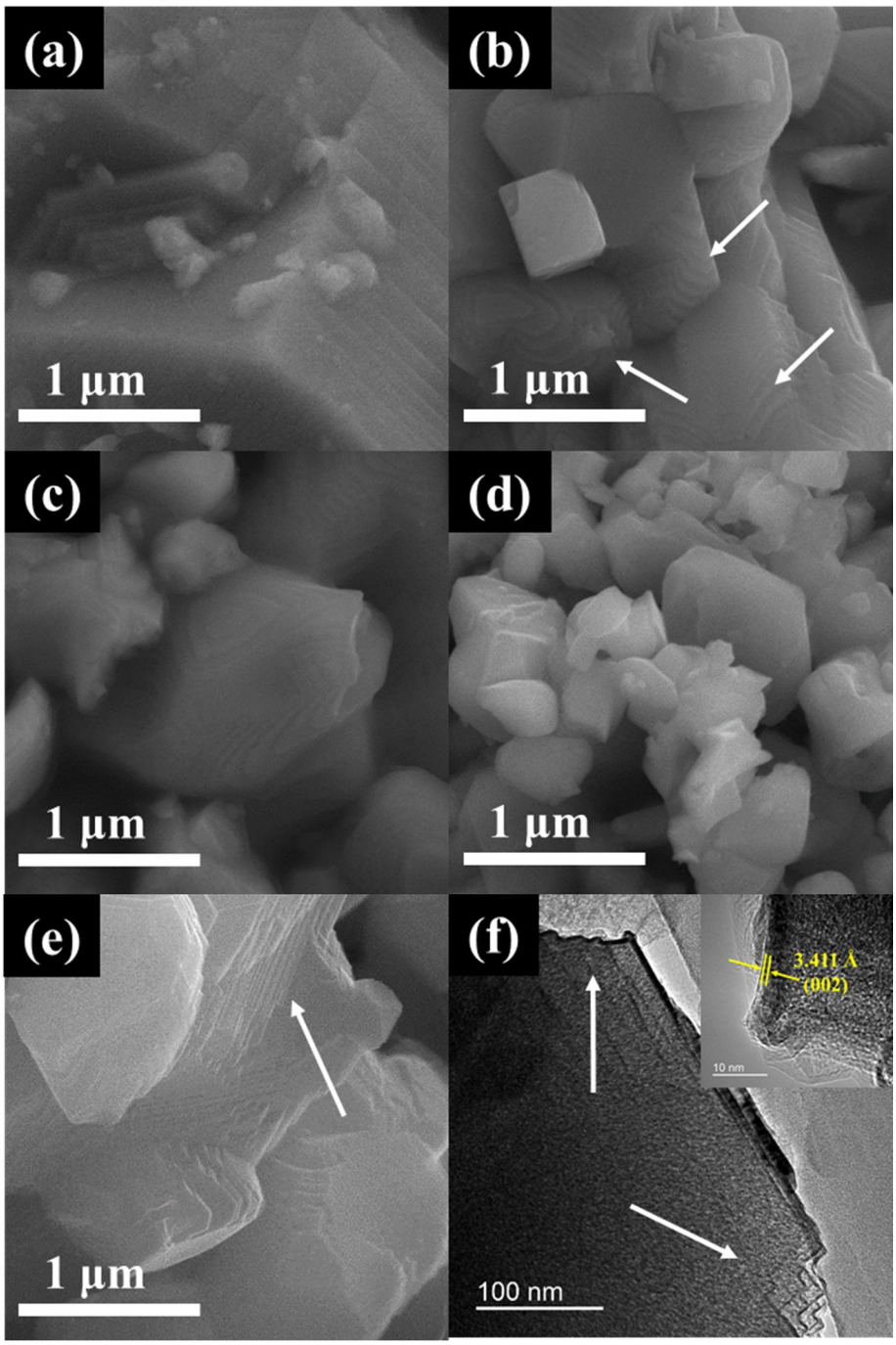

Figure S 1. SEM images of as-received powder of (a) TiC, (b), $Ti(C_{0.7},N_{0.3})$, (c) $Ti(C_{0.5},N_{0.5})$, and (d) $Ti(C_{0.3},N_{0.7})$. (e – f) show the SEM and TEM images of CN(73)800.

4. Overall Conclusion

In this thesis, the novel synthesis methods for heteroatoms doped porous carbon-based material with hierarchical pore structure has been demonstrated by using chlorination reaction method. This approach provides a new method for doping heteroatoms such as nitrogen and boron, but also demonstrate how atomically dispersed Fe-N_4/C could be synthesized.

Nitrogen-doped porous carbon by chlorination of $Ti(C_{1-x},N_x)$ was revisited in this study. The doping mechanism, as well as the formation of pore, and lastly, the formation of hollow carbon using $Ti(C_{0.3},N_{0.7})$ are explored both experimentally and theoretically. Although chlorination of TiN readily produce $TiCl_4$ and N_2 gases, the difference in thermodynamic stability between $TiC_{s.s}$ and $TiN_{s.s}$ in Cl_2 allows a sequential reaction to proceed. This sequential reaction promoted more nitrogen to dope in carbon matrix. Depending on the composition, the doping amount and PSDs can be widely varied without promoting graphitization. On the other hand, formation of hollow carbon was achieved by chlorinating $Ti(C_{0.3},N_{0.7})$ with highest nitrogen dopants at 800 ℃. Since most of nitrogen compositions are dissociated as N_2 gas, this creates channels in the particles for Cl_2 to react inside the particles and even break particles into pieces. Eventually hollow carbon is achieved. However, nitrogen doped hollow carbon possessed the lowest BET SSA, resulting lowest capacitance from all CNs. Hence, modification to starting material $Ti(C_{0.3},N_{0.7})$ was made by pre-vacuum-annealing at high temperature. The vacuum treatment resulted structural evolution toward thermodynamically stable crystallographic morphology with growth of ‘steps’. The chlorination of ‘steps’ containing $Ti(C_{0.3},N_{0.x})$ has produced core-shell structured carbon, where core consisting

highly microporous carbon with increased BET SSA, but only a slight decrease in nitrogen contents. This modified core-shell structured carbon demonstrated an enhancement in gravimetric capacitance, but in particular, a remarkable increase in volumetric capacitance of 233.8 F/cm^3 was obtained, which surpass the capacitance of currently reported CDCs but also, comparable to graphene materials.

Lastly, atomically dispersed Fe-CNB was demonstrated. This was not possible in boron-free Fe-CN synthesis, where large iron oxide particle growth occurred to form Fe_3O_4. From the COHP calculation, the bonding energy between Fe and N increased when boron was added into the system. The result demonstrate that when boron is positioned next to nitrogen atom, increased in binding energy between iron and nitrogen was found. This allows stronger bonding between Fe and N, and restricted agglomeration of iron or growth into larger particles. The obtained Fe-CNB was also analysed as a potential candidate for ORR electrocatalysts, where significant improvement was shown compared to CN, CNB, Fe-CN and even commercial Pt/C, without any post treatment. It is worth noting that the Fe-CNB catalysts was synthesized from single-step chlorination reaction and no leaching process was required. We expect that this new insight for synthesizing atomically dispersed Fe-CNB materials could offer other material scientists an opportunity to the scientific community. The original contribution to knowledge from this thesis is summarized in Figure 45.

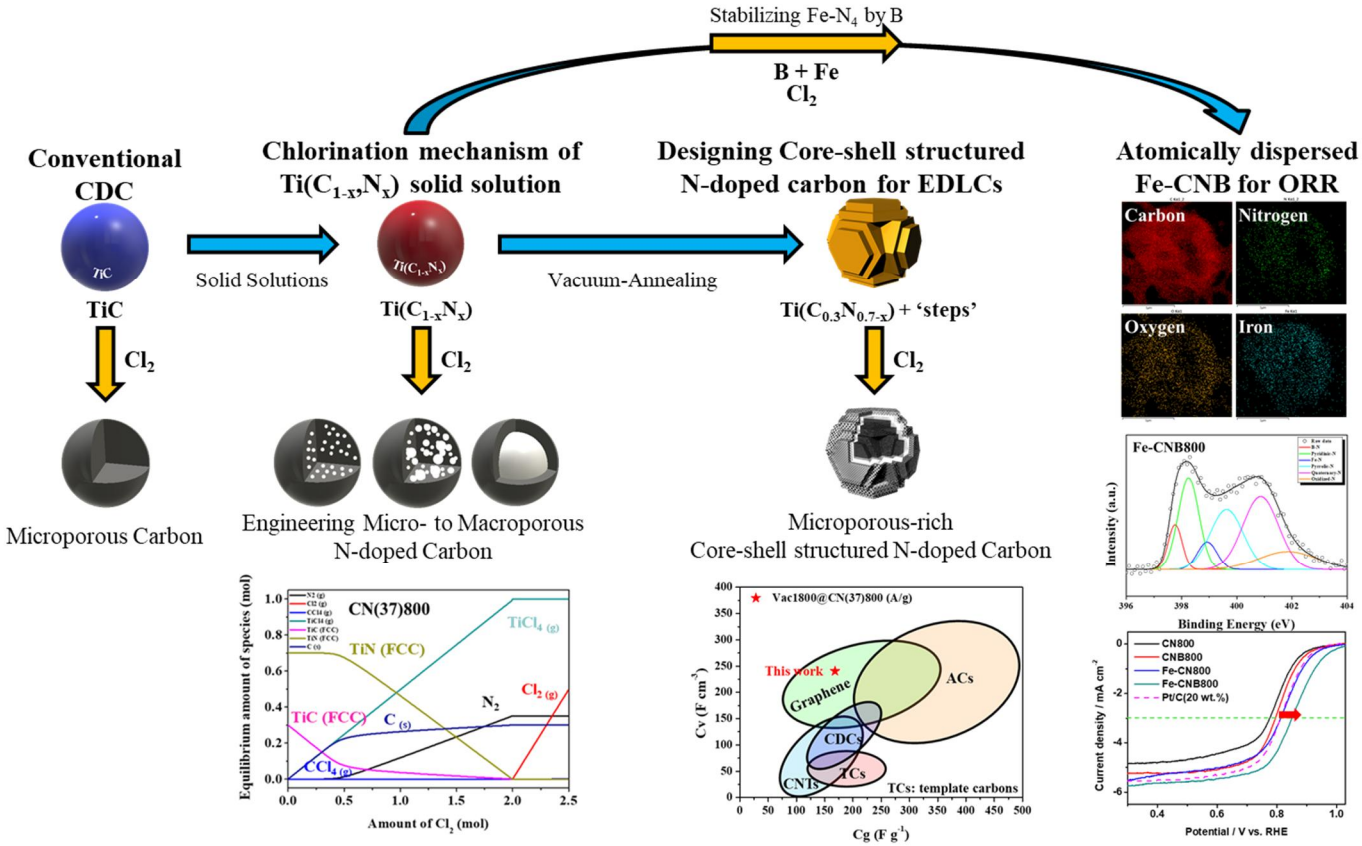

Figure 45. The original contribution to knowledge.

References

[1] C.R. Perez, S.H. Yeon, J. Segalini, V. Presser, P.L. Taberna, P. Simon, Y. Gogotsi, Structure and Electrochemical Performance of Carbide-Derived Carbon Nanopowders, Adv Funct Mater 23(8) (2013) 1081-1089.
[2] L. Borchardt, F. Hasche, M.R. Lohe, M. Oschatz, F. Schmidt, E. Kockrick, C. Ziegler, T. Lescouet, A. Bachmatiuk, B. Buchner, D. Farrusseng, P. Strasser, S. Kaskel, Transition metal loaded silicon carbide-derived carbons with enhanced catalytic properties, Carbon 50(5) (2012) 1861-1870.
[3] T. Palaniselvam, V. Kashyap, S.N. Bhange, J.B. Baek, S. Kurungot, Nanoporous Graphene Enriched with Fe/Co-N Active Sites as a Promising Oxygen Reduction Electrocatalyst for Anion Exchange Membrane Fuel Cells, Adv Funct Mater 26(13) (2016) 2150-2162.
[4] L. Cao, S. Sahu, P. Anilkumar, C.E. Bunker, J.A. Xu, K.A.S. Fernando, P. Wang, E.A. Guliants, K.N. Tackett, Y.P. Sun, Carbon Nanoparticles as Visible-Light Photocatalysts for Efficient CO2 Conversion and Beyond, J Am Chem Soc 133(13) (2011) 4754-4757.
[5] S. Sen Gupta, T.S. Sreeprasad, S.M. Maliyekkal, S.K. Das, T. Pradeep, Graphene from Sugar and its Application in Water Purification, Acs Appl Mater Inter 4(8) (2012) 4156-4163.
[6] M. Sevilla, R. Mokaya, Activation of carbide-derived carbons: a route to materials with enhanced gas and energy storage properties, J Mater Chem 21(13) (2011) 4727-4732.
[7] Z.H. Hu, M.P. Srinivasan, Preparation of high-surface-area activated carbons from coconut shell, Micropor Mesopor Mat 27(1) (1999) 11-18.
[8] J. Yan, Q. Wang, T. Wei, Z.J. Fan, Recent Advances in Design and Fabrication of Electrochemical Supercapacitors with High Energy Densities, Adv Energy Mater 4(4) (2014).
[9] K. Kierzek, E. Frackowiak, G. Lota, G. Gryglewicz, J. Machnikowski, Electrochemical capacitors based on highly porous carbons prepared by KOH activation, Electrochim Acta 49(4) (2004) 515-523.
[10] O. Barbieri, M. Hahn, A. Herzog, R. Kotz, Capacitance limits of high surface area activated carbons for double layer capacitors, Carbon 43(6) (2005) 1303-1310.
[11] M. Thommes, K. Kaneko, A.V. Neimark, J.P. Olivier, F. Rodriguez-Reinoso, J. Rouquerol, K.S.W. Sing, Physisorption of gases, with special reference to the evaluation of surface area and pore size distribution (IUPAC Technical Report), Pure Appl Chem 87(9-10) (2015) 1051-1069.
[12] J. Chmiola, G. Yushin, Y. Gogotsi, C. Portet, P. Simon, P.L. Taberna, Anomalous increase in carbon capacitance at pore sizes less than 1 nanometer, Science 313(5794) (2006) 1760-1763.
[13] M. Oschatz, S. Boukhalfa, W. Nickel, J.P. Hofmann, C. Fischer, G. Yushin, S. Kaskel, Carbide-derived carbon aerogels with tunable pore structure as versatile electrode material in high power supercapacitors, Carbon 113 (2017) 283-291.
[14] Y. Korenblit, M. Rose, E. Kockrick, L. Borchardt, A. Kvit, S. Kaskel, G. Yushin, High-Rate Electrochemical Capacitors Based on Ordered Mesoporous Silicon Carbide-Derived Carbon, Acs Nano 4(3) (2010) 1337-1344.
[15] G.A. Ferrero, K. Preuss, A.B. Fuertes, M. Sevilla, M.M. Titirici, The influence of pore size distribution on the oxygen reduction reaction performance in nitrogen

doped carbon microspheres, J Mater Chem A 4(7) (2016) 2581-2589.
[16] V. Presser, M. Heon, Y. Gogotsi, Carbide-Derived Carbons - From Porous Networks to Nanotubes and Graphene, Adv Funct Mater 21(5) (2011) 810-833.
[17] O. Hutchins, Method for the production of silicon tetrachlorid, Google Patents, 1918.
[18] Y. Gogotsi, A. Nikitin, H.H. Ye, W. Zhou, J.E. Fischer, B. Yi, H.C. Foley, M.W. Barsoum, Nanoporous carbide-derived carbon with tunable pore size, Nat Mater 2(9) (2003) 591-594.
[19] F. Beguin, V. Presser, A. Balducci, E. Frackowiak, Carbons and Electrolytes for Advanced Supercapacitors, Adv Mater 26(14) (2014) 2219-2251.
[20] Q. Wang, J. Yan, Z.J. Fan, Carbon materials for high volumetric performance supercapacitors: design, progress, challenges and opportunities, Energ Environ Sci 9(3) (2016) 729-762.
[21] M. Rose, Y. Korenblit, E. Kockrick, L. Borchardt, M. Oschatz, S. Kaskel, G. Yushin, Hierarchical Micro- and Mesoporous Carbide-Derived Carbon as a High-Performance Electrode Material in Supercapacitors, Small 7(8) (2011) 1108-1117.
[22] Y.P. Zhai, Y.Q. Dou, D.Y. Zhao, P.F. Fulvio, R.T. Mayes, S. Dai, Carbon Materials for Chemical Capacitive Energy Storage, Adv Mater 23(42) (2011) 4828-4850.
[23] X.G. Fu, P. Zamani, J.Y. Choi, F.M. Hassan, G.P. Jiang, D.C. Higgins, Y.N. Zhang, M.A. Hoque, Z.W. Chen, In Situ Polymer Graphenization Ingrained with Nanoporosity in a Nitrogenous Electrocatalyst Boosting the Performance of Polymer-Electrolyte-Membrane Fuel Cells, Adv Mater 29(7) (2017).
[24] L. Qie, Y. Lin, J.W. Connell, J.T. Xu, L.M. Dai, Highly Rechargeable Lithium-CO2 Batteries with a Boron- and Nitrogen-Codoped Holey-Graphene Cathode, Angew Chem Int Edit 56(24) (2017) 6970-6974.
[25] H. Tabassum, R.Q. Zou, A. Mahmood, Z.B. Liang, S.J. Guo, A catalyst-free synthesis of B, N co-doped graphene nanostructures with tunable dimensions as highly efficient metal free dual electrocatalysts, J Mater Chem A 4(42) (2016) 16469-16475.
[26] C. Zhan, Y. Zhang, P.T. Cummings, D.E. Jiang, Enhancing graphene capacitance by nitrogen: effects of doping configuration and concentration, Phys Chem Chem Phys 18(6) (2016) 4668-4674.
[27] K.P. Gong, F. Du, Z.H. Xia, M. Durstock, L.M. Dai, Nitrogen-Doped Carbon Nanotube Arrays with High Electrocatalytic Activity for Oxygen Reduction, Science 323(5915) (2009) 760-764.
[28] H.B. Li, W.J. Kang, L. Wang, Q.L. Yue, S.L. Xu, H.S. Wang, J.F. Liu, Synthesis of three-dimensional flowerlike nitrogen-doped carbons by a copyrolysis route and the effect of nitrogen species on the electrocatalytic activity in oxygen reduction reaction, Carbon 54 (2013) 249-257.
[29] B. Zheng, J. Wang, F.B. Wang, X.H. Xia, Synthesis of nitrogen doped graphene with high electrocatalytic activity toward oxygen reduction reaction, Electrochem Commun 28 (2013) 24-26.
[30] L.J. Yang, S.J. Jiang, Y. Zhao, L. Zhu, S. Chen, X.Z. Wang, Q. Wu, J. Ma, Y.W. Ma, Z. Hu, Boron-Doped Carbon Nanotubes as Metal-Free Electrocatalysts for the Oxygen Reduction Reaction, Angew Chem Int Edit 50(31) (2011) 7132-7135.
[31] Y. Zhao, L.J. Yang, S. Chen, X.Z. Wang, Y.W. Ma, Q. Wu, Y.F. Jiang, W.J. Qian, Z. Hu, Can Boron and Nitrogen Co-doping Improve Oxygen Reduction Reaction Activity of Carbon Nanotubes?, J Am Chem Soc 135(4) (2013) 1201-

1204.
[32] J. Kim, J. Han, D. Ha, S. Kang, Synthesis of nitrogen and boron co-doped carbon (CNB) and their CO2 capture properties: from porous to hollow granule structure, J Mater Chem A 2(39) (2014) 16645-16651.
[33] J.S. Han, D.Y. Chung, D.G. Ha, J.H. Kim, K. Choi, Y.E. Sung, S.H. Kang, Nitrogen and boron co-doped hollow carbon catalyst for the oxygen reduction reaction, Carbon 105 (2016) 1-7.
[34] F.L. Yuan, T. Yuan, L.Z. Sui, Z.B. Wang, Z.F. Xi, Y.C. Li, X.H. Li, L.Z. Fan, Z.A. Tan, A.M. Chen, M.X. Jin, S.H. Yang, Engineering triangular carbon quantum dots with unprecedented narrow bandwidth emission for multicolored LEDs, Nat Commun 9 (2018).
[35] M.J. Allen, V.C. Tung, R.B. Kaner, Honeycomb Carbon: A Review of Graphene, Chem Rev 110(1) (2010) 132-145.
[36] J. Liu, N.P. Wickramaratne, S.Z. Qiao, M. Jaroniec, Molecular-based design and emerging applications of nanoporous carbon spheres, Nat Mater 14(8) (2015) 763-774.
[37] J.Y. Shen, M.J. Wang, Y.N. Wu, F.T. Li, Preparation of mesoporous carbon nanofibers from the electrospun poly(furfuryl alcohol)/poly(vinyl acetate)/silica composites, Rsc Adv 4(40) (2014) 21089-21092.
[38] J.M. Zhang, Y.X. Zhang, S.Y. Lian, Y. Liu, Z.H. Kang, S.T. Lee, Highly ordered macroporous carbon spheres and their catalytic application for methanol oxidation, J Colloid Interf Sci 361(2) (2011) 503-508.
[39] X.L. Zou, L.Q. Wang, B.I. Yakobson, Mechanisms of the oxygen reduction reaction on B- and/or N-doped carbon nanomaterials with curvature and edge effects, Nanoscale 10(3) (2018) 1129-1134.
[40] H. Vaghari, H. Jafarizadeh-Malmiri, A. Berenjian, N. Anarjan, Recent advances in application of chitosan in fuel cells, Sustainable Chemical Processes 1(1) (2013) 16.
[41] L.F. Lai, J.R. Potts, D. Zhan, L. Wang, C.K. Poh, C.H. Tang, H. Gong, Z.X. Shen, L.Y. Jianyi, R.S. Ruoff, Exploration of the active center structure of nitrogen-doped graphene-based catalysts for oxygen reduction reaction, Energ Environ Sci 5(7) (2012) 7936-7942.
[42] G.A. Ferrero, K. Preuss, A. Marinovic, A.B. Jorge, N. Mansor, D.J.L. Brett, A.B. Fuertes, M. Sevilla, M.M. Titirici, Fe-N-Doped Carbon Capsules with Outstanding Electrochemical Performance and Stability for the Oxygen Reduction Reaction in Both Acid and Alkaline Conditions, Acs Nano 10(6) (2016) 5922-5932.
[43] Z.P. Miao, X.M. Wang, M.C. Tsai, Q.Q. Jin, J.S. Liang, F. Ma, T.Y. Wang, S.J. Zheng, B.J. Hwang, Y.H. Huang, S.J. Guo, Q. Li, Atomically Dispersed Fe-N-x/C Electrocatalyst Boosts Oxygen Catalysis via a New Metal-Organic Polymer Supramolecule Strategy, Adv Energy Mater 8(24) (2018).
[44] S. Chen, J.Y. Bi, Y. Zhao, L.J. Yang, C. Zhang, Y.W. Ma, Q. Wu, X.Z. Wang, Z. Hu, Nitrogen-Doped Carbon Nanocages as Efficient Metal-Free Electrocatalysts for Oxygen Reduction Reaction, Adv Mater 24(41) (2012) 5593-5597.
[45] Q. Li, R. Cao, J. Cho, G. Wu, Nanocarbon Electrocatalysts for Oxygen Reduction in Alkaline Media for Advanced Energy Conversion and Storage, Adv Energy Mater 4(6) (2014).
[46] D.W. Wang, D.S. Su, Heterogeneous nanocarbon materials for oxygen reduction reaction, Energ Environ Sci 7(2) (2014) 576-591.
[47] Z.W. Chen, D. Higgins, A.P. Yu, L. Zhang, J.J. Zhang, A review on non-

precious metal electrocatalysts for PEM fuel cells, Energ Environ Sci 4(9) (2011) 3167-3192.
[48] C.H. Choi, C. Baldizzone, J.P. Grote, A.K. Schuppert, F. Jaouen, K.J.J. Mayrhofer, Stability of Fe-N-C Catalysts in Acidic Medium Studied by Operando Spectroscopy, Angew Chem Int Edit 54(43) (2015) 12753-12757.
[49] M. Zhou, C.Z. Yang, K.Y. Chan, Structuring Porous Iron-Nitrogen-Doped Carbon in a Core/Shell Geometry for the Oxygen Reduction Reaction, Adv Energy Mater 4(18) (2014).
[50] L. Yang, D.J. Cheng, X.F. Zeng, X. Wan, J.L. Shui, Z.H. Xiang, D.P. Cao, Unveiling the high-activity origin of single-atom iron catalysts for oxygen reduction reaction, P Natl Acad Sci USA 115(26) (2018) 6626-6631.
[51] A. Zitolo, V. Goellner, V. Armel, M.T. Sougrati, T. Mineva, L. Stievano, E. Fonda, F. Jaouen, Identification of catalytic sites for oxygen reduction in iron- and nitrogen-doped graphene materials, Nat Mater 14(9) (2015) 937-+.
[52] A. Zitolo, N. Ranjbar-Sahraie, T. Mineva, J.K. Li, Q.Y. Jia, S. Stamatin, G.F. Harrington, S.M. Lyth, P. Krtil, S. Mukerjee, E. Fonda, F. Jaouen, Identification of catalytic sites in cobalt-nitrogen-carbon materials for the oxygen reduction reaction, Nat Commun 8 (2017).
[53] M.H. Shao, Q.W. Chang, J.P. Dodelet, R. Chenitz, Recent Advances in Electrocatalysts for Oxygen Reduction Reaction, Chem Rev 116(6) (2016) 3594-3657.
[54] C.W. Bale, E. Belisle, P. Chartrand, S.A. Decterov, G. Eriksson, A.E. Gheribi, K. Hack, I.H. Jung, Y.B. Kang, J. Melancon, A.D. Pelton, S. Petersen, C. Robelin, J. Sangster, P. Spencer, M.A. Van Ende, FactSage thermochemical software and databases, 2010-2016 (vol 54, pg 35, 2016), Calphad 55 (2016) 1-19.
[55] M.S. Seo, J.H. Kim, J.M. Kim, J.S. Han, S. Kang, J.S. Ihm, D.O. Kim, Tunable and selective formation of micropores and mesopores in carbide-derived carbon, Carbon 60 (2013) 299-306.
[56] J. Jung, S. Kang, Synthesis of ultrafine TiC1-X and Ti(CN) powders via planetary milling, Powder Metall 47(1) (2004) 93-98.
[57] D.S. Park, Y.D. Lee, S.H. Kang, Effect of carbides on the microstructure and properties of Ti(C, N)-based ceramics, J Am Ceram Soc 82(11) (1999) 3150-3154.
[58] I. Tallo, T. Thomberg, K. Kontturi, A. Janes, E. Lust, Nanostructured carbide-derived carbon synthesized by chlorination of tungsten carbide, Carbon 49(13) (2011) 4427-4433.
[59] D.V. Badami, G. Kaye, The Nature of Turbostratic Carbon, Carbon 1(3) (1964) 375-375.
[60] A.C. Ferrari, J. Robertson, Interpretation of Raman spectra of disordered and amorphous carbon, Phys Rev B 61(20) (2000) 14095-14107.
[61] A.C. Ferrari, Raman spectroscopy of graphene and graphite: Disorder, electron-phonon coupling, doping and nonadiabatic effects, Solid State Commun 143(1-2) (2007) 47-57.
[62] Q.T. Li, Z.C. Ni, J.L. Gong, D.H. Zhu, Z.Y. Zhu, Carbon nanotubes coated by carbon nanoparticles of turbostratic stacked graphenes, Carbon 46(3) (2008) 434-439.
[63] S. Urbonaite, L. Halldahl, G. Svensson, Raman spectroscopy studies of carbide derived carbons, Carbon 46(14) (2008) 1942-1947.
[64] D.G. Mcculloch, S. Prawer, A. Hoffman, Structural Investigation of Xenon-Ion-Beam-Irradiated Glassy-Carbon, Phys Rev B 50(9) (1994) 5905-5917.

[65] R.J. Nemanich, S.A. Solin, 1st-Order and 2nd-Order Raman-Scattering from Finite-Size Crystals of Graphite, Phys Rev B 20(2) (1979) 392-401.
[66] E.B. Barros, N.S. Demir, A.G. Souza, J. Mendes, A. Jorio, G. Dresselhaus, M.S. Dresselhaus, Raman spectroscopy of graphitic foams, Phys Rev B 71(16) (2005).
[67] R. Saito, A. Jorio, A.G. Souza, G. Dresselhaus, M.S. Dresselhaus, M.A. Pimenta, Probing phonon dispersion relations of graphite by double resonance Raman scattering, Phys Rev Lett 88(2) (2002).
[68] C. Lastoskie, K.E. Gubbins, N. Quirke, Pore-Size Distribution Analysis of Microporous Carbons - a Density-Functional Theory Approach, J Phys Chem-Us 97(18) (1993) 4786-4796.
[69] J. Silvestre-Albero, A. Silvestre-Albero, F. Rodriguez-Reinoso, M. Thommes, Physical characterization of activated carbons with narrow microporosity by nitrogen (77.4 K), carbon dioxide (273 K) and argon (87.3 K) adsorption in combination with immersion calorimetry, Carbon 50(9) (2012) 3128-3133.
[70] R.K. Dash, G. Yushin, Y. Gogotsi, Synthesis, structure and porosity analysis of microporous mesoporous carbon derived from zirconium carbide, Micropor Mesopor Mat 86(1-3) (2005) 50-57.
[71] J. Chmiola, G. Yushin, R. Dash, Y. Gogotsi, Effect of pore size and surface area of carbide derived carbons on specific capacitance, J Power Sources 158(1) (2006) 765-772.
[72] J. Xu, R.J. Zhang, P. Chen, D.J. Shen, X.Z. Ye, S.H. Ge, Mechanism of formation and electrochemical performance of carbide-derived carbons obtained from different carbides, Carbon 64 (2013) 444-455.
[73] S. Urbonaite, J.M. Juarez-Galan, J. Leis, F. Rodriguez-Reinoso, G. Svensson, Porosity development along the synthesis of carbons from metal carbides, Micropor Mesopor Mat 113(1-3) (2008) 14-21.
[74] A. Silvestre-Albero, S. Rico-Frances, F. Rodriguez-Reinoso, A.M. Kern, M. Klumpp, B.J.M. Etzold, J. Silvestre-Albero, High selectivity of TiC-CDC for CO2/N-2 separation, Carbon 59 (2013) 221-228.
[75] L.M. Dai, D.W. Chang, J.B. Baek, W. Lu, Carbon Nanomaterials for Advanced Energy Conversion and Storage, Small 8(8) (2012) 1130-1166.
[76] B.J. Lee, Thermodynamic assessment of the Fe-Nb-Ti-C-N system, Metall Mater Trans A 32(10) (2001) 2423-2439.
[77] P. Becker, F. Glenk, M. Kormann, N. Popovska, B.J.M. Etzold, Chlorination of titanium carbide for the processing of nanoporous carbon: A kinetic study, Chem Eng J 159(1-3) (2010) 236-241.
[78] T. Knorr, M. Kaiser, F. Glenk, B.J.M. Etzold, Shrinking core like fluid solid reactions-A dispersion model accounting for fluid phase volume change and solid phase particle size distributions, Chem Eng Sci 69(1) (2012) 492-502.
[79] T. Ariyanto, B. Dyatkin, G.R. Zhang, A. Kern, Y. Gogotsi, B.J.M. Etzold, Synthesis of carbon core-shell pore structures and their performance as supercapacitors, Micropor Mesopor Mat 218 (2015) 130-136.
[80] I.J. Jung, S. Kang, S.H. Jhi, J. Ihm, A study of the formation of Ti(CN) solid solutions, Acta Mater 47(11) (1999) 3241-3245.
[81] S.H. Yeon, D.H. Kim, S.H. Lee, S.S. Nam, S.K. Park, J.Y. So, K.H. Shin, C.S. Jin, Y.J. Park, Y.C. Kang, High microporosity of carbide-derived carbon prepared from a vacuum-treated precursor for energy storage devices, Carbon 118 (2017) 327-338.

[82] Z.Q. Li, C.J. Lu, Z.P. Xia, Y. Zhou, Z. Luo, X-ray diffraction patterns of graphite and turbostratic carbon, Carbon 45(8) (2007) 1686-1695.
[83] S.B. Jin, P. Shen, B.L. Zou, Q.C. Jiang, Morphology Evolution of TiCx Grains During SHS in an Al-Ti-C System, Cryst Growth Des 9(2) (2009) 646-649.
[84] S.B. Jin, P. Shen, D.S. Zhou, Q.C. Jiang, A Common Regularity of Stoichiometry-Induced Morphology Evolution of Transition Metal Carbides, Nitrides, and Diborides during Self-Propagating High-Temperature Synthesis, Cryst Growth Des 12(6) (2012) 2814-2824.
[85] W. Norimatsu, M. Kusunoki, Formation process of graphene on SiC (0001), Physica E 42(4) (2010) 691-694.
[86] C. Zhan, C. Lian, Y. Zhang, M.W. Thompson, Y. Xie, J.Z. Wu, P.R.C. Kent, P.T. Cummings, D.E. Jiang, D.J. Wesolowski, Computational Insights into Materials and Interfaces for Capacitive Energy Storage, Adv Sci 4(7) (2017).
[87] A. Bagri, C. Mattevi, M. Acik, Y.J. Chabal, M. Chhowalla, V.B. Shenoy, Structural evolution during the reduction of chemically derived graphene oxide, Nat Chem 2(7) (2010) 581-587.
[88] C. Largeot, C. Portet, J. Chmiola, P.L. Taberna, Y. Gogotsi, P. Simon, Relation between the ion size and pore size for an electric double-layer capacitor, J Am Chem Soc 130(9) (2008) 2730-+.
[89] K.V. Sankar, R.K. Selvan, Improved electrochemical performances of reduced graphene oxide based supercapacitor using redox additive electrolyte, Carbon 90 (2015) 260-273.
[90] C.N.R. Rao, A. Govindaraj, Carbon nanotubes from organometallic precursors, Accounts Chem Res 35(12) (2002) 998-1007.
[91] J. Leis, A. Perkson, M. Arulepp, P. Nigu, G. Svensson, Catalytic effects of metals of the iron subgroup on the chlorination of titanium carbide to form nanostructural carbon, Carbon 40(9) (2002) 1559-1564.
[92] K. Yuan, S. Sfaelou, M. Qiu, D. Lutzenkirchen-Hecht, X.D. Zhuang, Y.W. Chen, C. Yuan, X.L. Feng, U. Scherft, Synergetic Contribution of Boron and Fe-N-x Species in Porous Carbons toward Efficient Electrocatalysts for Oxygen Reduction Reaction, Acs Energy Lett 3(1) (2018) 252-260.
[93] D.H. Guo, R. Shibuya, C. Akiba, S. Saji, T. Kondo, J. Nakamura, Active sites of nitrogen-doped carbon materials for oxygen reduction reaction clarified using model catalysts, Science 351(6271) (2016) 361-365.
[94] C. Rivera□Cárcamo, P. Serp, Single atom catalysts on carbon□based materials, Chemcatchem.

Publication lists

1) Changes in the microstructure and mechanical properties of $(Ti_{0.88}W_{0.12})C$ and $(Ti_{0.88}W_{0.12})(C_{0.7}N_{0.3})$-20Ni upon Mo addition. Journal of Alloys and Compounds 698 (2017) 39-43.

2) Emission properties of Zinc Gallate nanophosphors. Journal of the Ceramic Society of Japan 126 [5] 382-388.

3) A study of salt-assisted solution combustion synthesis of magnesium aluminate and sintering behaviour. Ceramics International, https://doi.org/10.1016/j.ceramint.2018.12.155

4) Chlorination of titanium carbonitride solid solutions: Formation of nitrogen-doped carbon and its electrochemical applications. To be submitted.

5) Nitrogen-doped core-shell structured carbonitride-derived carbon with superior volumetric capacitance via pre-vacuum annealing process. To be submitted.

6) Atomically dispersed Fe-CNB material toward superior oxygen reduction reaction. In process.

Abstract (Korean)

Ti(C,N) solid solution과 염소간의 반응을 통한 N-doped carbon (CN) 의 합성, 그리고 붕소 추가를 통해 hollow structured B,N co-doped carbon (CNB)을 얻는 결과는 기존 실험에서 보고가 되었습니다. 허나, 이들 선행연구에서는 질소 치환이 가능 할 수 있었던 이유와, Ti(C,N) 의 질소의 양에 따른 구조적 변화 및 중공구조(hollow structure)를 얻는 메커니즘의 관한 이해는 다소 불충분 하였습니다.

불충분 했던 형성 메커니즘을 더 명확히 규명하고자, 본 졸업논문에서는 제 1부는 메커니즘에 대해 재론하고자 합니다.

제 1부에서 얻어진 이해를 통해 제 2부에서는 기존의 N-doped carbon을 에너지 소재의 특성 측면에서 어떻게 향상시킬 수 있는가?를 재료의 열역학적 결정학적 측면에서 살펴보고 이를 바탕으로 새로운 공정을 제시하였습니다. 본 공정을 통하여 capacitance가 크게 향상된 N-doped carbon (CN) 을 합성할 수 있으며, 본 소재가 에너지 저장 소재(슈퍼-커패시터)로서 높은 응용 가능성을 가짐을 보였습니다.

마지막으로 제 3부에서는 새로운 합성법을 통해 얻어진 Fe-CNB합성 메커니즘 및 전기화학 촉매(ORR)로의 응용을 논하고자 합니다. 앞에서 얻어진 결과 및 이해를 바탕으로, 탄소체(carbon) 표면에 전이금속 원자들

을 효과적으로 치환할 수 있는 방법을 제시하였으며, 이 과정에서 붕소의 도입이 Fe 원자가 N-doped carbon (CN) 에 원자단위로 효과적으로 치환되는데 중요한 역할을 함을 제시하였습니다. 원자단위로 분포된 Fe-Nx의 경우 Pyridinic-N 주변의 Fe, 즉 Fe-N4 로 형성된 구조로 존재할 때 열역학적으로 가장 안정합니다. 붕소의 도입은 Fe-CN에서 pyridinic-N의 안정성을 높여, Fe-N4 형성을 극대화 시키며, 합성된 Fe-CNB가 높은 촉매 특성(ORR)을 보이는 주요인자로 작용함을 증명하였습니다.